CONVECTION IN A ROTATING CAVITY.

by

SCOTT A. CONDIE

A thesis submitted for the degree of

Doctor of Philosophy

of the Australian National University.

Research School of Earth Sciences

November 1988

Except where otherwise mentioned in the text or in the acknowledgements, the research described in this thesis is my own.

Scott A. Condie

Acknowledgements

I would like to thank my supervisors Professor Stewart Turner, Dr Ross Griffiths and Dr Gregory Ivey for their encouragement and advice throughout this study. Greg taught me much about stratified fluids and experimental techniques, while Ross's expertise on rotating flows was invaluable. I would also like to express my appreciation to my good friend Dr Roger Nokes, who wrote the data logging and plotting routines. Thanks also to my adviser Dr Peter Baines for his interest in the project.

Mr Pat Travers constructed the convection tank, Mr Ross Wylde-Browne processed multitudes of photographs, while Mr Derek Corrigan and Mr Tony Beasley guided and assisted me with other technical problems. Derek also constructed the rotating table which I found to be an exceptional facility.

Finally, I would like to say that working with the GFD group has been an extremely enjoyable experience.

ABSTRACT

Many large scale flows in the ocean are driven by an imposed longitudinal density gradient and the resulting buoyancy-driven flow is both influenced by the Earth's rotation and has a low aspect ratio (i.e. the characteristic vertical scale of the motion is small compared to the characteristic horizontal scale of the motion). The essential features of such flows were incorporated into a laboratory model, by differentially heating and cooling the vertical end walls of a low aspect ratio, rectangular cavity rotating about a vertical axis through its centre.

When heating and cooling were initiated at the respective vertical end walls of the cavity, a hot current formed along the surface and a cold current along the bottom. These moved out from each end wall into the interior of the tank, but were confined to the sidewalls (model coastlines) by the effects of rotation. Initially the currents propagated under a balance between buoyancy and inertial forces, with an unstable balance between buoyancy and Coriolis forces in the cross-stream direction. Drag forces eventually slowed the the propagation speeds. The currents were internally stratified in temperature, and became unstable as a result of a rotationally dominated instability, driven by both the potential energy associated with the temperature difference between the currents and the isothermal environment and the velocity shear across the current. The flows were analogous to buoyancy driven coastal currents such as the East Greenland Current, the Norwegian Coastal Current and the Leeuwin Current off Western Australia.

As an experiment progressed, the instabilities on the currents grew and broke to produce eddies which eventually filled the cavity. The timescales for development of the stratification within the cavity were found to be dependent on the end wall temperatures, but independent of rotation. In its statistically steady state the mean circulation consisted of baroclinic boundary currents superimposed on two basin-scale counter-rotating gyres and a nearly linear vertical temperature gradient. These observations can be explained in terms of potential vorticity dynamics in the presence of a relative slope between isopotential surfaces and horizontal boundaries. Measurements of the potential vorticity were made in the laboratory flow and the quantity proved to be a very effective dynamical tracer. The steady state flow may have interesting implications for the large scale circulation of the oceans.

ERRATA

Page 12, line 1: Bracketed phrase should read:
"(but not necessarily turbulent)."

line 2: "large scale behaviour" should read:
"large amplitude behaviour."

Page 15, lines 4-7: should read:
"However, the oceans are strongly stratified and much of the geostrophic turbulence occurs as a result of baroclinic instability. Geostrophic turbulence generated by baroclinic instability in a two-layer stratification was contrasted with that generated by an oscillating grid in a homogeneous fluid in the experiments of Hopfinger et al. (1983) and Griffiths and Hopfinger (1984). They reported some notable differences."

Page 15, line 15: Insert "where h is the layer depth."

Page 15, line 21: should read:
"where the constant of order one relating these quantities was determined ..."

Page 21, line 9: Insert at end of sentence:
"and by starting a small, steady flow of dye through the hyperdermic tubes at the centre of each end wall."

Page 53, line 10: should read:
"Furthermore, the relative vorticity calculated from the velocity profiles given by the thymol blue technique (Figure 6.2) shows that $\zeta/f<10^{-1}$ even in the regions of maximum horizontal shear."

TABLE OF CONTENTS

CHAPTER 1

INTRODUCTION

Many geophysical flows are driven by buoyancy forces and have sufficiently large horizontal length scales to be influenced by the earth's rotation. For example, coastal currents driven by temperature or salinity gradients and influenced by the earth's rotation are common in the oceans. Fresh water entering the sea from rivers can be deflected to the right (in the Northern hemisphere) by Coriolis forces and moves along the coast. Many larger scale ocean currents flowing along continental coastlines are produced by horizontal density gradients and have a significant effect on the global circulation and coastal climates. Notable examples include the East Greenland Current (Wadhams et al. 1979), the Norwegian Coastal Current (Mysak and Schott 1977), the Alaska Coastal Current (Royer 1981) and the Leeuwin Current off Western and Southern Australia (Godfrey and Ridgeway 1985). Many of these currents flow along meridional boundaries and play a significant role in the transport of heat between polar and subpolar or temperate and equatorial regions.

Flows in large scale confined water bodies such as Seas, Gulfs and estuaries are also affected by rotation. For example, Atlantic Ocean water flows through the Strait of Gibraltar into the more saline western basin of the Mediterranean Sea known as the Alboran Sea (Whitehead and Miller 1979). Buoyant jets have also been observed in the St. Lawrence estuary and Gulf of St. Lawrence off Quebec. This is an unusual estuarine system, in that instability plays a important role in the dynamics of the system (Mertz et al. 1988). In South Australia, high evaporation rates at the shallow head of Spencer Gulf produce strong salinity gradients and the resulting gravity currents form a net landward residual flow (Nunes and Lennon 1987). This type of inverse estuary is particularly susceptible to the accumulation of pollutants at the head of the water body.

Another important class of oceanic gravity currents are dense flows along topography. These contribute dissolved oxygen to the deep ocean and maintain the deep-

sea density stratification. For example, with the exception of the North Atlantic, most of the bottom water in the worlds oceans flows out of the Weddell Sea near Antarctica (Warren 1981). Similar dense bottom currents derived from Greenland bottom water produce the North Atlantic deep water and the circulation of this flow is thought to significantly influence the climatological characteristics of northern Europe (Smith 1975).

The present study may also be relevant to the thermohaline component of the large scale circulation of the ocean. The relative role of wind stress and buoyancy flux in the ocean circulation is still unclear. Specifically, Luyten and Stommel (1986) suggest that the baroclinic circulation may be 'driven by buoyancy and steered by wind'. Even in the deep ocean, where the direct effects of wind stress are small compared to those in the upper ocean, our understanding of the circulation is very limited. Despite these difficulties, the importance of this system cannot be overstated. The large scale circulation of the ocean forms an integral component (and perhaps the weakest link), in the atmospheric global warming models which predict the climatic effects of 'greenhouse gases' in the atmosphere.

Given this range of oceanic applications, there is considerable interest in describing the dynamics of rotationally dominated, density driven flows.

1.1 Research Approach

Each of the flows described in the previous section has three common features: an imposed longitudinal density gradient, a low aspect ratio (ratio of the depth to the horizontal length scale) and the influence of the earth's rotation. This study incorporates these characteristics in a laboratory experiment. Buoyancy is supplied to fluids by differentially heating and cooling the end walls of a shallow rectangular cavity, which rotates about a vertical axis through its centre. The boundary currents observed in the cavity immediately after the heating and cooling were initiated were similar to the surface coastal currents described above, while the later flow had features in common with abyssal circulation.

Chapter two reviews previous work and provides some necessary background information. In chapter three the laboratory facilities are described and parameters which describe the system are defined. The evolution of the flows is described in chapters four, five and six. These correspond to the formation of the initial intrusions (published in Condie and Ivey 1988), the longer term development of the transient flow (Condie 1988 in press) and the steady state flow (Condie and Griffiths 1988 - submitted for publication) respectively. In chapter seven the results are applied to oceanic flows and a conclusion is presented in chapter eight.

CHAPTER 2

REVIEW

This chapter reviews previous work of relevance to the present study. Buoyantly driven currents in non-rotating systems are considered first. Of particular relevance to this research are the density currents produced when a longitudinal temperature gradient is applied across a cavity (i.e. the non-rotating analogue of this study). Previous work on these flows is described in Section 2.2. Rotating density currents are then reviewed followed by a discussion of rotationally induced instabilities. Relevant oceanic studies are incorporated in chapter seven, where comparisons with the experiments are made.

2.1 Non-rotating Density Currents

A density current or gravity current is the flow of one fluid within another, driven by the density difference between the fluids. Gravity currents in non-rotating systems have been studied extensively (see the review by Simpson 1982). The basic features of gravity currents flowing along horizontal surfaces (including free surfaces) will now be described briefly, as background for the study of the more complex rotating currents.

The profile of a gravity current is dependent upon the Reynolds number, $Re = uh/\nu$, were u is the velocity, h is the characteristic depth of the intrusion and ν is the kinematic viscosity (Figure 2.1). At the leading edge of most gravity currents there exists a 'head' or 'billow' of depth greater than the following flow. This structure is produced by shear across the interface which separates the intrusion and ambient fluid. The foremost point of the head is referred to as the nose. When $Re > 10^3$, billows stream back from the upper surface of the gravity current head, producing intense mixing. The initial velocity of the nose is found to scale with the internal wave speed $(g'h)^{1/2}$ where $g' = g(\rho-\rho_0)/\rho_0$ is the reduced gravity, g is the gravitational acceleration, ρ is the density of the intrusion and ρ_0 is the density of the ambient fluid. However, Simpson and Britter (1979) found the nose speed to be sensitive to the ratio of the intrusion depth to the total fluid depth in lock-exchange experiments. After the gravity current has progressed some

distance the velocity begins to decay as viscous forces dominate over inertial forces.

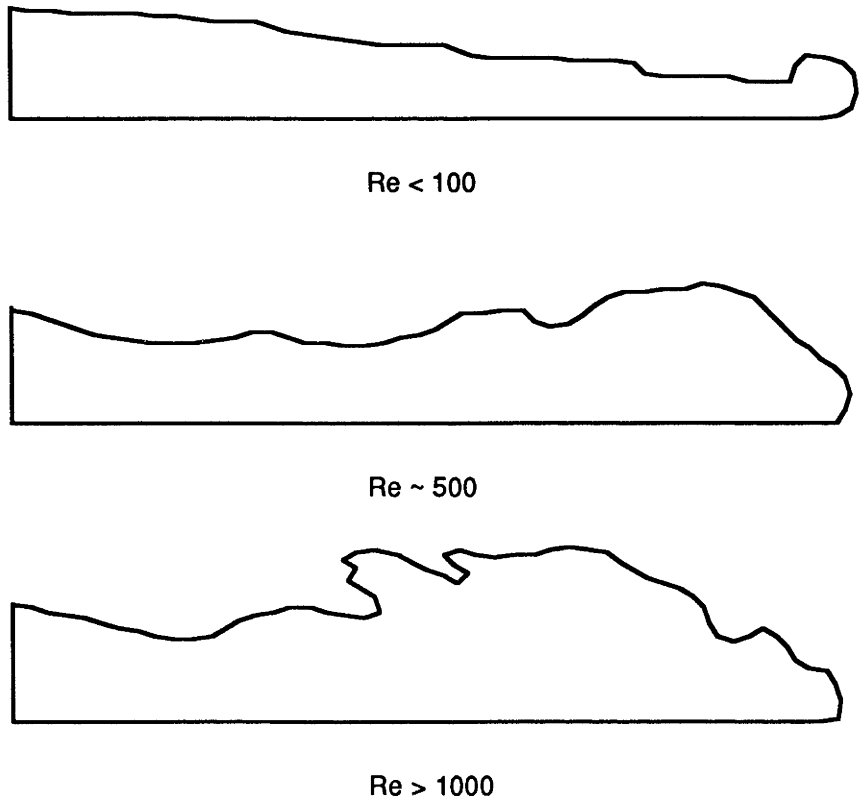

Figure 2.1 Schematic representations of gravity currents moving along a horizontal boundary, for a range of Reynolds numbers.

2.2 Convection in a Stationary Cavity

A particular class of density current is produced by the initial motion of a convectively driven flow in a closed cavity (reviewed in Bejan 1984). The problem can be defined in the following manner. A stationary rectangular cavity of height H, length L, and width B contains isothermal fluid of density ρ_0, kinematic viscosity ν, thermal diffusivity κ, and temperature T_0. The bottom and top boundaries ($z = 0$, H) and side boundaries ($y = 0$, B) are thermally insulated. At time $t = 0$ a temperature $T_0+\Delta T/2$ is instantaneously applied to one end wall ($x = 0$) and $T_0-\Delta T/2$ to the other end wall ($x = L$). This produces a thermal boundary layer at each end wall. Near the heated (cooled) wall fluid rises (falls) vertically, then travels along the horizontal lid (bottom) as a density current.

The dynamics of this system are governed by three dimensionless parameters (Batchelor 1954). The first of these is the aspect ratio

$$A = \frac{H}{L}, \tag{2.1}$$

which depends only on the cavity geometry. The second is the Prandtl number, a property of the fluid and defined as the ratio of the kinematic viscosity to the thermal diffusivity. i.e.

$$Pr = \frac{\nu}{\kappa}. \tag{2.2}$$

The final parameter is the Rayleigh number which describes the forcing by the applied temperature difference ΔT between the end walls. This is defined by the relation

$$Ra = \frac{g\alpha\Delta T H^3}{\nu\kappa}, \tag{2.3}$$

where α is the coefficient of thermal expansion.

Patterson and Imberger (1980) investigated transient behaviour as a function of the parameters defined above, with the aid of scaling arguments. It was found that when $Ra < 1$, there was a long heat up period in which heat transfer was dominated by conduction. When $Ra > \max (Pr^2, A^{-12})$ heat transfer was virtually purely advective. It is interesting to note that similar flow regimes to those described here occurred when the heating and cooling were replaced by a linear distribution (in the horizontal) of sources and sinks (Patterson 1984). This suggests that cavity convection experiments may be relevant to a broad range of density driven flows.

The numerical results of Patterson and Imberger (1980) indicated that for $Ra > Pr^4 A^{-4}$, the flow velocities (and thus heat transfer) rose sharply when the temperature gradient was first applied, then experienced an oscillatory decay to steady state values. To explain this it was postulated that warm fluid was drawn down by entrainment over the entire upper half of the cold boundary, resulting in tilting of isotherms and consequent formation of internal waves. However subsequent laboratory observations by Ivey (1984) found no evidence of cavity scale oscillations, although

some oscillatory behaviour was detected and attributed to the presence of internal hydraulic jumps (see Turner 1973 p 64).

Patterson and Imberger (1980) also derived the 'heat-up time' for establishment of the steady state temperature structure within the cavity. Their theory was based on a simple 'filling box' process in which the interior of the cavity was assumed to fill with heated fluid by horizontal layering. They showed that the volume flux pumped through the thermal boundary layers of the end walls, scales as $B\kappa Ra^{1/4}$. The timescale to pump all the fluid in the cavity through the boundary layers is therefore

$$\tau \sim \frac{HL}{\kappa Ra^{1/4}}. \qquad (2.4)$$

Experimental observations by Yewell, et al. (1982) and Ivey and Hamblin (1988), verified the existence of a filling box type of process with timescales consistent with equation (2.4).

The steady-state convective flow has been studied more extensively than the transient problem. Early interest, such as the analytical studies of Batchelor (1954) and Gill (1966), and experimental work by Elder (1965) focussed on the large aspect ratio cavities. The principal motivation for these studies was engineering problems involving insulating cavities. In keeping with oceanographic interests, emphasis here is on low aspect ratio cavities. These were first considered in detail in a series of papers in 1974. Cormack, Leal and Imberger (1974) examined the steady-state problem in the limit of small aspect ratio A (and Ra, Pr fixed) by matching asymptotic solutions for the centre and end of the cavity. Essentially the solution consisted of parallel flow in the core, with passive end regions in which the flow was turned through 180 degrees. In the interior, vertical diffusion of heat from the warm to the cold intrusion layers eliminated all vertical temperature structure. These results agree with the numerical solutions of the full Navier-Stokes equation by Cormack, Leal and Seinfeld (1974) for the parameter range $A < 0.1$, $Ra^2A^3 < 10^5$.

Cormack, Leal and Seinfeld (1974) also demonstrated the transition from the low

aspect ratio limit to the boundary layer limit of Gill (1966), in which A is fixed and $Ra \rightarrow \infty$. Under these circumstances the intrusions formed jets and heat transfer was almost purely advective, with isotherms tending towards the horizontal. These jets were observed experimentally by Bejan, Al-homoud and Imberger (1981), while the criterion distinguishing the two flow regimes was refined by Ivey and Hamblin (1988) using scaling arguments:

$$RaA^4 < Pr^4 \quad \text{parallel flow (no jets),} \tag{2.5a}$$

$$RaA^4 > Pr^4 \quad \text{intrusion layers (jets).} \tag{2.5b}$$

This result is consistent with available experimental data. The third paper in the series (Imberger 1974) was an experimental investigation using cavities of aspect ratio 1.0×10^{-2} and 1.9×10^{-2}. This confirmed the existence of parallel core flow which shrank in volume as Ra^2A^3 was increased. Qualitative agreement was found with the numerical results, although these had been restricted to larger aspect ratios.

It can be concluded from the above discussion that a reasonable understanding of the dynamics of flows in stationary convection cavities has been obtained. This understanding represents a good basis from which to extend the work to include rotational effects.

2.3 Rotating Density Currents

Another area of study closely related to the present work involved the release of buoyant fluid into a rotating channel. Such work has focussed on the formation and motion of the initial intrusion (see review by Griffiths 1986). The first of these, a theoretical analysis by Gill (1976), found linear solutions for a channel in which the initial free surface depth of the fluid was described by a step function. The adjustment process consisted of a buoyancy dominated period not unlike the non-rotating case, followed by a transition to flow governed by Coriolis forces. In the limit of small channel width, rotational effects were suppressed while adjustment in an infinitely wide channel was governed by the Rossby radius length scale

$$R = \frac{(g'h)^{1/2}}{f}, \qquad (2.6)$$

where f is the Coriolis parameter. The finite width solution produced intrusions along the side boundaries.

The experimental counterpart to Gill's theory is the 'lock-exchange experiment' in a rotating channel. In previous studies, a vertical barrier separating fluids of different densities was removed so that the lighter fluid spread over the heavy fluid and was deflected to the right (anti-clockwise rotation) by Coriolis forces. Using this approach Stern, Whitehead and Hua (1982) observed boundary currents for a range of density differences and rotation rates. In that study, the currents consisted of an unsteady bulbous head with a thin neck, followed by a quasi-laminar jet along the boundary. The width of the boundary jet, nose velocity and detrainment coefficient (fraction of the boundary transport left behind the propagating nose) were measured. Theoretical values of these quantities, based on a similarity solution, were in reasonable agreement with their experiment. A slightly better prediction for the nose velocity during its early propagation, was obtained by Nof (1987) by assuming that the head of the current was non-hydrostatic.

After the flow produced by Stern et al. (1982) progressed a short distance from the lock, the nose velocity decreased until eventually the flow either separated from the wall or became stagnant. Griffiths and Hopfinger (1983) quantified this behaviour in similar experiments, and identified a decay in both the depth and the velocity of the nose, which was well described by an exponential law. They argued that for currents with Ekman numbers less than 10^{-3} this decay was the result of transfer of momentum into the lower layer by inertial waves excited by turbulent motions near the nose. For larger Ekman numbers the decay was dominated by Ekman dissipation. When the depth and velocity became very small, Griffiths and Hopfinger reported a transition to a shallow viscous intrusion moving slowly along the wall.

These studies all deal with constant volume releases and the subsequent slump of the fluid. The constant flux case (as produced in the convection cavity) has not been

considered in such detail, with previous studies almost exclusively theoretical. Stern (1980) examined the effect of finite amplitude long wavelength perturbations on a geostrophically balanced boundary current and the propagation of the nose. Ikeda (1984) modeled freshwater discharge into a two layered ocean, by representing the density flux as entrainment of one of the density layers into the other. In a laboratory experiment, Griffiths and Linden (1981a) produced a continuous boundary current by releasing buoyant fluid adjacent to a vertical cylinder at the centre of rotation (see Section 2.4). Such 'point source' experiments are however, restricted to low Reynolds numbers.

Other more recent studies of rotating density currents have considered the effects of additional complications, such as bottom topography. For example Hsieh and Gill (1984) and Whitehead and Chapman (1986) observed flows over a sloping bottom, while Gill, Davey, Johnson and Linden (1986) examined the flow over a step. Such studies are particularly important in determining the influences of the continental shelf on ocean boundary currents.

2.4 Instability

Prominent features along boundary currents in both nature and the laboratory are shear induced instabilities, commonly referred to in the literature as baroclinic instabilities. These can have a significant influence on the dynamics and heat transfer of convective flows. Rotation tends to inhibit the transport of heat and momentum (except along meridional boundaries), whereas instability breaks the geostrophic constraints and allows these quantities to be transferred in the form of eddies. There have been many studies of rotationally induced instabilities and in particular of baroclinic waves, due to their application to the atmospheric circulation. More recently their importance to large scale oceanic flows has been recognized.

Instabilities are most frequently generated at density fronts where high shear stresses exist. Baroclinic instabilities result from vertical shear and derive energy from the potential energy stored in the density structure. Barotropic instabilities, on the other hand, obtain their energy from the kinetic energy of horizontally sheared flows. In

practice, most instabilities rely on some combination of these mechanisms. Traditionally the dominant mechanism was identified from the wavelength of the most rapidly growing wave. If this quantity scaled with the internal deformation radius then the instability was thought to be baroclinic, whereas if it scaled with the width of the shear zone it was thought to be barotropic. However, a recent study by Killworth et al. (1984) cast some doubt on these conclusions, with predictions of mixed mode instabilities with wavelengths that scaled with the deformation radius.

2.4.1 Small Amplitude Theory

Charney (1947) and Eady (1949) determined theoretically that a small amplitude sinusoidal perturbation applied to a vertically sheared rotating flow would grow spontaneously. Stability analysis has since been applied to many boundary flow configurations (e.g. Stern 1980, Killworth 1980, Griffiths, Killworth and Stern 1982). Killworth and Stern (1982) examined the stability of a coastal density current forming a front. They found that when the mean flow at the wall is zero (such as in the laboratory) the flow is unstable provided the mean potential vorticity increases towards the wall. Conventional quasi-geostrophic theory (a single active layer) had required an extremum of the potential vorticity for instability. Killworth (1983) found that in the absence of the boundary, the front is unstable provided it is sufficiently narrow with respect to the Rossby radius. The same instability also occurred in the theory of Kubokawa (1985).

Killworth, Paldor and Stern (1984) considered a more realistic geostrophic boundary current, for which the lower layer was of finite depth. The effect of the lower layer is such that the front is always unstable to a combination of baroclinic and barotropic waves, regardless of the potential vorticity distribution. In this case the growing waves extract energy from both vertical (baroclinic) and horizontal (barotropic) velocity shears. Instabilities with the same characteristics were predicted by Paldor and Killworth (1987) for an isolated front. Both studies yielded wave numbers of order R^{-1} (i.e. wavelengths around $2\pi R$), where R is the deformation radius.

2.4.2 Large Amplitude Instability

When instabilities reach finite amplitude their motion becomes nonlinear (but not turbulent). Theoretical work is then difficult, and most progress in large scale behaviour has been experimental. Two of the most successful classes of experiments designed to study baroclinic instability are illustrated in Figure 2.2. The first involved rotating an annulus, while differentially heating the inner and outer walls (see review by Hide and Mason 1975). The dynamics of this system are governed by the dimensionless parameter

$$\theta = \frac{g\alpha\Delta T H}{f^2(b-a)^2}. \tag{2.7}$$

When $\theta > 1$ the flow was stable and axisymmetric, while at lower values, steady baroclinic waves were present. These vacillated periodically in shape, amplitude and wave number if θ was further reduced. Finally when $\theta < 0.1$, the waves became irregular and decayed into a geostrophically turbulent state. When friction became important an additional parameter,

$$\Im = \frac{f^2(b-a)^5}{\nu^2 H}, \tag{2.8}$$

needed to be specified.

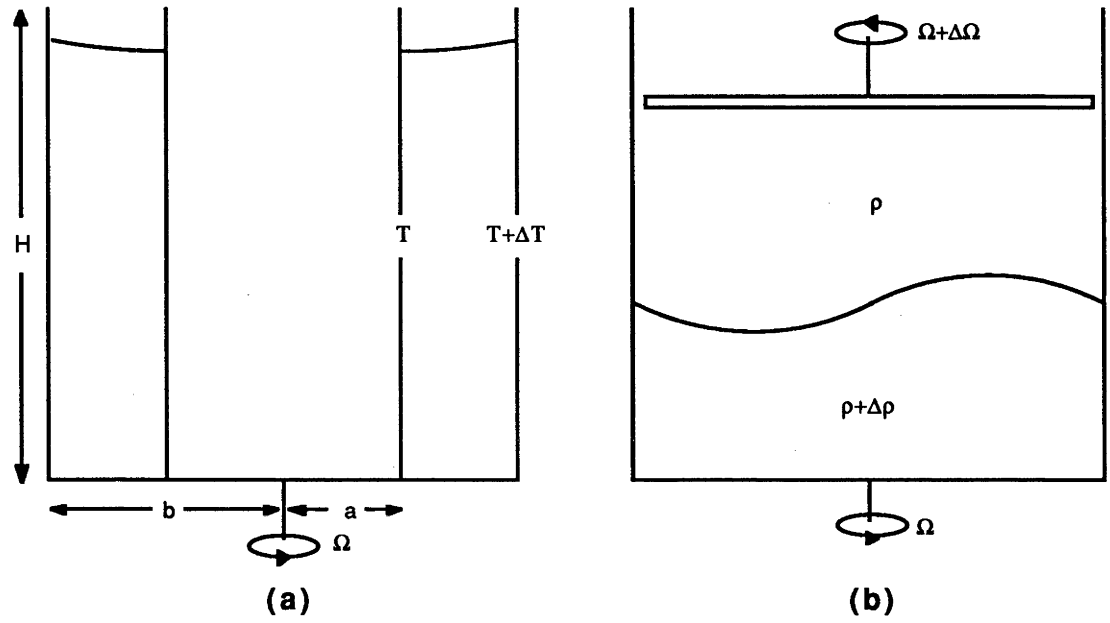

Figure 2.2 Cross-sections of experiments designed to study baroclinic instability.

A number of variations on the basic annulus configuration have recently been studied. For example, Hignett, Ibbetson and Killworth (1981), Hathaway and Fowlis (1986) and Miller and Fowlis (1986) considered the effects of applying a radial temperature gradient along the horizontal boundaries. Li, Kung and Pfeffer (1986) introduced bottom topography, while Hyun (1984) replaced the heating and cooling with a source-sink system.

In the second type of experiment (Figure 2.2(b)), two fluid layers of different densities were contained in a rotating cylinder and driven from above, by a differentially rotating disc. Similar regimes (e.g. stable flow, steady waves, amplitude vacillation) to those observed in the annulus experiments were reported (Hart 1973, 1980, 1981). A more extensive review of both the annulus and rotating disc experiments was presented by Hart (1979).

The production of baroclinic waves and eddies at density fronts will now be considered. Most available results are again experimental, with theoretical progress mainly restricted to isolated structures (reviewed by Flierl 1987). Griffiths and Linden (1981a) produced density driven boundary flows by releasing buoyant fluid adjacent to a vertical cylinder at the centre of rotation. When the width of the current reached a few Rossby radii, what is believed to have been a mixed baroclinic-barotropic instability was observed. For experiments involving current depths that were a significant fraction of the total depth, wavelengths were adequately predicted by Phillips' model for baroclinic instability (Pedlosky 1979, pp485). A later comparison with a more sophisticated model proposed by Killworth et al. (1984) showed good agreement.

Similar experiments by Griffiths and Linden (1982) and Chia, Griffiths and Linden (1982) ensured approximate conservation of potential vorticity, by releasing a set volume of buoyant fluid held in an annulus at the centre of rotation. A criterion for the onset of instability was established based on the rotating Froude number of the buoyant fluid before release. When waves grew to large amplitude, they detached from the coastal current to form anticyclonic eddies in the upper layer. These coupled with cyclonic eddies

produced in the lower layer wave troughs to form vortex dipoles, which in turn could interact to produce geostrophic turbulence. Vortex structures have also been observed off upwelling fronts, produced by an applied surface stress (Narimousa and Maxworthy 1987). They have also been studied extensively as isolated structures (for example Flierl, Stern and Whitehead 1983 and Fedorov and Ginsburg 1986).

2.4.3 Geostrophic Turbulence

When eddies produced at a density front in a rotating fluid interact, the motion often decays into a turbulent state. Despite non-linearity, the flow is always near geostrophic and hydrostatic balance. Coriolis forces tend to orientate the wave vector in a direction perpendicular to the rotation axis, giving the turbulence a two dimensional character. The result is that vortex stretching, the mechanism which transfers energy to smaller length scales in three dimensional turbulence, is absent in geostrophic turbulence (a comparison of two and three dimensional turbulence is given by Tennekes 1985). In fact, Batchelor (1969) showed that in order to conserve energy and vorticity in two dimensional turbulent flows, energy must be transferred towards larger length scales (i.e. from large to small wavenumbers), while enstrophy ($\frac{1}{2}\zeta^2$ where ζ is the relative vorticity) cascades to smaller scales. Geostrophic turbulence and its effects on the potential vorticity field of oceanic flows has been reviewed by Rhines (1979) and Ivchenko and Klepilov (1985), while Holloway (1986) gave a detailed account of the statistical properties of the phenomena.

Because of the difficulties associated with the creation of geostrophic turbulence, laboratory experiments have met with less success than their three dimensional counterparts (Tritton 1985). Most have involved the production of turbulence using either an oscillating grid (Bretherton and Turner 1968, Hopfinger et.al. 1982, Dickinson and Long 1983) or boundary forcing with sources and sinks (McEwan 1976, Colin de Verdiere 1980). Bretherton and Turner, and McEwan were interested in angular momentum mixing, while later studies concerned themselves with the overall properties of the turbulence. For example, Hopfinger et.al. (1982) examined the transition from

three to quasi two dimensional turbulence and discovered isolated waves propagating along vortex cores.

The experiments mentioned in the previous paragraph involved only homogeneous fluids. However, geophysical turbulence is concentrated in regions where stratification is strongest, such as ocean fronts. The only detailed experimental studies of this phenomenon appear to be the two layer experiments of Hopfinger et. al. (1983) and Griffiths and Hopfinger (1984). They reported some notable differences from the homogeneous case. Turbulence which evolved from rotationally induced instability consisted of almost equal numbers of cyclonic (lower layer) and anticyclonic (upper layer) eddies, both of which had low relative vorticity ($< f/6$). In contrast, the eddies observed in homogeneous fluids were predominantly cyclonic and had vorticity of order f.

Griffiths and Hopfinger (1984) also examined spreading across a front due to mesoscale turbulence, and found it could be satisfactorily described in terms of a horizontal turbulent diffusion coefficient κ_H. They showed that the turbulence intensity scaled with the internal wave speed ($<U^2>^{1/2} \sim (g'h)^{1/2}$) and that the eddy length scale was the internal Rossby radius R. The theory of Haidvogel and Keffer (1984) indicated that the effective ensemble-averaged horizontal turbulent diffusivity coefficient was given by the product of appropriate velocity and length scales. Griffiths and Hopfinger concluded that,

$$\kappa_H \sim R<U^2>^{1/2} \sim \frac{g'h}{f}, \qquad (2.9)$$

where the order one constant was determined experimentally to be 0.59. Ivey (1987) conducted a quite different experiment in which a turbulent front was created at the interface of two layers by an oscillating grid, and obtained a constant of 0.13.

2.5 Rotating Convection Experiments

In addition to the annulus experiments discussed in Section 2.4.2, there have been two other convection experiments of relevance to large-scale ocean circulation. Sugimoto and Whitehead (1983) considered quite a complex configuration in which a shallow

rectangular sea of constant depth was bounded by a deep ocean through a uniformly sloping bottom region. The fluid was heated at the deep ocean end wall and cooled at the surface, while the system rotated. The resulting flow included a number of gyres (dependent on the rotation rate), and a jet-like front along the shelf break. More recently, Speer and Whitehead (1988) conducted experiments in a rotating rectangular cavity with non-uniform heating from below. This system modelled convection in an ocean with non-uniform heating at the surface. Over much of the parameter range studied, the flow was dominated by a cyclonic gyre in the upper layer and much weaker anticyclonic motions near the bottom.

2.6 Summary

A review of relevant aspects of previous work has been presented. Studies of convection in stationary rectangular cavities with differentially heated end walls provide a background from which to extend the work to rotating reference frames. Although constant flux intrusions have not previously been studied in rotating channels, constant volume releases have many similar characteristics and provide an interesting comparison with the early development of the convection experiment. The review has also discussed rotational instabilities and their interaction to produce geostrophic turbulence. These are very prominent features of rotating buoyancy driven flows and will be seen to be of fundamental significance to this study.

CHAPTER 3

EXPERIMENTAL CONFIGURATION

In this chapter, the experimental apparatus used in the study is described. Appropriate non-dimensional parameters which govern the dynamics of this system are then defined.

3.1 Apparatus

A photograph of the basic apparatus consisting of the convection tank mounted on the rotating table is shown in Figure 3.1. The experiments were conducted in a rectangular perspex cavity of height H = 15cm, length L = 200cm and width B = 60cm, giving a fixed longitudinal aspect ratio of A = 0.075. Heat exchangers formed the two vertical end walls of the tank (Figure 3.2) and consisted of a 3.0cm thick aluminium block with 1.2cm square grooves through which heated or cooled water was pumped. To ensure an even temperature distribution over the heat exchanger surface, a 1.0cm thick block of copper was in contact with the working fluid. Copper was chosen because of its high thermal conductivity and adequate resistance to corrosion. Thermistors embedded in the copper and aluminium plates allowed both the temperature gradient between the plates, and the temperature in contact with the fluid to be measured. With the end walls calibrated (Appendix A), the heat flux into the fluid could be calculated from the temperature gradient. Three hypodermic tubes inserted through the end walls allowed dye to be continuously gravity fed into the fluid to visualize the flow.

The tank was insulated to minimize heat losses. It rested on a sheet of 5cm thick expanded polystyrene, while side wall heat transfer was restricted by air cavities of width 10cm. When neither side visualization nor side lighting was required these cavities where filled with polystyrene. The lid, as a potential source of significant losses, was designed as a series of sealed transparent air cavities. The depth of the cavities was selected to

Figure 3.1 The convection tank mounted on the rotating table.

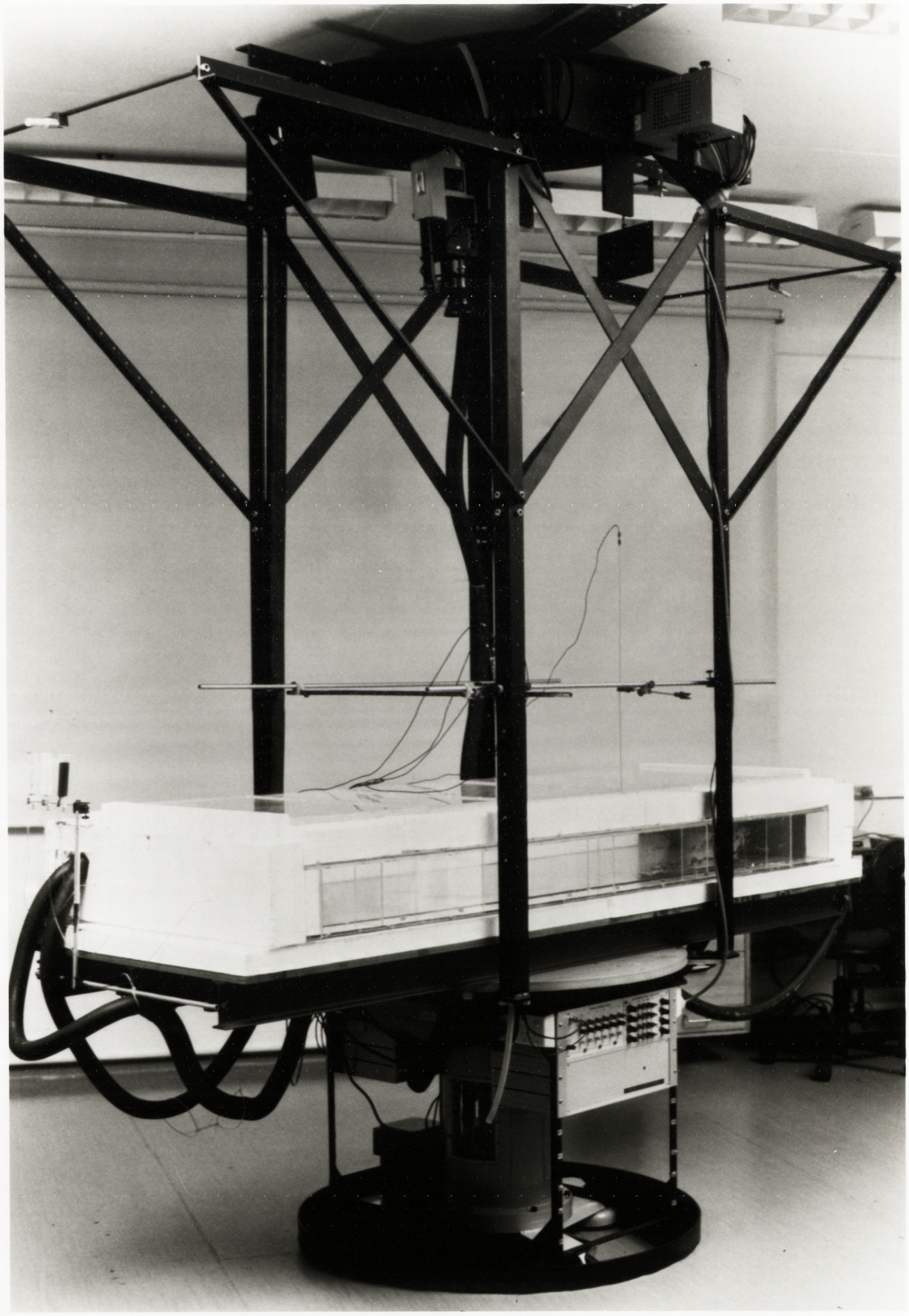

minimize heat losses. For an air cavity with a Rayleigh number within the range $7x10^3 < Ra < 2.7x10^5$, the Nusselt number is given by $Nu = 0.22Ra^{1/4}$ and when $Ra > 2.8x10^5$, $Nu = 0.075Ra^{1/3}$ (Rossby 1969). Considering a typical case in which a 10°C gradient exists within the lid cavities, this gives a Rayleigh number of $Ra = 1.2x10^9D^3$, where D is the lid cavity depth. Then since the heat transfer is proportional to Nu/D we find that the heat loss is proportional to $D^{-1/4}$ for D < 6cm and independent of D for D > 6cm. To allow for some error in this figure and to ensure reasonable rigidity, the lid was constructed with a thickness of D = 10cm.

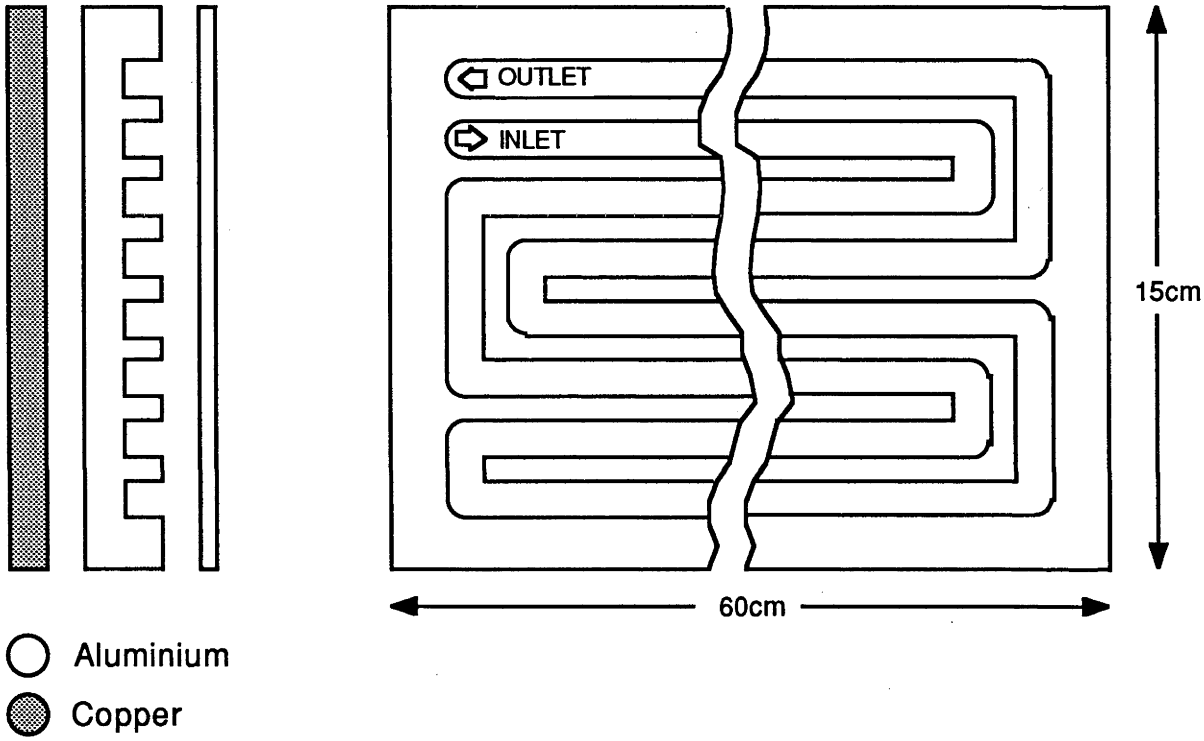

Figure 3.2 The heat exchangers which form the end walls of the cavity.

This assembly was mounted on a 1.0m diameter rotating table. This facility has a rotation speed range of 0-18 rad/sec and can maintain a constant speed to within 0.1% for the range of rotation speeds used in this study. Fluid slip rings allowed the hot and cold baths supplying fluid to the end walls to be located off the table. Visual facilities included a video camera and recorder, movie camera and still cameras. Active thermistor bridges on the turn-table allowed for amplification of thermistor probe signals. The amplified signals passed through electrical connections from the rotating table to the stationary reference frame, where they were recorded.

3.2 Dimensional Analysis

The dynamics of the system described in this chapter are governed by five independent non-dimensional parameters. As pointed out in chapter two, the non-rotating cavity flow can be described by the aspect ratio, the Prandtl number and the Rayleigh number defined by equations (2.1), (2.2) and (2.3) respectively. Rotation introduces two additional independent variables and therefore requires two additional non-dimensional parameters. The first variable is the Coriolis parameter f (defined as twice the angular velocity) which has been included in an Ekman number,

$$\mathrm{Ek} = \frac{\nu}{\mathrm{H}^2 f} \ . \tag{3.1}$$

The second additional variable is the width of the cavity, which is not required in the non-rotating case since the flow is then two dimensional. In our case the width is most usefully represented in terms of a rotational Froude number

$$\mathrm{Fr} = \frac{\mathrm{B}^2 f^2}{g\alpha\Delta\mathrm{TH}} \ , \tag{3.2}$$

which is the square of the ratio of the cavity width to the Rossby deformation radius. In Chapter 4 additional *internal* non-dimensional parameters are defined to describe the early development of the flow.

Hence the rotating convection problem can be defined in terms of a five dimensional parameter space, where the dimensions are determined by equations (2.1), (2.2), (2.3), (3.1) and (3.2). This study examined the dependence of the flow on the last three parameters (Ra, Ek and Fr) with A = 0.075 and Pr = 6. Furthermore, we are only interested in the regime in which

$$\mathrm{Ek} < 1. \tag{3.3}$$

If (3.3) is not satisfied, the depth of the Ekman layers is comparable to the fluid depth and the problem reduces to the non-rotating case discussed in Section 2.2. In general, the study will also be restricted to

$$Fr > 1. \qquad (3.4)$$

When the Froude number is less than unity, the width of boundary currents becomes comparable with the cavity width and rotational effects are again suppressed.

Appendix A: calibration of heat flux meters

In each end wall of the convection cavity there were two pairs of thermistors. This configuration will be referred to as a heat flux meter. In order to calibrate the heat flux meters, additional insulation was first placed around the tank. A temperature difference of 10°C (as measured by the thermistor pairs) was then applied between the aluminium and copper by circulating warm water from a bath through one of the end walls. The bath temperature was steadily increased to maintain the 10°C step, while the water in the cavity was stirred as its temperature T was measured. Assuming heat losses to be negligible the heat flux through the end wall is

$$\frac{dH}{dt} = K_T \Delta T = mc\frac{dT}{dt} \qquad (A3.1)$$

where m is the mass of water in the tank, c is the specific heat of water, and K_T is a characteristic constant of the heat flux meter in units of $W°C^{-1}$. The tank temperature T was plotted as a function of time t and $\frac{dT}{dt}$ determined for each heat exchanger (the linearity of these curves indicated that losses were small). Then K_T was determined for each end wall from equation (A3.1). The heat flux through the end walls could then be easily determined from A3.1 by taking a pair of thermistor readings.

During experiments (when the additional insulation was removed) the heat loss through the top and side walls was

$$\left(\frac{dH}{dt}\right)_{Hot} - \left(\frac{dH}{dt}\right)_{Cold} = K_{TH}\Delta T_H - K_{TC}\Delta T_C \approx 0.06 K_{TH}\Delta T_H$$

That is the heat loss was 6% of the longitudinal heat transfer.

CHAPTER 4

THE INITIAL INTRUSIONS

This chapter describes the early convective motions in the cavity, observed immediately after the heating and cooling were initiated. During this period the boundary currents were distinct from the ambient fluid. A general description of the currents is given in Section 4.1, followed by a scaling analysis of their dynamics. In Section 4.3, the temperature structure and alongshore propagation of the currents is considered. Properties of the instabilities are discussed in Section 4.4.

4.1 Description of the Experiments

For each run the tank was filled with water and spun up to solid body rotation, with an angular velocity $f/2$. Each experiment was initiated by commencing the pumping of hot and cold water through the heat exchangers. This process produced end wall temperatures of $T_0 \pm \Delta T/2$ for the hot and cold ends respectively, where T_0 was the initial temperature of the working fluid. As the flow from the hot and cold ends was almost symmetric, it is sufficient to describe the kinematics of the flow which originated from the hot wall. The only asymmetry was a higher buoyancy flux out of the hot thermal boundary layer due to the nonlinear equation of state of water (see Section 5.1).

When heating was initiated a thermal boundary layer rapidly formed adjacent to the heated surface. As yet unaffected by rotation, the buoyant fluid rose vertically and was turned into the interior by the upper horizontal lid. Coriolis forces pushed this current to the right (anti-clockwise rotation) and after a transition distance of the order of the internal Rossby radius, a density current formed along the right-hand wall. When $Ek > 2 \times 10^{-4}$ a bulbous 'head' structure similar those in high Reynolds number lock-exchange experiments (Stern et al. 1982 and Griffiths and Hopfinger 1983) was observed. Conversely, at smaller Ekman numbers the depth of the intrusion increased monotonically from the nose such that the currents did not possess a distinct head structure. Photographs are shown of the temporal development of warm and cold intrusions (Figure

4.1) and of well developed warm intrusions for a range of rotation speeds (Figure 4.2). Figure 4.2 clearly demonstrates that the boundary currents were narrower at higher rotation speeds. This aspect will be discussed further in Sections 4.2 and 4.3 below.

Ten to fifteen rotation periods after the boundary currents were first formed, rotationally induced instabilities developed on their edge some distance behind the nose. These were likely to be mixed mode instabilities with both barotropic and baroclinic components (Section 4.4). When $f < 0.5$ (Ek $> 10^{-4}$ and Fr < 10) the waves were damped, probably by some combination of Ekman layer dissipation and the effects of the finite width of the cavity. At higher rotation rates, however, they broke backwards towards the source of the intrusion, producing cold core cyclonic eddies. If unimpeded by neighbouring eddies, a warm anticyclone formed on the downstream side of the cyclonic eddies to create dipolar eddy pairs. Dye streaks also revealed that eddy structures penetrated into the lower layer, sometimes reaching the bottom of the tank. Neighbouring eddies interacted in a highly non-linear fashion, with like signed vortices coalescing into a single structure and opposite signed vortices coupling to produce 'second generation' dipoles. The net effect of these processes was to spread hot fluid laterally across the tank.

When the intrusion reached the cold end wall it turned and flowed along this boundary, sinking as it cooled. Some of this fluid then became part of the cold boundary current. The coupling of this circulation with the rotational instabilities transferred heat and momentum throughout the fluid (discussed in Chapter 5), until eventually a steady mean state was reached. Eddies were then prominent throughout the cavity and the mean flow was determined by potential vorticity constraints. A detailed account of the steady

---

Figure 4.1 A plan view of the development of the warm and cold boundary current when $f = 1.0s^{-1}$ and $\Delta T = 16^{o}C$. The hot current flows from the right hand end wall along the underside of the lid, while the cold current flows from the left along the bottom. The number of rotation periods since the commencement of heating and cooling is displayed at the bottom of the figure. The tank rotation is anti-clockwise.

Figure 4.2 Plan views of the warm boundary currents for rotation rates of $f = 0.1$, 0.5, and $2.0s^{-1}$ respectively with $\Delta T = 16^{o}C$.

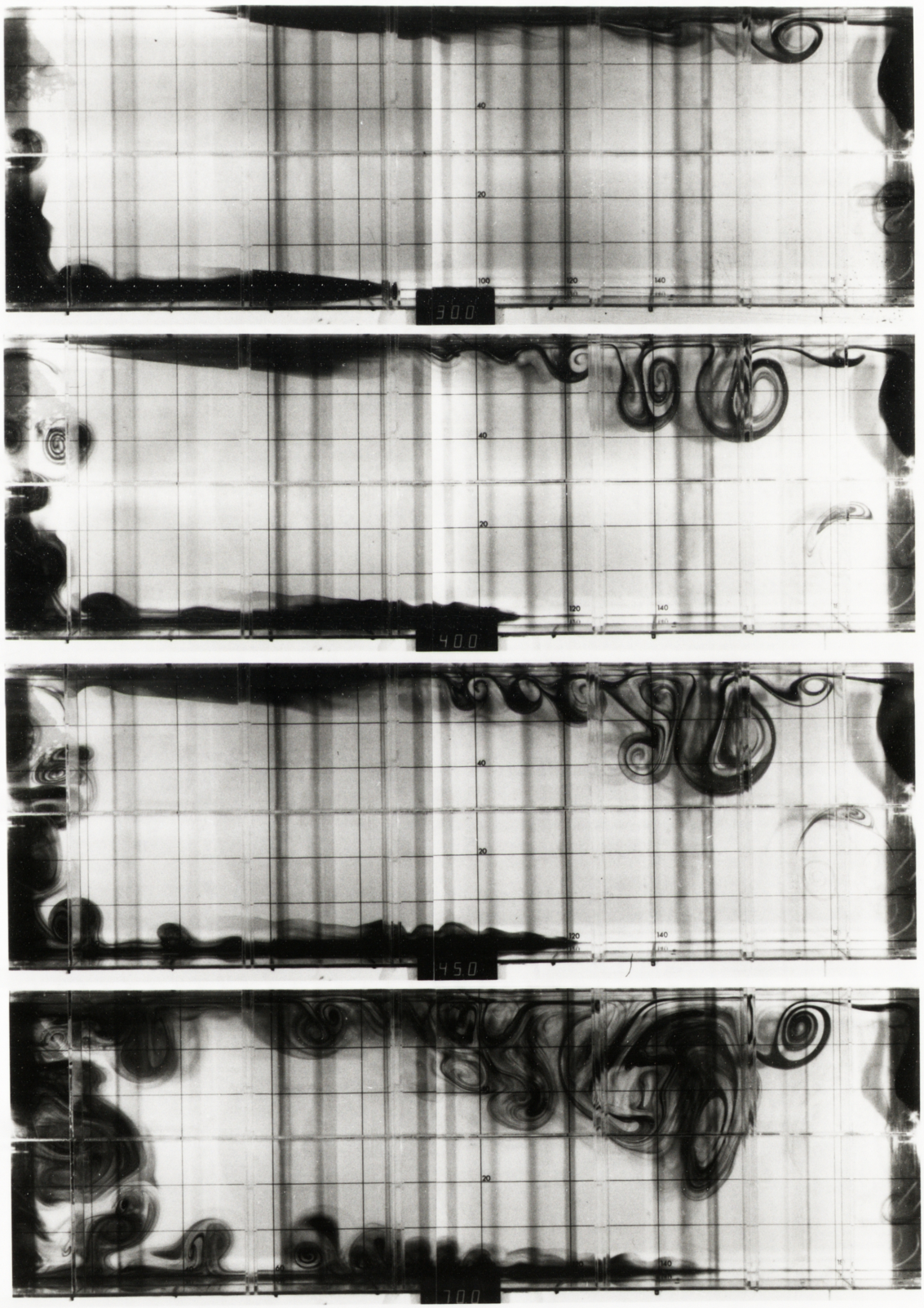
40
20
100
120
140
30.0
40
20
120
140
40.0
40
20
120
140
45.0
20
140
70.0

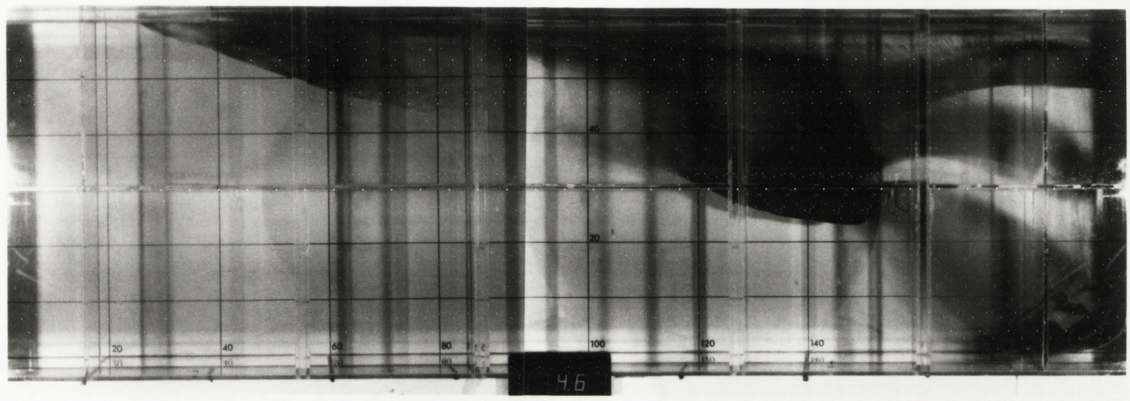
4.6

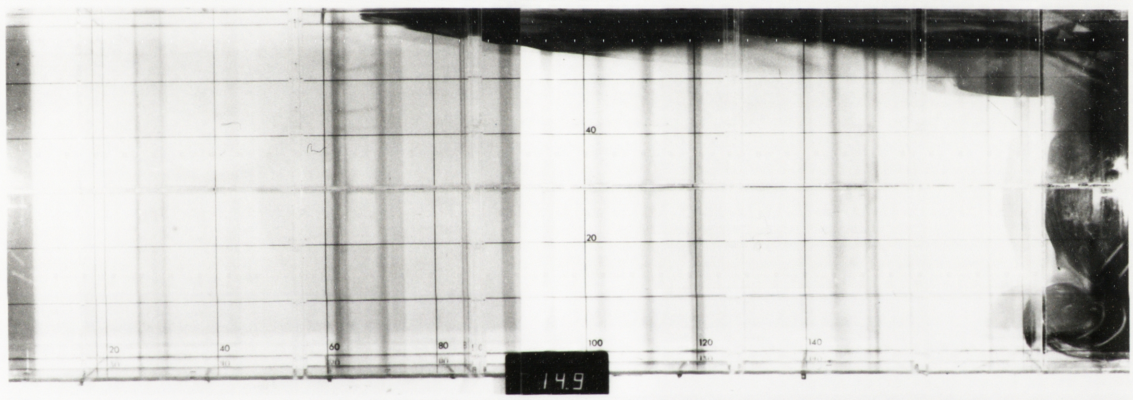
14.9

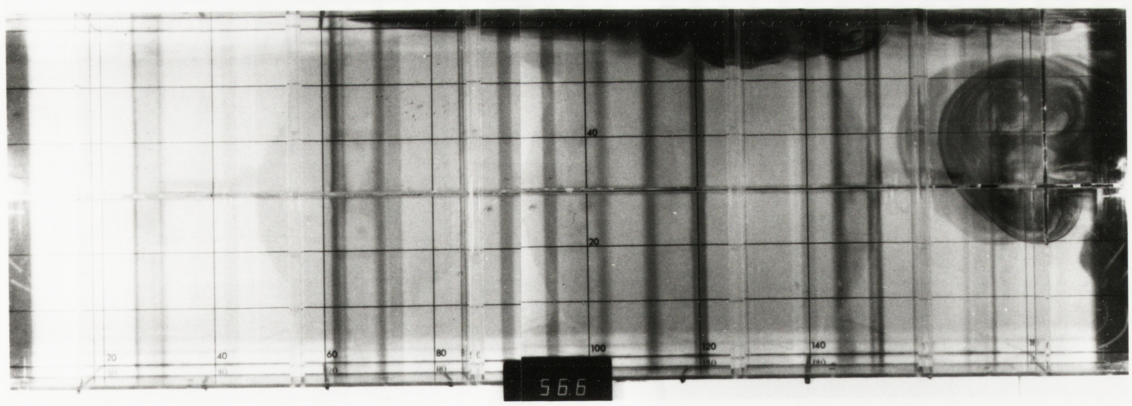
5.6.6

flow will be given in a Chapter 6. This chapter looks at the early period of the experiments, in which the intrusion was still distinct from the surrounding fluid ($\lesssim 100$ rotation periods).

4.2 Analysis of the Initial Intrusion

A simple scaling analysis can be used to determine the force balances operating in the experiment before instabilities became prominent. It will be shown that much of the dynamics of the intrusion can be described in terms of an internal Ekman number, defined by the relation

$$Ek_i = \frac{\nu}{h^2 f}, \tag{4.1}$$

where ν is the kinematic viscosity and h is the depth scale of the intrusion. Although it is not usual to include a dependent variable (in this case h) in the definition of a dimensionless parameter, this form of the Ekman number was found to be physically the most appropriate. Results in this form are also more relevant to previous studies of rotating boundary currents, such as Stern et al. 1982 and Griffiths and Hopfinger 1984 which also included scaling based on the local depth of the intrusions. The dependence of h on the independent variables will be discussed in Section 4.3 below.

The density of the ambient fluid is denoted by ρ and the pressure by p. The x direction is defined as parallel to the adiabatic side walls and directed from the hot to the cold end of the basin. The y co-ordinate is normal to these side walls and the z co-ordinate is vertical, while the corresponding velocity components are (u,v,w) respectively. The components of the momentum equation which describe the system are:

$$\begin{aligned}
\frac{Du}{Dt} - fv &= -\frac{1}{\rho}\frac{\partial p}{\partial x} + \nu\nabla^2 u, \\
\frac{Dv}{Dt} + fu &= -\frac{1}{\rho}\frac{\partial p}{\partial y} + \nu\nabla^2 v, \\
\frac{Dw}{Dt} &= -\frac{1}{\rho}\frac{\partial p}{\partial z} + \nu\nabla^2 w + g'.
\end{aligned} \tag{4.2}$$

where $g'=g\alpha(T-T_0)$ is the reduced gravity, α is the coefficient of thermal expansion and T is the local temperature.

If the flow is assumed to be parallel to the side boundary then the x component of the momentum equation for the flow within the intrusion, but outside the viscous boundary layers, can then be expressed as

$$\frac{Du}{Dt} = -\frac{1}{\rho}\frac{\partial p}{\partial x} - (\tfrac{1}{2}\nu f)^{1/2}\frac{\partial u}{\partial z}. \tag{4.3}$$

The last term parameterizes the dissipation of momentum due to the Ekman layer beneath the fixed lid (Gill 1982 p331). Elsewhere, viscous dissipation is negligible provided $Ek < 1$. The cross-stream and vertical components of the momentum equation are assumed to be given by the geostrophic and hydrostatic approximations

$$fu = -\frac{1}{\rho}\frac{\partial p}{\partial y}, \tag{4.4}$$

$$0 = -\frac{1}{\rho}\frac{\partial p}{\partial z} + g', \tag{4.5}$$

The longitudinal pressure gradient term in equation (4.3) represents the buoyancy driving of the flow and therefore can always be assumed to be significant. Comparing the inertial and Ekman dissipation terms in (4.3) indicates that the inertial term will dominate for times less than the spin-down time

$$\tau_s \sim \frac{h}{(\tfrac{1}{2}\nu f)^{1/2}}. \tag{4.6}$$

Therefore, when $t < \tau_s$ the along shore balance is between buoyancy and inertial terms. This gives the internal wave speed as a velocity scale

$$U \sim Nh, \tag{4.7}$$

while (4.4) and (4.5) imply that the cross-stream width b scales with the internal Rossby deformation radius R:

$$b \sim R = \frac{Nh}{f}. \tag{4.8}$$

where the buoyancy frequency is defined by the relation $N = (g\alpha\partial T/\partial z)^{1/2}$. Equation (4.8) can alternatively be expressed as a scale for the slope of isotherms within the current

$$\frac{\partial h}{\partial y} \sim \frac{h}{R} \sim \frac{f}{N}. \tag{4.9}$$

For times larger than the spin-down time, the scaling indicates that the inertial term will be smaller than the Ekman dissipation term, leaving a balance between buoyancy and Ekman dissipation. The velocity and cross-stream length scales after the transition are given by

$$U \sim Ek_i^{-1/2} \left(\frac{N^2h^2}{f}\right) x^{-1} \tag{4.10}$$

and

$$b \sim Ek_i^{1/2}\, x. \tag{4.11}$$

These are overall scales for the flow and are not necessarily applicable near the nose of the intrusion. A balance between buoyancy and inertia may persist in this region until the flow changes to a viscous intrusion. However, if momentum is dissipated over most of the intrusion length the volume transport into the nose region will be reduced. The depth of the head will subsequently decrease with a corresponding fall in nose velocity.

Instabilities are observed on the edge of the current when it is approximately ten rotation periods old. These instabilities introduce significant cross-stream mass and momentum transfer, which may reduce the volume flux into the nose region and thus cause a reduction in nose velocity. Eddies may also produce drag by coupling with the lower layer which, for a baroclinic flow, would be traveling in the opposite direction to the boundary current. If we assume that these decay mechanisms will dominate after eddies have had time to develop (~10 rotation periods), then the intermediate Ekman dissipation regime will play a significant role only if the spin-down time is less than order ten rotation periods. This condition corresponds to

$$Ek_i > 10^{-4}. \tag{4.12}$$

If (4.12) is not satisfied, the intrusion may pass from a buoyancy-inertial balance directly to a regime in which buoyancy is balanced by an eddy drag.

The analysis can be extended to take into account the dimensions of the cavity. Dissipation in Ekman layers will play a significant role within the cavity length only if the advective time-scale L/Nh is greater than the spin-down time. This implies that

$$Ek_i > Fr_i^{-1} \tag{4.13}$$

where the internal rotating Froude number is defined by the relation

$$Fr_i = \frac{L^2}{R^2} = \left(\frac{fL}{Nh}\right)^2. \tag{4.14}$$

Therefore, Ekman dissipation will be important only if both (4.12) and (4.13) are satisfied. Alternatively, for instability induced drag to be important before the intrusion reaches the end of the tank, L/Nh must be greater than ~10 rotation periods. This in turn requires that

$$Fr_i > 10^4. \tag{4.15}$$

The predictions of the scaling analysis can be conveniently summarized in the following form. The intrusion will propagate under an inertial-buoyancy balance over the entire cavity length if

$$\max\{Ek_i, 10^{-4}\} < Fr_i^{-1}. \tag{4.17}$$

The inertial regime is followed directly by a flow dominated by the drag associated with rotational instabilities provided

$$\max\{Ek_i, Fr_i^{-1}\} < 10^{-4}. \tag{4.18}$$

Alternatively when

$$\max\{Fr_i^{-1}, 10^{-4}\} < Ek_i, \tag{4.19}$$

the inertial regime is followed by a period dominated by Ekman dissipation and then another dominated by the instability drag.

4.3 Experimental Results

In this section, the thermal structure of the flow is examined. The alongshore propagation of the current is then considered, including a comparison with some of the scaling arguments in Section 4.2.

The temperature structure of the boundary currents was investigated using a rack of 15 fast response ($\sim 10^{-2}$sec) thermistors at 2.0cm horizontal spacings. This configuration was mounted on a traversing mechanism 85cm from the heated end wall. The traversing speed was 1.0cms^{-1} and temperatures were recorded every 0.1s. Cross-stream profiles covering half the width of the cavity where recorded regularly, throughout the duration of each experiment. The profile obtained from the first thermistor (1.0cm from the side wall) was used to measure the temperature gradient and depth h (see Figure 4.3 for a precise definition of these quantities). The precise position at which $\partial T/\partial z$ was measured was not critical, since this quantity was relatively constant across the width of the current. On the other hand, the depth was essentially the maximum depth of the boundary current at that particular cross-section.

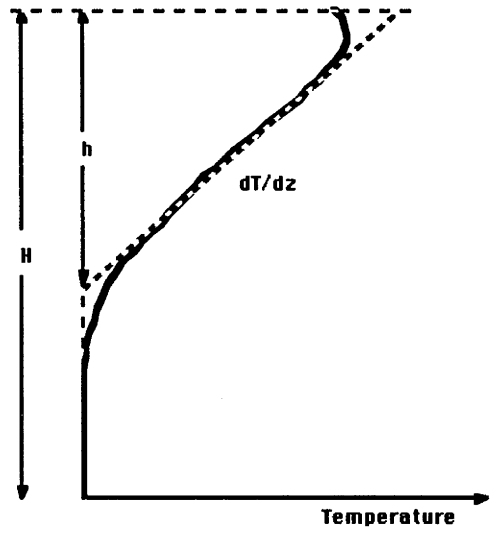

Figure 4.3 Typical vertical temperature structure of the flow next to the right hand boundary. This illustrates how both the temperature gradient and depth of the current were defined.

Typical cross-sections of the temperature structure of the boundary currents are shown in Figure 4.4 for a range of rotation rates. The intrusion took a wedge-shaped form which was constrained more tightly to the side boundary as the rotation rate was increased. The shape of the cross-sections of the currents can generally be approximated by the hyperbolic form $h(y) \propto 1 - (\cosh y/R)/(\cosh b/R)$ predicted by Griffiths and Linden (1982) for a flow of uniform potential vorticity. An average depth of the intrusion $\hat{h}$ can then be defined by $\hat{h} = b^{-1}\int h(y)dy = 0.7h$. In many instances the average depth was more relevant in making comparisons with earlier work. Figure 4.5 illustrates how the geostrophic constraint was broken by instabilities and the subsequent cross-stream spreading by eddies. The latter profiles (4.5c and 4.5d) include an anti-cyclonic eddy whose core took the lens shaped form observed in ocean eddies (Robinson 1983).

Since the depth and vertical temperature gradient were included in the definition of the parameters Ek and Fr which describe the flow, it is important to describe the dependence of those quantities on the independent variables ΔT and f. Firstly, the temperature gradient was found to be well represented by $\partial T/\partial z \approx \Delta T/4h$, leaving only the dependence of h to be determined. An analysis by Condie and Ivey (1986) in which both dissipation and instability were neglected, indicated that the depth scaled as $h \sim (B^4H^3\kappa^3/g^3\alpha^3\nu)^{1/8}(f^{1/2}/\Delta T^{3/8})$. However, over the relatively small range of temperature differences examined (ΔT=12 to 24°C) there was no significant variation in h. Furthermore, when f was increased by a factor of 20 (f=0.1 to 2.0s^{-1}), h only

---

Figure 4.4 (Top) The cross-stream temperature structure of the warm boundary currents before instabilities appeared at the position of the thermistors (x = 85cm) for $\Delta T = 8°C$. Cross-sections correspond to f = 0.1, 0.5, 1.0, and 2.0s^{-1} respectively. Isotherms are at 0.5 C intervals while the area over which the profiles were taken is 15cm high (the full height of the cavity), 20cm wide (one third of the width of the cavity) and adjacent to the right hand side boundary.

Figure 4.5 (Bottom) Development of the temperature structure of the warm intrusion with time (f = 1.0s^{-1}, $\Delta T = 8°C$). The cross section is the same as that in Figure 4.4 (x = 85cm). Cross sections were recorded at 27, 42, 69, and 91 rotation periods after heating commenced. The approximate stage of development of the current for each profile can be determined by referring to the photographs in Figure 4.1.

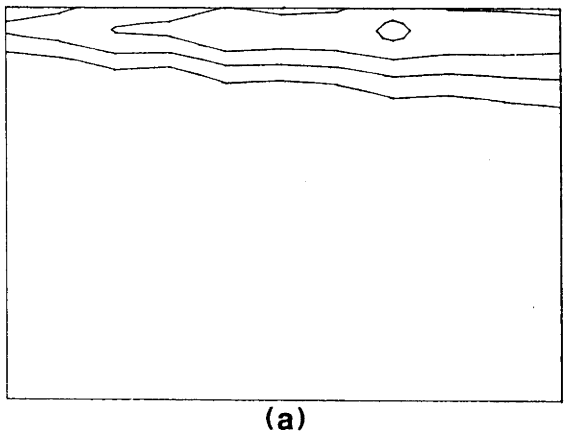

(a)

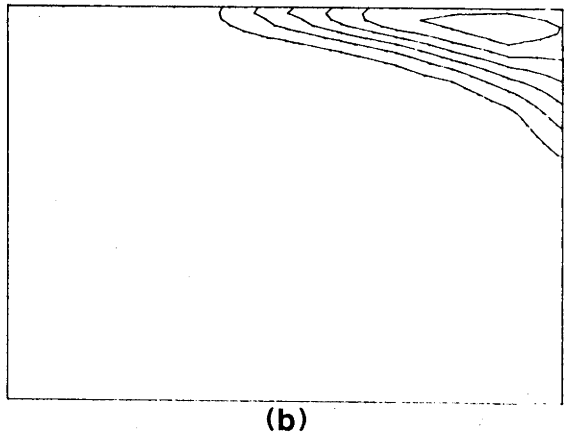

(b)

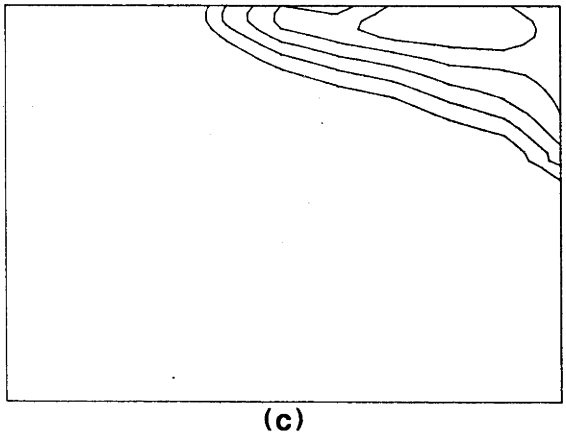

(c)

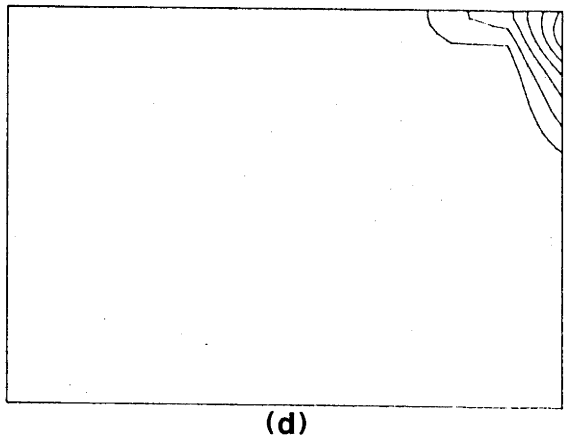

(d)

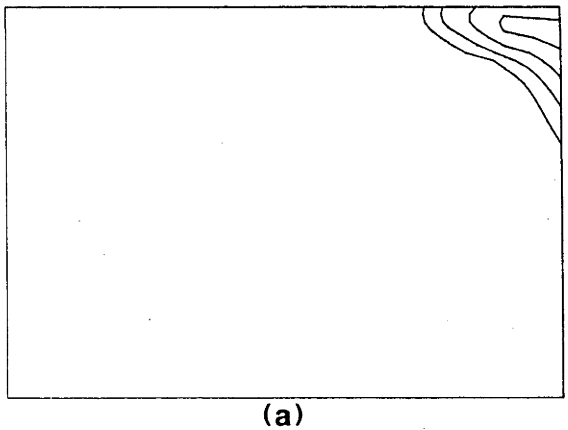

(a)

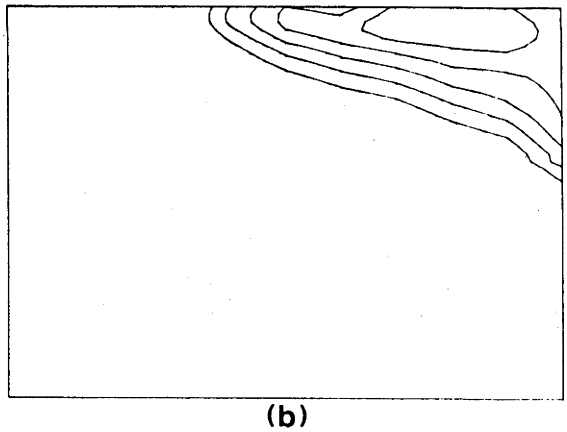

(b)

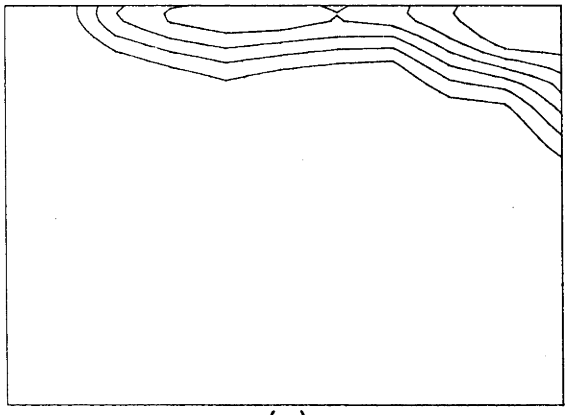

(c)

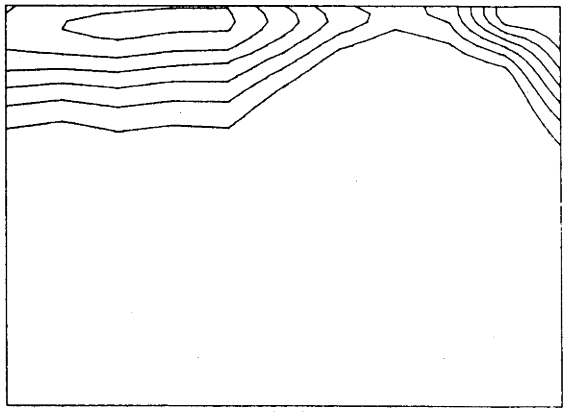

(d)

increased from 6 to 9cm. These limited observations suggest that the finite depth of the cavity may have influenced the current depth.

As a measure of the current width, the distance of a given isotherm from the side wall was recorded as a function of time from the temperature profiles. The temporal development of the width (non-dimensionalized by the internal deformation radius given in equation 4.8) is illustrated by Figure 4.6. This begins with an initial adjustment period of approximately ten rotation periods. From 10 to 40 rotation periods the current width is relatively constant. Within this time interval the surface width of the isotherm 0.5°C above ambient (where the maximum temperature within the current is 4°C above ambient) is given by b/R= 2.4±0.5 (Figure 6a). During this period each isotherm for each rotation rate exhibited a similar trend. After 40 rotation periods photographic records reveal that instabilities became visible at the position of the thermistors (x=85cm). From this point the non-dimensional width shows a great deal of variation due to the instabilities.

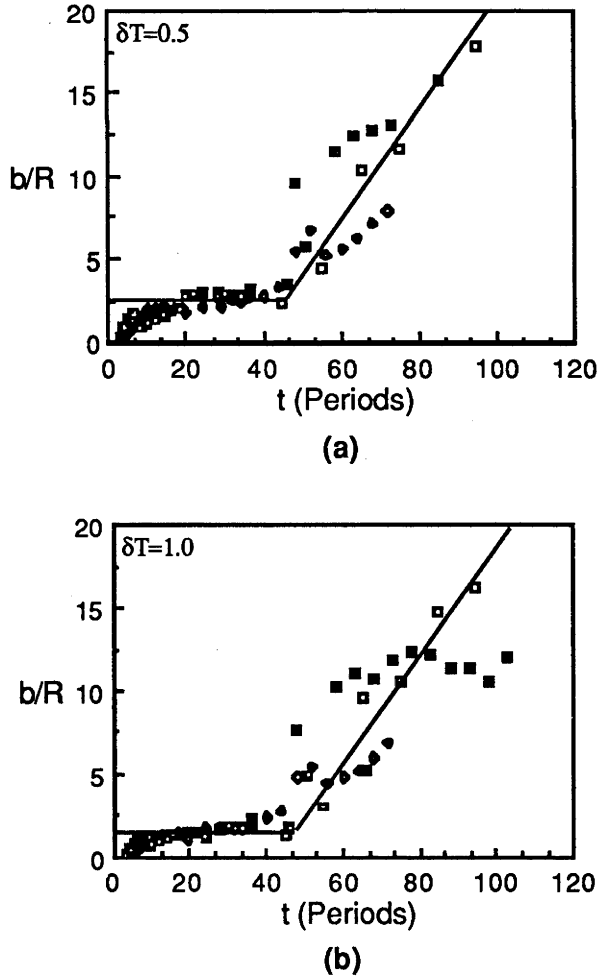

Figure 4.6 (Caption appears on following page).

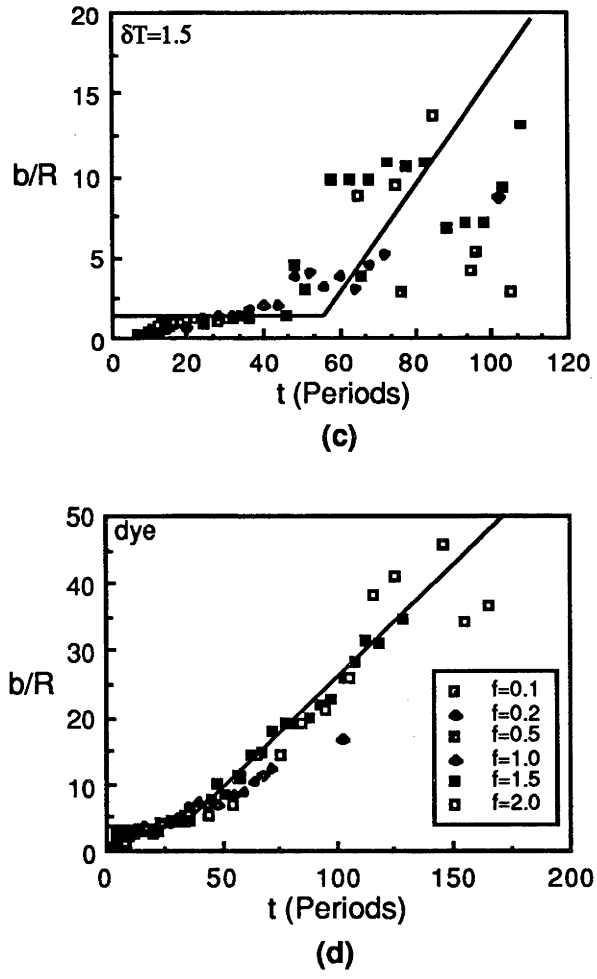

Figure 4.6 Non-dimensional width of the intrusion (at x = 85cm) as a function of time for Ra = 8.7×10^8. The width is defined for the first three graphs as the distance from the boundary to the chosen isotherm ($\delta T = 0.5^oC$, 1.0^oC, and 1.5^oC above ambient temperature for (a), (b) and (c) respectively where the maximum δT in the intrusion is 4.0^oC). Graph (d) corresponds to the width of the dye cloud and includes the definition of the symbols.

The trends of the previous paragraph are consistent with measurements of the width of the dye clouds at the same cross-section (Figure 4.6d). These data are more extensive than the temperature measurements since the latter are restricted to half the width of the tank. The stable period ($t < 40$ rotation periods) corresponds to $b/R = 3.22 \pm 0.30$ for the dye cloud, while the eddy induced spreading ($t > 40$ rotation periods) is well represented by $\partial b/\partial t = 0.33$ deformation radii per period. Similar measurements over the length of the cavity yielded the spatial distribution of the cross-cavity transport. The mean cross cavity velocity at the surface (between $t = 40$ and $t = 150$ rotation periods), as determined by the spreading of dye clouds, is graphed in Figure 4.7 as a function of the position along the cavity. There was relatively little

transport near the hot and cold end walls, however, it was quite substantial in the central region of the tank. This distribution will be explained in Chapter 6.

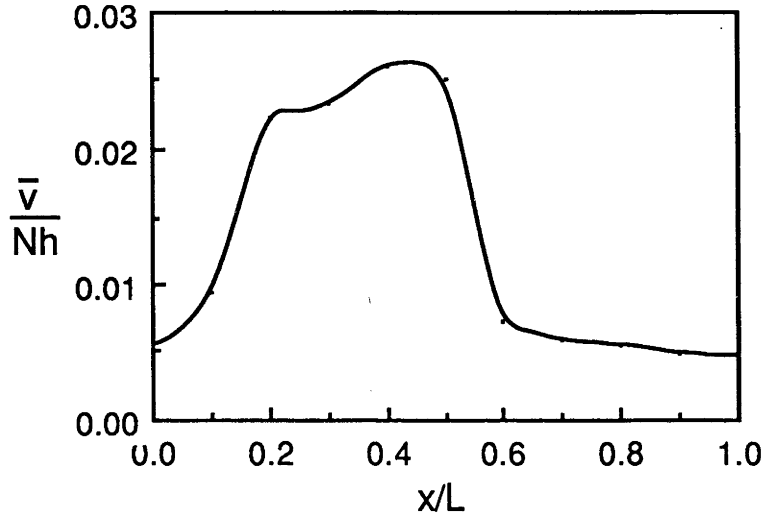

Figure 4.7 The cross cavity mean velocity distribution for the hot intrusion as a function of distance along the cavity. Each data point was determined by plotting the position of the warm front (as defined by the spreading of the dye cloud) at the appropriate value of x, as a function of time. For the non-dimensionalization used in the figure, the data from runs with different conditions collapsed onto a single line. The best fit slope of this line gave a non-dimensional cross cavity velocity representative of all the parameter range except Fr < 1.

While boundary current width measurements form a valuable comparison with satellite images (see for example Griffiths and Pearce 1985), the slope of isopycnals within the current is a more accessible statistic to ship based oceanographers. Therefore, for each profile the slopes of isotherms (at 0.5°C intervals) were measured and averaged. Isotherm slopes (non-dimensionalized in accordance with equation 4.9) are plotted as a function of time in Figure 4.8. The slopes can be measured when the isotherms are fairly linear, but not when the temperature structure is more complex (for example Figure 4.5d). While the data are thus restricted to relatively short times, the trends are consistent with the width measurements. After an initial adjustment period ($t \leq 10$ rotation periods) the isotherm slope remained relatively constant from 10 to 40 rotation periods and within this interval $\partial h/\partial y = (0.28 \pm 0.08) f/N$. The values for f=0.1 are anomalously low, perhaps reflecting the influence of the opposite side boundary when Fr < 1. After 40 periods the intrusions spread by the action of eddies, resulting in a further flattening of the isotherms.

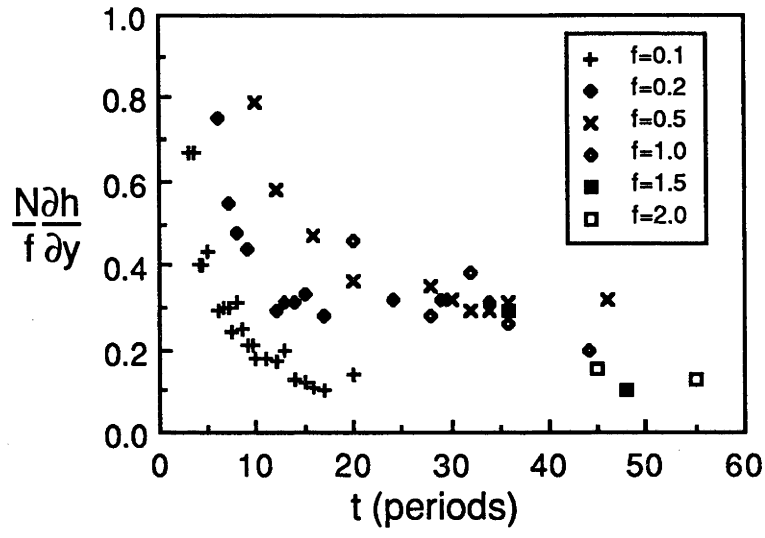

Figure 4.8 The slope of isotherms as a function of time for a range of f.

Some of the scaling predictions made in Section 4.2 were tested by examining the propagation of the head of the intrusion. The distance x the intrusion traveled along the tank was measured as a function of time for a range of rotation speeds. This length was plotted as a function of time t' after the commencement of the experiment for each rotation rate and a virtual time origin t_0 defined such that t=0 when x=0, where $t=t'-t_0$. The non-dimensionalised nose position is plotted as a function of non-dimensional time in Figure 4.9. For each rotation rate the initial motion involved a constant nose velocity, consistent with an inertial buoyancy balance. The initial nose velocity also increased with rotation rate. An increase in rotation rate caused a deepening of the intrusion depth, resulting in greater buoyancy forces and the higher velocities observed (as described by equation 4.7).

Figure 4.9 also reveals a decay of the nose velocity. This effect was more acute, and occurred earlier, at high rotation rates. As the temporal range of the data was insufficient to quantify the decay, further observations were made. Dye streaks released ahead of the intrusion revealed neither communication with the approaching end wall nor the presence of inertial waves. Furthermore, temperature measurements at different locations along the side wall revealed that losses in buoyancy due to mixing near the front could only account for a velocity drop of five to ten percent. This left the two decay

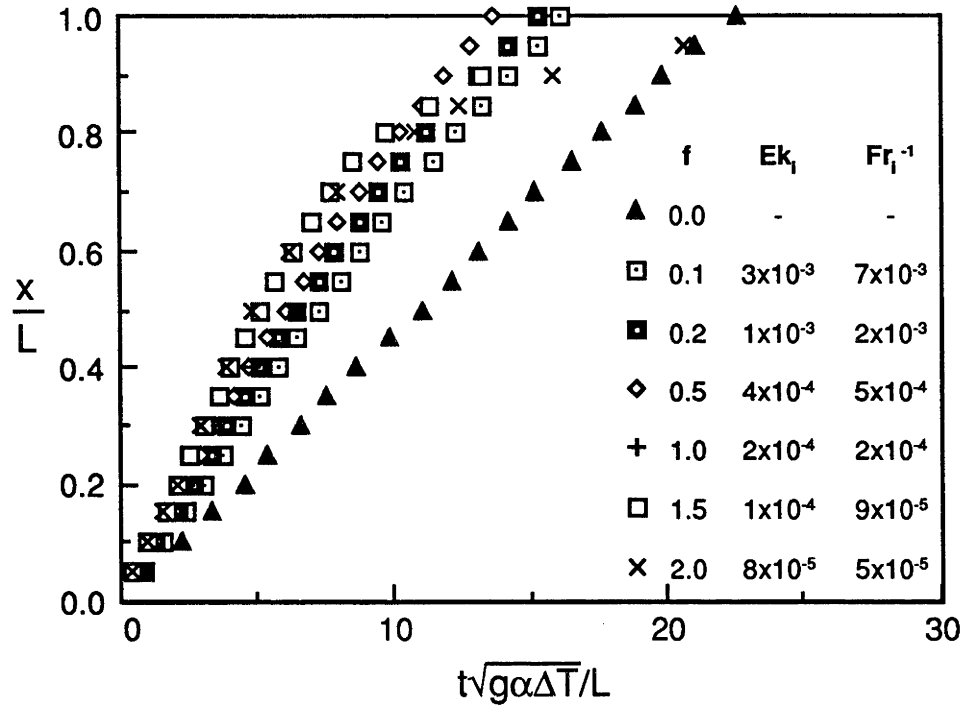

Figure 4.9 The position of the nose of the intrusion nondimensionalized by the length of the cavity, as a function of time t. Time is nondimensionalized by a term representative of the forcing by the heated and cooled end walls. In all runs shown here Ra = 8.7×10^8.

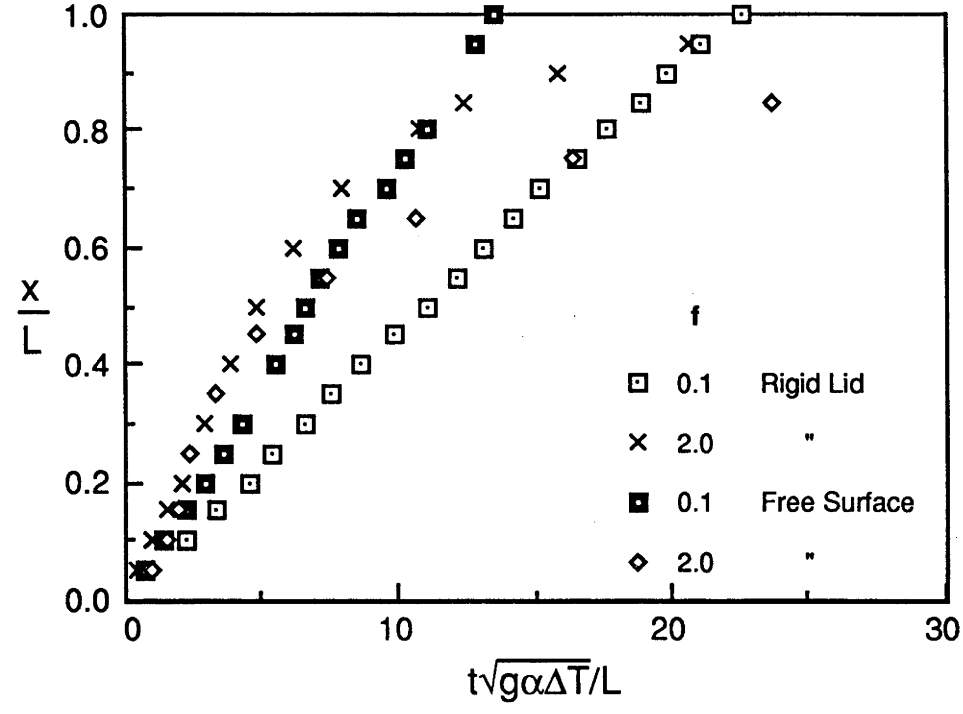

Figure 4.10 The nose position as a function of time for both fixed lid and free surface experiments (Ra = 8.7×10^8).

mechanisms discussed in Section 4.2: the dissipation of momentum by Ekman pumping and the essentially inviscid drag associated with the formation of eddies.

A second series of experiments was conducted to identify the dominant decay mechanism. This involved a slight reduction in fluid level in the cavity so as to produce a free surface. Results for f=0.1s^{-1} and f=2.0s^{-1} for both fixed lid and free surface experiments are shown in Figure 4.10. At the low rotation rate ($Ek_i = 3x10^{-3}$) the initial velocity was higher and the decay almost absent when using a free surface. This result indicates that any velocity decay observed with a fixed lid at this Ekman number was due to Ekman layer dissipation. These observations are consistent with the scaling analysis results in Section 4.2. On the other hand, intrusions in experiments with a higher rotation rate ($Ek_i = 8x10^{-5}$) underwent a more rapid velocity decay with a free surface than with a fixed lid. It was also observed that the growth rates of instabilities was greater in the free surface cases (as a result of less Ekman dissipation). Those two observations suggest that the drag at this smaller Ekman number was that associated with the growth of instabilities as predicted in Section 4.2 (equation 4.18).

Thus to summarise, the experiments like the theory suggest two regimes of propagation. When $Ek_i > 10^{-4}$ the velocity decay resulted from dissipation within the Ekman layer. Conversely, when $Ek_i < 10^{-4}$ transfer of mass and momentum away from the boundary by waves and eddies reduced the alongshore velocity by decreasing the buoyancy flux into the nose region. Within the latter regime eddies may have also supplied additional drag by coupling with the lower layer.

4.4 Instabilities

Rotationally induced instabilities can have a very significant influence on boundary currents. The previous section demonstrated their role in broadening the intrusion and in the decay of the nose speed. We now examine some specific characteristics of those structures such as wavelengths, phase-speeds and growth rates, with emphasis on the small amplitude behaviour. At larger amplitudes, waves and eddies interacted in a highly non-linear fashion, making quantitative measurements difficult to interpret.

Wavelengths of small amplitude instabilities were estimated from photographs of the dyed intrusion for a range of rotation rates. The wavelength is here defined as the distance between finite amplitude perturbations on the edge of the current and is non-dimensionalized by $2\pi R$ where R is the local value of the internal Rossby radius (defined by equation 4.8). This is plotted as a function of the Froude number in Figure 4.11. The graph confirms that the wavelength scaled with the deformation radius. When Fr = 260, perturbations on the edge of the current grew and interacted very quickly, making small amplitude measurements difficult and hence produced a large degree of scatter in the data. Taking an average of the remaining points gives $\lambda/2\pi R = 0.83\pm0.11$ or alternatively $\lambda/2\pi\hat{R} = 1.19\pm0.16$ where $\hat{R} = N\hat{h}/f$.

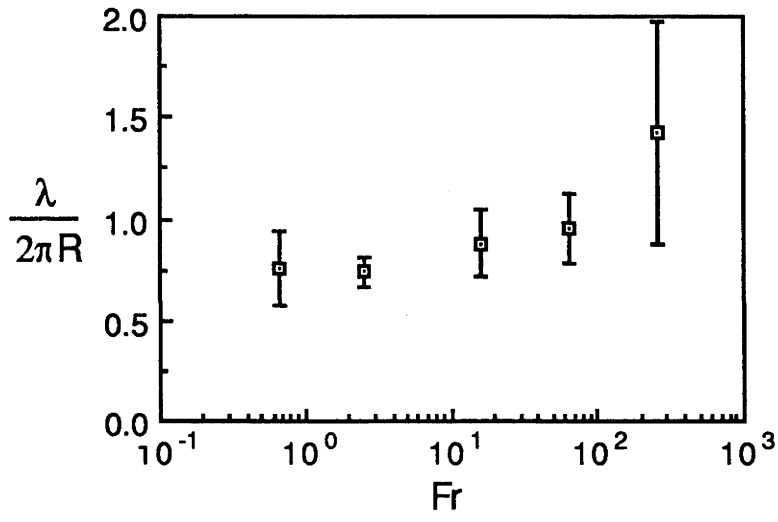

Figure 4.11 The wavelength of instabilities as a function of Froude number. The error bars represent one standard deviation based on from five to nine measurements (for each Fr value) taken at different times and positions in the tank.

Wavelengths based on the average intrusion depth are the more appropriate for comparison with earlier studies of two layered flows in which the deformation radius represented a geometric mean for the two layers. The value given in the previous paragraph is similar to the experimental values of 1.1±0.3 found by Griffiths and Linden (1982), 1.16±0.27 by Chia et al. (1982) and 1.14 by Narimousa and Maxworthy (1987). It is also in agreement with the theoretical figure of 1.15 derived by Killworth et al. (1984) for waves which extract energy from both the vertical and horizontal velocity

shears. Thus, while the wavelength was well defined and in agreement with previous measurements, it is not a reliable indicator of the energy conversions taking place. Like the instabilities in the Killworth et al. model, the laboratory waves may have had both baroclinic and barotropic components.

Perturbations on the edge of the currents were advected along at finite phase velocities. However, as indicated in Figure 4.12, these velocities were much less than fluid velocities within the intrusion which were typically of the order of the internal wave speed Nh. The theoretical values of Killworth et al. (1984) for a similar current are also illustrated in Figure 4.12. The experimental phase speeds are typically one third of the theoretical values.

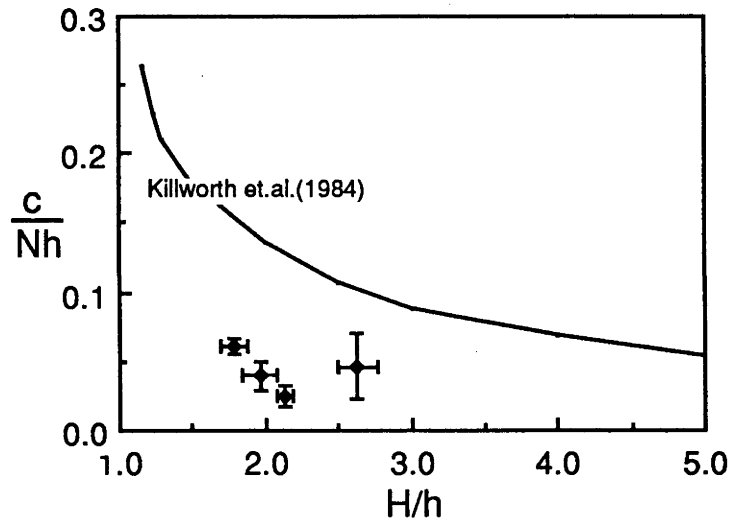

Figure 4.12 The phase speed of small amplitude instabilities as a function of the depth ratio H/h. Also shown is the theoretical curve predicted by Killworth et al.(1984).

Some discrepancy between the theory and experiment was expected, since Killworth et al. (1984) assumed that there was no mean flow in the lower layer. In the experiments, however, the intrusion caused a significant shallowing of the lower layer. In order to conserve potential vorticity in this layer, a counter flow was produced beneath the boundary current. This counter current was clearly observed during the experiments using the thymol blue technique. Since waves interacted with the lower layer, the counter flow would have reduced their forward propagation. Large amplitude eddies, which also

must have strongly interacted with the lower layer, had no observable phase velocity. Any movement of these structures was generally not parallel to the boundary and resulted from interactions with other eddies.

The growth rates of waves were also examined. This involved tracking individual waves on photographic records and measuring their cross-stream amplitude ε before they broke or interacted with other waves or eddies. The dominant growth behaviour observed during this period was linear. No evidence was found for the exponential growth predicted by linear stability analysis suggesting that this behaviour had ceased before the instabilities where large enough to be observed. The growth rate during the linear growth period is plotted as a function of Froude number in Figure 4.13. Although there is generally a small increase in growth rate with Fr the trend is hardly significant when errors are taken into account. Taking an average of the data points gives a non-dimensional growth rate for waves beneath a rigid lid of $\varepsilon/fR = 0.016 \pm 0.005$. If we assume that the linear behaviour dominated throughout the growth of a wave, then a timescale for the growth can be defined as $\lambda/\varepsilon = 26 \pm 11$ rotation periods.

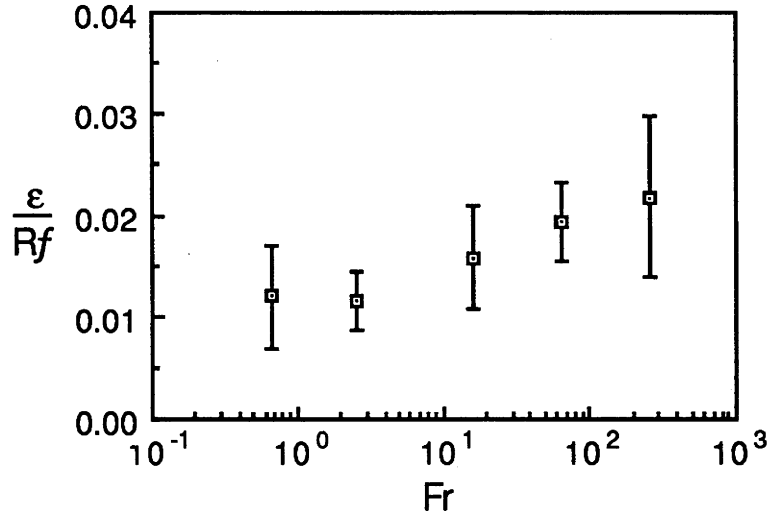

Figure 4.13 The non-dimensionalized growth rate of small amplitude instabilities as a function of Froude number.

After waves had grown to large amplitude they generally broke to form eddies. However, at low rotation speeds the waves were damped and failed to break (see for

example the top photograph in Figure 4.2). Since eddies can substantially influence the flow, it is important to identify the conditions under which breaking occurred. The presence of the side boundary opposite the current may have damped the wave growth. Waves were observed to break (within 100 rotation periods) only when the wavelength $2\pi R$ was less than the width of the cavity. Dissipation may also have played a significant role in preventing breaking and the experiments indicated that breaking only occurred when $Ek < 10^{-4}$. These results may be relevant to partially enclosed water bodies such as gulfs and straits.

4.5 Conclusions

Study of early convective motions in the cavity revealed a number of important features. The currents initially propagated under an along-shore inertial-buoyancy balance and a geostrophic cross-stream balance. After 10 to 15 rotation periods rotational instabilities formed on the edge of the currents. The growth of these structures resulted in a spreading of the flow away from the boundary. At a given cross-section this spreading was roughly linear with time. For small Ekman numbers ($Ek < 10^{-4}$) and large Froude numbers ($Fr > 10$) the waves produced dipolar eddy structures which coupled with the lower layer. Results indicate that this process slowed the advance of the intrusion. At these small Ekman numbers, the net effect of the Ekman layer beneath the rigid lid was to slow the growth of instabilities, thus *reducing* the decay in the alongshore velocity of the intrusion. On the other hand, at higher Ekman numbers the waves did not break and dissipation in the Ekman layer was directly responsible for any velocity decay. Careful measurements of the instabilities gave quantitative estimates for the wavelength, phase speed and growth rate at small amplitudes. These results will be compared with ocean data in Chapter 7.

CHAPTER 5

EVOLUTION TO STEADY STATE

In Chapter 4 the initial motions observed in the cavity were described ($t < 100$ rotation periods). This chapter continues the description of the transient behaviour, up to steady state. Section 5.1 examines the evolution of the velocity and temperature fields and in Section 5.2 the timescales for development of stratification in the cavity are determined. The steady state flow itself will be examined in Chapter 6.

5.1 Development of the Flow Field

The long term evolution of the flow was studied with the aid of temperature sections. A rack of fifteen equally spaced thermistors spanned the width of the cavity. Cross-sectional profiles were recorded at regular intervals throughout the development of the flow, at four positions along the length of the tank. Examples of these profiles in Figure 5.1 show the development of the temperature field for a single set of conditions. This type of data was used along with observations of the dye streaks released at the end walls, to determine how the flow developed. The description which follows is for the conditions in Figure 5.1; however the basic character of the flow was similar provided $Fr > 1$. As the Froude number was increased, horizontal length scales, such as the width of strong current regions and diameter of eddy structures, decreased.

Column (a) in Figure 5.1 shows the temperature structure at the four cross-sections in the cavity (viewed from the heated end), 50 rotation periods after the heating and cooling were applied. As described in Chapter 4, warm and cold intrusions, with almost linear internal stratification, flowed with a side boundary on their right hand side.

Figure 5.1 Cross-sections of the temperature structure in the cavity when $Ra=2.1\times10^{9}$, $Ek=2.4\times10^{-5}$ and $Fr=71.0$. The cross-sections are viewed from the hot end and isotherms are at $1.0^{o}C$ intervals. The columns correspond to (a) t=50, (b) t=100, (c) t=200 rotation periods and (d) steady state, while the rows correspond to x/L=0.28, 0.43, 0.65 and 0.80 respectively (where x is measured from the hot end wall). The directions of strong currents are also indicated.

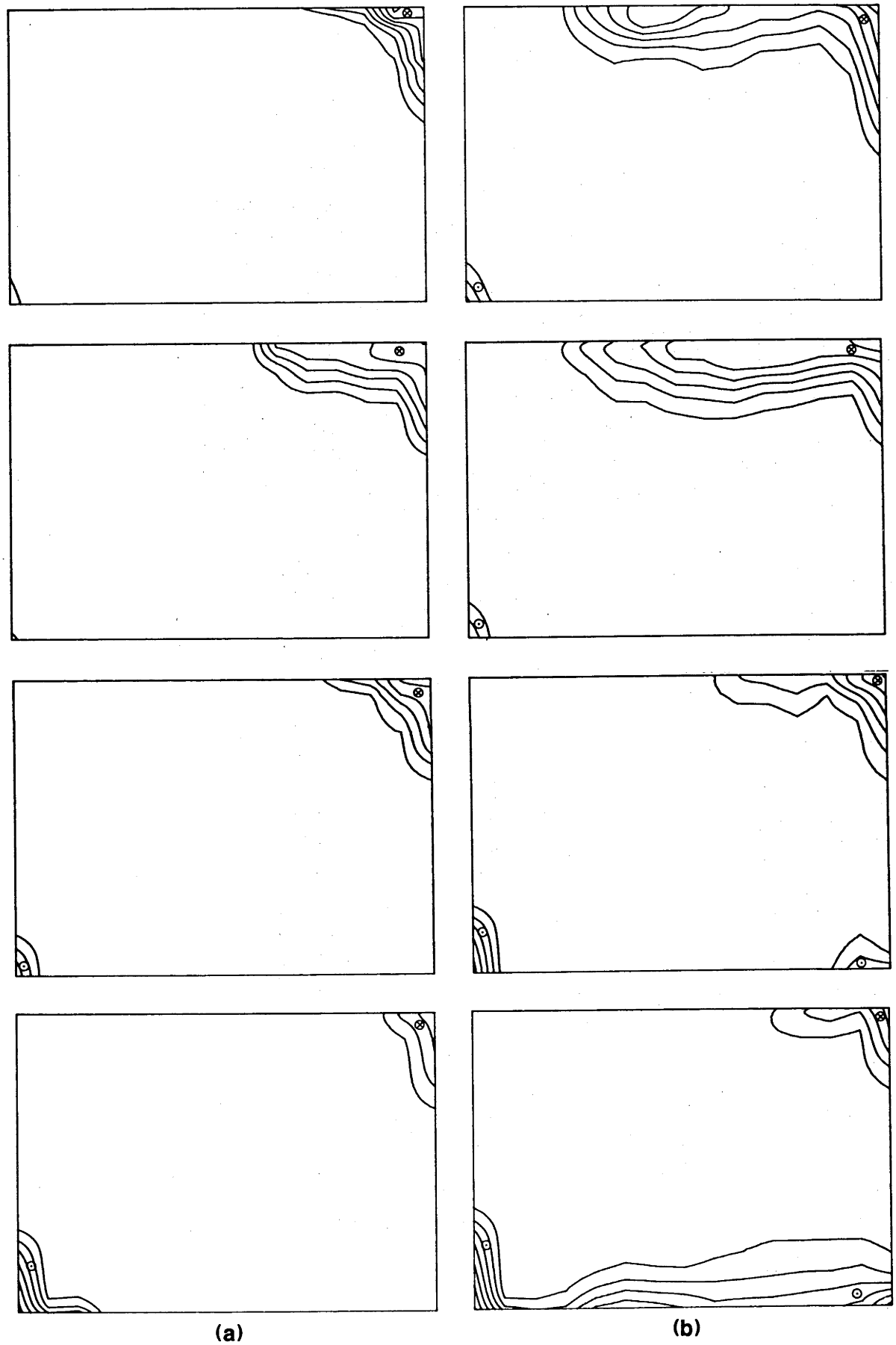

(a) (b)

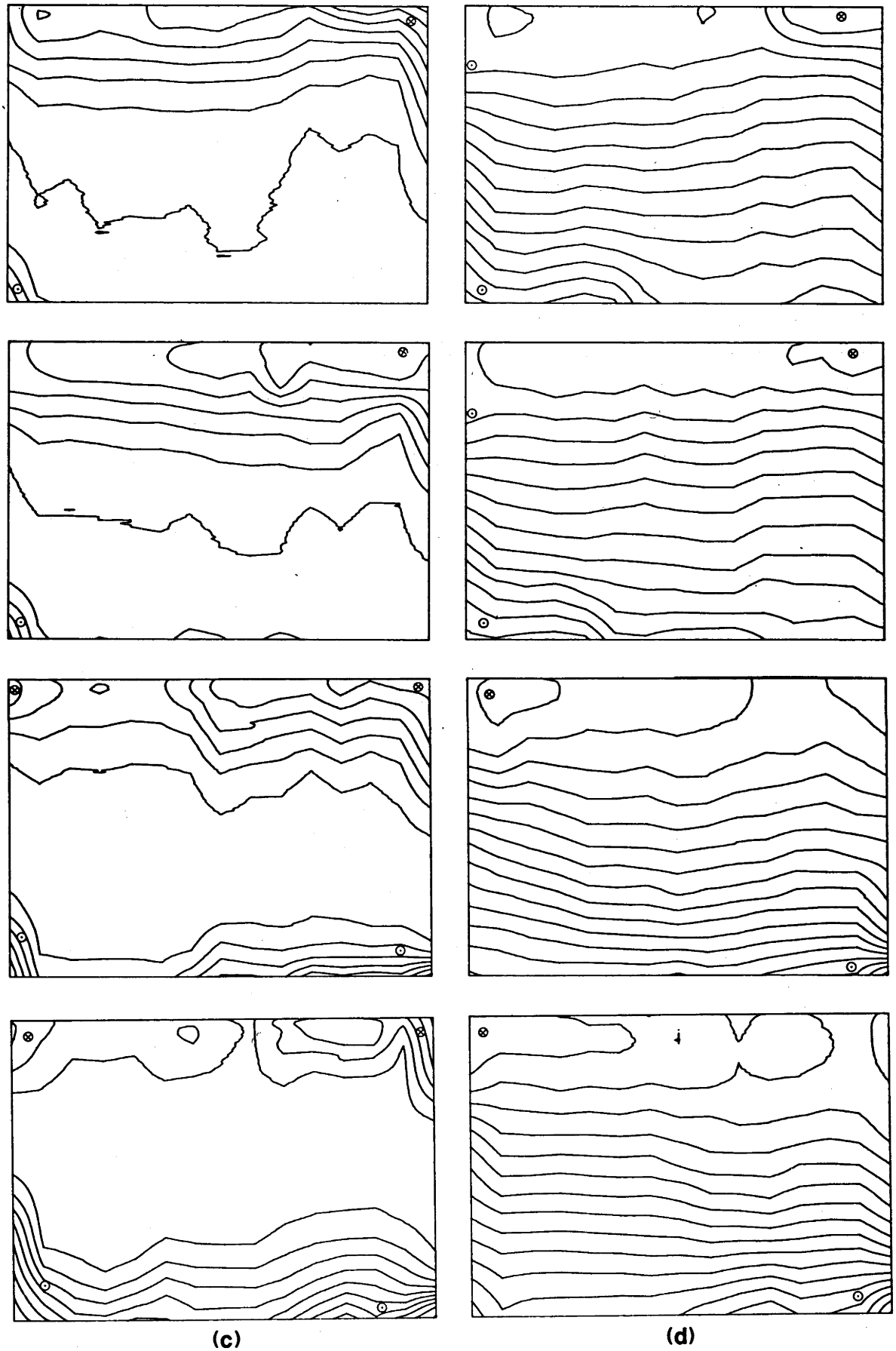

(c) (d)

The second profile in this column indicates that the warm current was particularly wide at that section, reflecting the presence of a large amplitude wave or eddy.

The dimensions of the warm current were generally larger than those of the cold bottom current. This resulted from the higher buoyancy flux associated with the warm flow, due to the non-linear equation of state of water. Specifically; the buoyancy flux B_f can be defined as the product of the reduced gravity and the volume flux out of the thermal boundary layer. Assuming that the volume flux is not effected by rotation, it can be shown to scale as $B\kappa Ra^{1/4}$ (Patterson and Imberger 1980). Hence,

$$B_f \sim g'B\kappa Ra^{1/4} = (B\nu\kappa^2/H^3)Ra^{5/4},$$

indicating that the buoyancy flux is proportional to $\alpha^{5/4}$. For the flow in Figure 5.1, the coefficient of thermal expansion at the temperature of the hot end wall was double that at the cold end. The buoyancy fluxes therefore differed by a factor of 2.4. This effect is also demonstrated by the stronger temperature gradients within the cold current in Figure 5.1. Clearly the difference in the buoyancy fluxes is very significant at high Rayleigh numbers and will be seen to play an important role in the steady state flow discussed in Chapter 6.

After 100 periods (Column (b) of Figure 5.1) the growth and interactions of eddy structures had significantly broadened the currents. This is also evident from the photographs of the intrusion in Figure 4.1. It was pointed out in the previous chapter that at the higher rotation rates ($Ek < 5x10^{-5}$) the nose of the current almost stagnated before reaching the end of the cavity, indicating that the cross cavity flux exceeded the alongshore flux. The dynamics of the cross flow was of particular interest, since this appeared to influence the flow throughout the cavity. While eddies were extremely prominent in the region, the mean cross stream velocities were essentially constant (Figure 4.7), suggesting an advective transport process, rather than turbulent diffusion. This aspect will be discussed further in chapter six.

By 200 rotation periods (column (c) of Figure 5.1) the cross cavity flow had considerably altered the nature of the flow field. When the cross-flow impinged near the centre of the opposite side wall, it produced two inertial jets along this boundary. The weaker jet went to the left and returned a small amount of warm fluid to the hot end. The stronger jet carried the remainder of the warm fluid to the right towards the cold end wall (this feature is quite distinct in the last two profiles in column (c)). This region of the flow may be analogous to that analysed by Whitehead (1985), in which a baroclinic jet impinged on a wall in a rotating fluid. In the present experiment, the cross cavity flow struck the wall almost normally and active mixing by mesoscale eddies suggests that the potential vorticity distribution would have been relatively uniform. For a constant potential vorticity jet normal to the wall, Whitehead's model indicates that approximately 70% of the fluid goes to the right and 30% to the left. This result is consistent with qualitative observations of dye transports in the cavity, even though the turbulent nature of the cross-cavity flow and associated non-linear effects complicate the exact description of the flow in our experiments.

As stratification in the cavity developed towards the steady state profiles (column (d) of Figure 5.1), the horizontal density gradients were reduced. This process acted to weaken the buoyancy driven components of the flow. Dye streaks showed that the larger scales of motion became more barotropic, while the inertial jets became more significant. The weakening of baroclinic components of the flow was accompanied by a decay in the cold flux from the base of the left side (viewed from the hot end) of the cold end wall. A somewhat surprising observation was that the flow from the right hand side of the cold end, thereafter, carried all of the cold fluid. This cold intrusion moved towards the centre of the cavity (with the side wall to its left when looking in the direction of flow), then meandered across to the opposite boundary (the left hand side wall when viewed from the hot end). After the cold water reached the left hand wall, most of it continued on to the hot end beneath the weak inertial warm jet flowing in the same direction. The steady state flow was clearly complex and Chapter 6 is devoted to a detailed description of the dynamics of this aspect of the experiment.

5.2 Development of the Stratification

The aim of this part of the study was to determine the timescales for development of the density structure in the cavity and investigate its dependence on the Ekman, Froude and Rayleigh numbers. A scaled estimate for this quantity in a non-rotating cavity was derived by Patterson and Imberger (1980) based on a simple 'filling box' process in which the interior region was assumed to fill with heated fluid by horizontal layering. This process has been studied experimentally in a cavity with only one differentially heated end wall (Worster and Leitch 1985). Such a configuration more closely models the idealized filling box, because of the absence of a sink for the buoyant fluid. However, experiments by Yewell, et al. (1982) and Ivey and Hamblin (1988), along with temperature sections such as those in Figure 5.1, suggest that a similar type of process may operate in cavities with two differentially heated end walls. Patterson and Imberger (1980) derived the timescale to pump all the fluid in the cavity through the thermal boundary layers. This result is given by equation (2.4) and is repeated here for convenience,

$$\tau \sim \frac{HL}{\kappa Ra^{1/4}}. \tag{5.1}$$

This quantity will be referred to as the 'heat-up' time.

Cross-sectional profiles, such as those in Figure 5.1, were used to determine the adjustment timescales. Ten profiles, recorded after the system had been allowed to reach steady state, were averaged to determine the mean steady state temperature structure. The standard deviation of the instantaneous temperature values from the steady state values was then calculated for each cross-sectional profile taken during the heat-up process. More precisely, if the two dimensional matrix of temperature values for a given time and cross-section has elements T_{ij} and the steady state values at the same positions are S_{ij}, then the standard deviation between the profiles is defined as

$$\delta T = \left(\frac{\sum_{i=1}^{n} \sum_{j=1}^{m} | T_{ij} - S_{ij} |^2}{nm} \right)^{1/2}, \tag{5.2}$$

where n was the number of thermistors (n = 15) and m was the number of readings taken by each thermistor in a single profile ($m \approx 100$). δT was calculated at the four cross-sections in the tank throughout the development of the flow. This procedure was carried out over the entire experimental parameter range.

Values of δT, normalized by the end wall temperature difference ΔT, are plotted as a function of time (non-dimensionalized by the heat-up time) for a range of Ekman and Froude numbers in Figure 5.2 and for two Rayleigh numbers in Figure 5.3. Although there is not a simple exponential behaviour, the data for any given run can be fitted satisfactorily by two exponential curves, corresponding to the early and later development of the stratification. In other words, the adjustment process can be divided into two regimes, each of which is described by an exponential timescale. Attempts to fit the data to a power-law yielded unsatisfactory results. The trends for small times ($t < 0.5\tau$) will be discussed first.

The initial adjustment is well described by the exponential law,

$$\delta T = C \, \Delta T \, e^{-kt/\tau}, \qquad (5.3)$$

where C and k are constants. Figure 5.2 indicates that the timescales are independent of rotation rate, while Figure 5.3 shows that the non-dimensionalization accurately describes the dependence on the end wall forcing for the range of ΔT investigated. There is also no distinguishable dependence of any of the data on the position along the tank. Measurements of the slopes and intercepts in Figures 5.2 and 5.3 give $k = 1.23 \pm 0.17$ and $C = 0.15 \pm 0.01$ for the early development of the temperature structure. This value of k corresponds to a timescale of $(0.81 \pm 0.11)\tau$.

Since the timescale for the early development of the stratification scales with the heat-up time, it is reasonable to assume that the adjustment process is adequately approximated by the filling box model. The transition point from the filling box to a second adjustment process, as given by the intersection of fitted curves for the two regimes, occurred at $t = (0.54 \pm 0.10)\tau$. For comparison, the sections in Figure 5.1

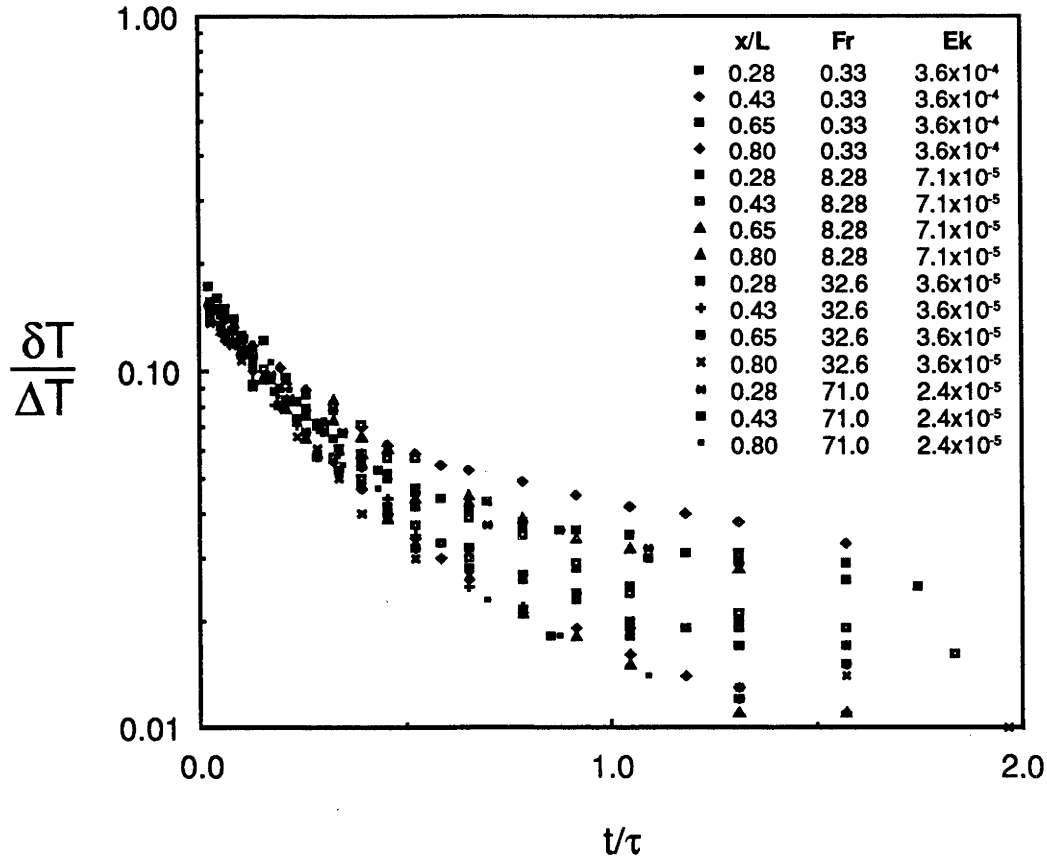

Figure 5.2 The standard deviation of the developing temperature structure from the mean steady state temperature, as a function of time (nondimensionalized by the applied temperature difference and the heat-up time respectively). Runs cover a range of Ekman numbers, Froude numbers and positions along the cavity.

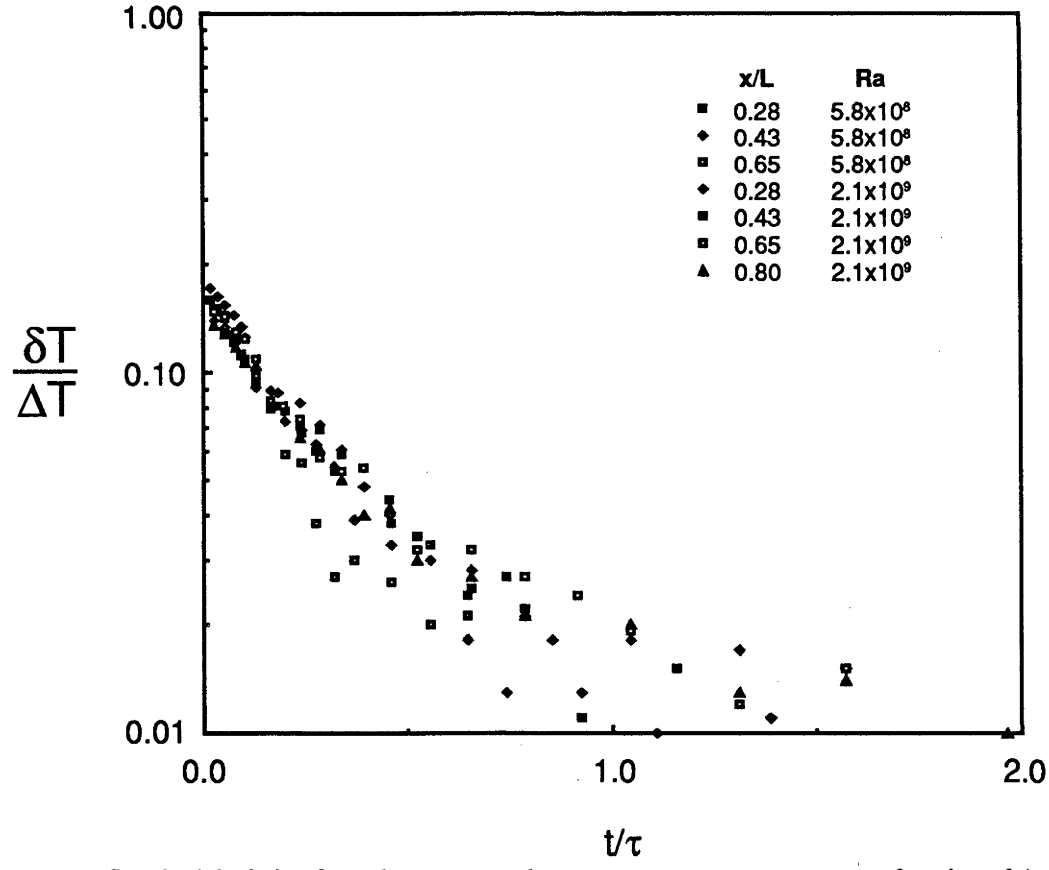

Figure 5.3 Standard deviation from the mean steady state temperature structure as a function of time, for a range of Rayleigh numbers and positions along the cavity.

correspond to (a) $t = 0.045\tau$, (b) $t = 0.090\tau$ and (c) $t = 0.18\tau$. Figure 5.4 shows the level of stratification outside the boundary currents at $t = 0.54\tau$, demonstrating that the filling box process established much of the final density structure within the cavity. The later adjustment process can therefore be regarded as a 'fine-tuning' of the density field.

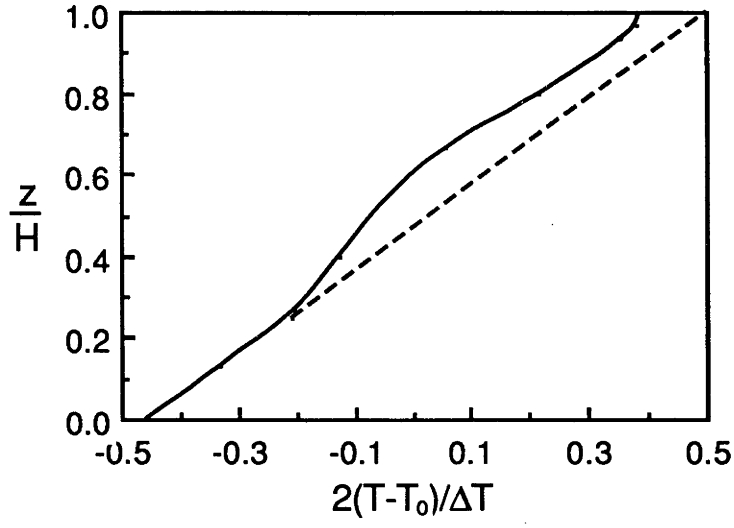

Figure 5.4 A vertical temperature profile within the cavity at the transition time between the two adjustment regimes ($t = 0.54\tau$). The broken line represents the steady state structure. With the temperature non-dimensionalized in this way, the profile is representative of the entire parameter range investigated. T_0 is the average of the two end wall temperatures.

The second adjustment regime was significantly slower than the first, but again could reasonably be described by an exponential law. The rapidity of the transition between the two regimes varied significantly, leading to a large degree of scatter in δT in the second regime. However, as noted in the previous paragraph the transition point was relatively constant. After the transition, the rate of change of δT with time continued to be independent of rotation rate. Since this result is not clear from inspection of Figure 5.2, the data have been replotted in Figure 5.5. Shown in this figure are the timescales for the second adjustment regime as a function of rotating Froude number. Taking into account the scatter in the data, there is no discernible trend, confirming that within the parameter range studied adjustment times were independent of rotation.

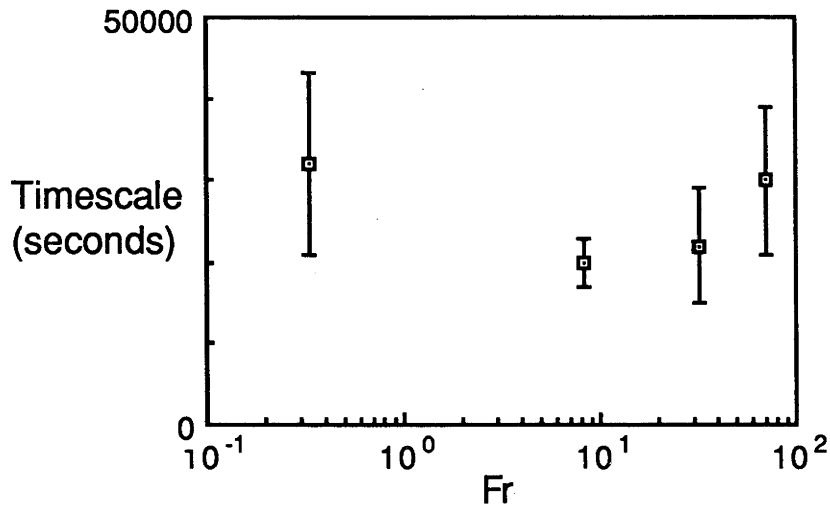

Figure 5.5 The exponential timescales for the second density adjustment process ($t > 0.5\tau$), as a function of rotating Froude number. The error bars represent one standard deviation, calculated from the values obtained at different cross-sections in the cavity. The Rayleigh number was constant for these runs at $Ra = 2.1 \times 10^9$.

The data in Figure 5.3 indicate that the second adjustment process had a relatively strong dependence on Rayleigh number. As noted by Patterson and Imberger (1980), the motion in the core region of the cavity during the approach to steady state is extremely complex, making detailed scaling of the the behaviour very difficult. However in dimensional terms, the exponential time scales were $(6.8 \pm 1.5) \times 10^4$ seconds for $Ra = 5.8 \times 10^8$ and $(2.33 \pm 0.55) \times 10^4$ seconds for $Ra = 2.1 \times 10^9$. Although the parameter range was insufficient to empirically determine the Rayleigh number dependence, these results suggest that the second stage adjustment timescales may have a close to linear dependence on Ra. This contrasts with the weaker $Ra^{1/4}$ dependence of the first regime.

A separate experiment was conducted in which the applied temperature difference, ΔT, was increased after the flow had been allowed to reach steady state. The transition was from a steady state flow with $Ra = 5.8 \times 10^8$ to a second steady state with $Ra = 2.1 \times 10^9$. This experiment yielded a single exponential timescale of 1.9×10^4 seconds for the duration of the adjustment process. This timescale agrees with the value of $(2.33 \pm 0.55) \times 10^4$ seconds, given in the previous paragraph for the second adjustment

when $Ra = 2.1x10^9$, indicating that the second, much longer, adjustment regime is relevant to the problem of modification of existing stratification by external forcing. This is perhaps not a surprising result since strong stratification was present throughout the process. Clearly, if the initial stratification had been sufficiently weak, the filling box mechanism would have operated at early times. Therefore, in summary, the initial conditions (strength of the initial stratification) determine the type of adjustment process, while the new boundary conditions determine the actual value of the adjustment timescale.

5.3 Conclusions

This completes the description of the transient flow, by considering its long term development to a steady state situation. The processes associated with the development of stratification, as well as some of the effects of a stratified environment on boundary currents have been considered. The chapter deals particularly with the heat-up timescales of the convective flow, both from an isothermal state and as a perturbation of a steady state. These processes can be described in terms of two adjustment modes. While the fluid was only weakly stratified (relative to the gradients associated with the forcing), a filling box process operated on an exponential timescale of $(0.81\pm0.11)\tau$. The second mode then took over. This was essentially a fine-tuning of the density field and the relevant timescale is dependent on the Rayleigh number. Perhaps the most significant finding is that both adjustment modes are independent of rotation.

CHAPTER 6

THE STEADY STATE FLOW

A very brief description of the steady state mean flow was given in Chapter 5, as part of the discussion of the transient behaviour. In this chapter, a detailed account of the steady state flow is presented. We begin Section 6.1 with a qualitative description of the mean flow, followed by a discussion of the potential vorticity dynamics of the mean flow and the role of baroclinic Rossby waves. Sections 6.2 and 6.3 then examine the temperature structure, the potential vorticity field and the variability in temperature associated with the eddy field. Since potential vorticity is a dynamically important property as well as a conservative tracer for the flow, its usefulness in revealing the geometry and dynamics of the laboratory flow is investigated. The convective heat transfer is then considered in Section 6.4.

6.1 Investigation of the Mean Flow

The photographs in Figures 6.1(a) and 6.1(b) show the steady state dyed flow which originated from the hot and cold end walls respectively, when the Froude number was large and the Ekman number small. Eddies were prominent features under these conditions; however in this section we will concentrate on the mean flow in the cavity. After emerging from the thermal boundary layer, heated fluid traveled with the boundary on its right, as might be expected for anti-clockwise rotation. This boundary current became very weak in the second half of the cavity, with most of the warm fluid transported laterally across the central region of the tank in a diffuse cloud. When the warm flow reached the opposite side wall it broke into two narrow boundary jets, one of which returned to the hot end, while the other progressed towards the cold end wall. The

---

Figure 6.1 A plan view of the flow originating from (a) the hot and (b) the cold end of the cavity when $Ra = 2.2 \times 10^9$, $Ek = 2.4 \times 10^{-5}$ and $Fr = 71$ ($\Delta T = 24^\circ C$ and $f = 1.5$). The number of rotation periods since dye began to be introduced is displayed at the bottom of the figure. The tank rotation is anti-clockwise.

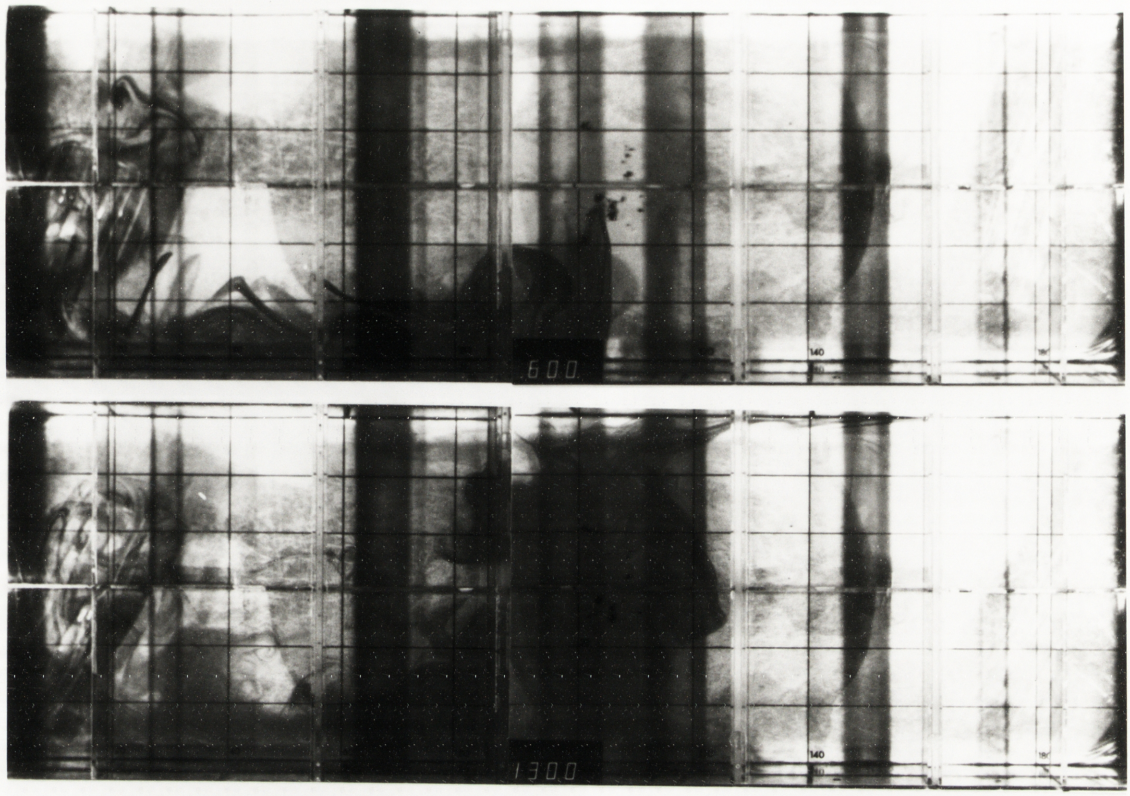

(a)

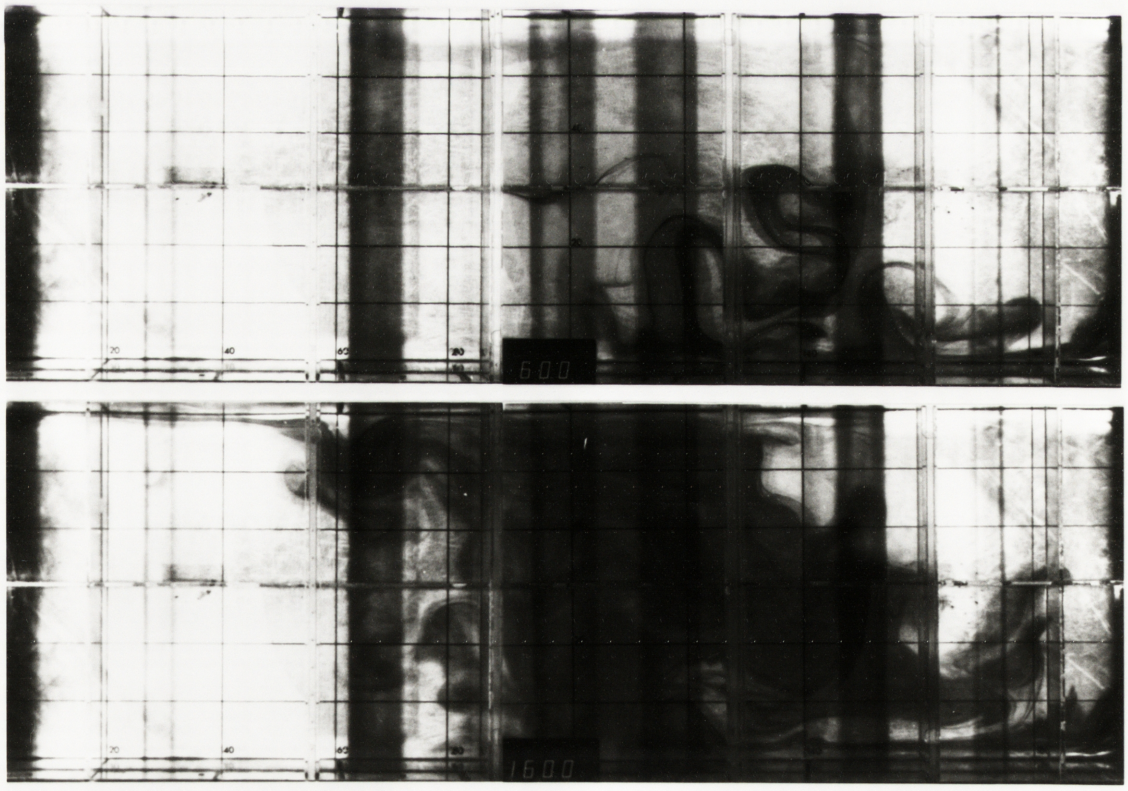

(b)

latter was the stronger of the two jets and carried fluid in an anticyclonic motion around the perimeter of the cooled end of the tank.

As the warm fluid traveled along the cold end wall, it cooled and sank. On reaching the right-hand (still looking from the hot to the cold end) side boundary it (surprisingly) formed a boundary current along the bottom of the wall (Figure 6.1(b)). After progressing approximately half way along the right-hand wall, this cold current meandered across to the opposite wall and continued to the heated end wall. These observations were supported by both instantaneous cross-stream velocity profiles obtained using the thymol-blue technique (Figure 6.2) and temperature data to be presented in Section 6.2. The mean flow can therefore be described as consisting of two basin-scale gyres, as shown schematically in Figure 6.3. The same basic flow pattern was also observed when the width of the cavity was reduced from B = 60cm to B = 15cm (by inserting an insulated divider along the length of the cavity).

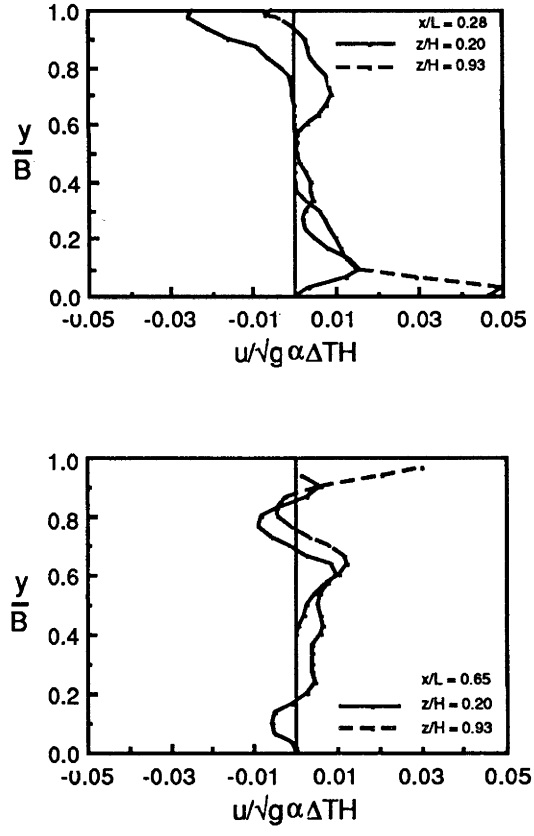

Figure 6.2 Cross-stream velocity profiles recorded at two depths (z is measured from the bottom) and two positions along the cavities length (x is measured from the heated end wall) when $Ra = 8.7 \times 10^8$, $Ek = 4.5 \times 10^{-5}$ and Fr = 65. The velocity is non-dimensionalized by the forcing term $\sqrt{(g\alpha\Delta TH)}$.

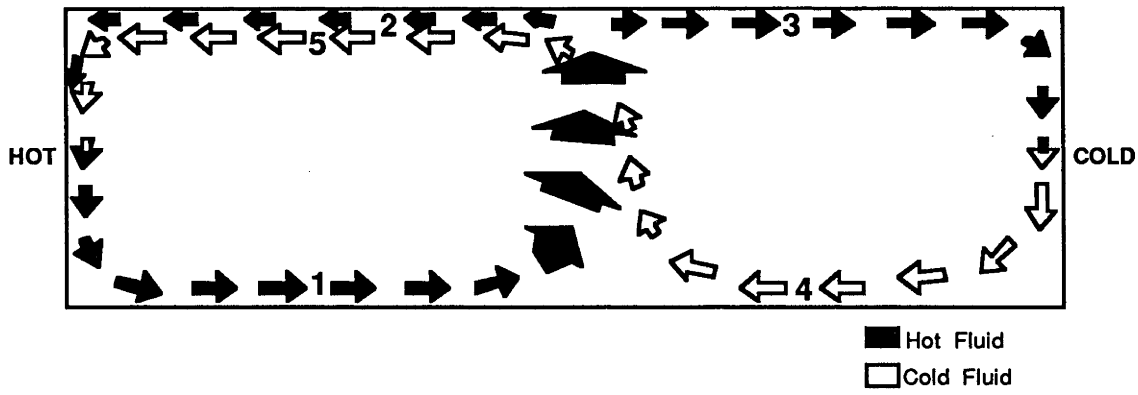

Figure 6.3 A pictorial representation of the mean flow observed in the cavity when Ek < 10^{-4}. The main boundary currents are numbered for later reference.

The formation of the two large scale gyres was an unexpected feature of the mean flow pattern. Kelvin wave dynamics on an f-plane suggest that a single cyclonic gyre should develop, with warm and cold boundary currents on either side of the cavity. The warm current flowing toward the cooled end wall (current 3 in Figure 6.3) and the cold bottom current flowing away from that end (current 4) are both contrary to the direction of propagation of Kelvin waves. The asymmetry between the warm and cold flows suggested that the driving mechanism for the gyres may have been related to non-linearity in the equation of state of water. Since the coefficient of thermal expansion α increases with temperature, the buoyancy flux which originated from the heated end was larger (by a factor of approximately two for Ra = $2x10^9$) than that from the cooled end, while the heat fluxes were equal. This difference led to a significantly stronger warm current at high Rayleigh numbers. This may explain the return flow of warm fluid (current 2 in Figure 6.3) to the heated end wall. Since all the heated fluid could not be pumped through the cold thermal boundary layer, a build up of warm fluid may have reduced the alongshore pressure gradient sufficiently to allow the return flow. This mechanism does not, however, account for the anticyclonic gyre observed.

A second cause of the observed asymmetry could be centrifugal effects, which imposed a paraboloidal shape on the isotherms. If we neglect the cross-stream parabolic variation and other distortions associated with the flow itself, then the isotherms form parabolas described by $\eta - \eta_0 = f^2(x - L/2)^2/8g$, where η_0 is the height of the isotherm at

the axis of rotation. The slope of isopotentials relative to the top and bottom of the tank is therefore

$$\frac{\partial \eta}{\partial x} = \frac{f^2(x - L/2)}{4g}. \qquad (6.1)$$

This could have affected the flow in the manner illustrated schematically in Figure 6.4. Fluid originating from the heated end and traveling between isopycnal surfaces close to the lid tends to be stretched in the vertical. Conservation of potential vorticity (defined in equation 6.11) then requires production of cyclonic relative vorticity. After this fluid passes the centre of rotation it is compressed, with a corresponding production of anticyclonic vorticity. Rather than continue along the right hand wall, the warm water follows the path of least vorticity stretching, which takes it across the centre of the cavity. On reaching the opposite boundary it then breaks into two inertial jets (currents 2 and 3 in Figure 6.3). A similar cycle, involving vertical compression followed by stretching of fluid near the base of the cavity, may account for the path of the cold water.

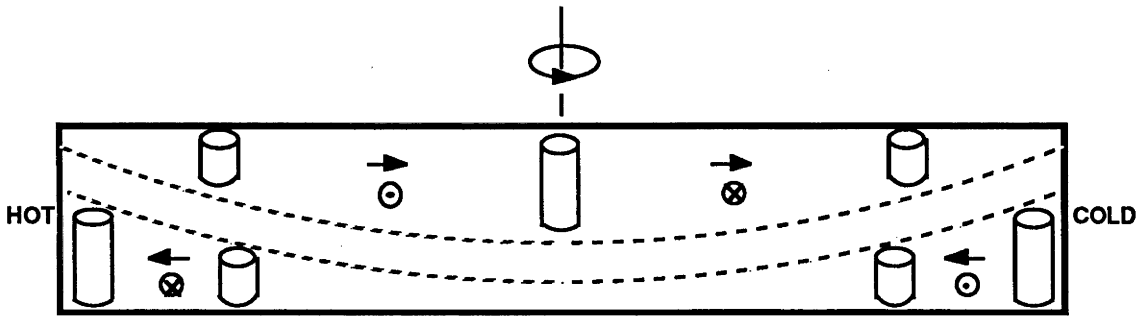

Figure 6.4 Schematic representation of the effects of parabolic shaped isopotentials on fluid columns. Arrows represent the direction of flow parallel with the page, while ⊙ and ⊗ indicate the direction of propagation of topographic Rossby waves.

The ideas outlined in the previous paragraph were verified experimentally as follows. Equation (6.1) indicates that the position along the cavity where the bottom and lid of the cavity were tangent to the potential surfaces (generally $x/L = 0.5$) could be translated by elevating one end of the cavity. Accordingly, the heated end wall of the cavity was elevated by 3cm. Under these conditions the cyclonic gyre then covered approximately one fifth of the cavity ($0 < x/L < 0.2$) and the anticyclonic gyre expanded over the remaining area ($0.2 < x/L < 1.0$). The value of $x/L = 0.2$

corresponds to the position where the tangent (of slope 3/200) touches the parabola (equation 6.1). Similarly, when the cooled end was elevated, the cyclonic gyre filled the majority of the cavity and the anticyclonic gyre the remainder. Taking this a step further, it was found that provided the slope was greater than $f^2L/8g$, the cavity filled with a cyclonic gyre when the cooled end was elevated and an anticyclonic gyre when the heated end was elevated.

Further evidence of these effects was found during experiments in which a conducting plate was inserted near the centre of the cavity. Fluid on one side of the barrier was stirred to maintain a uniform temperature, while the flow on the other side was observed. As well as increasing the aspect ratio, this also offset the centre of the flow from the centre of rotation. When the cooled end wall was near the centre of rotation, a single cyclonic gyre filled the cavity and when the heated end wall was near the centre, an anticyclonic gyre filled the cavity. All of these observations confirm that the mean flow was to a large extent controlled by the slope of the potential surfaces relative to the bottom and lid of the cavity.

The relative slope of potential surfaces and horizontal boundaries may also support topographic Rossby waves (see Pedlosky 1979, pp378-386 for a discussion of topographic waves in stratified fluids). Since there are no variations in the total fluid depth, barotropic Rossby waves are excluded. However, trapped baroclinic Rossby waves may propagate near the top and bottom of the cavity. The direction of phase propagation is with the 'shallow' fluid on the right (anti-clockwise rotation) as indicated in Figure 6.4. Neglecting the curvature (but not the slope) of the isopotentials, the dispersion relation for these waves is given by,

$$\sigma \sim -\frac{\partial \eta}{\partial x}\frac{Bf}{HFr^{1/2}}\sin\varphi \qquad (6.2)$$

(Rhines 1970) where φ is the horizontal angle of the wave vector to the x axis. The wave amplitude decays exponentially away from both the upper and lower boundary with an e-folding depth of

$$d = HFr^{1/2}/BK \qquad (6.3)$$

(Rhines 1970), where K is the wavenumber. Clearly, baroclinic waves can only propagate when this depth is less than the fluid depth or $K > Fr^{1/2}/B$.

There are two additional factors which restrict the Rossby wave spectrum. The first is the finite length and width of the cavity, which excludes modes with wavelengths greater than L/2. The second is dissipation, which strongly damps modes trapped within the Ekman layers (of depth $\sim HEk^{1/2}$). If we include these factors, Rossby wave behaviour in the cavity can be summarized in the following way: there are no modes with non-dimensional wavenumbers in the range

$$K < \max\{ \frac{4\pi}{L}, \frac{Fr^{1/2}}{B} \} \tag{6.4}$$

due to finite dimensions of cavity; wavenumbers in the range

$$\max\{ \frac{4\pi}{L}, \frac{Fr^{1/2}}{B} \} < K < \frac{1}{B}\left(\frac{Fr}{Ek}\right)^{1/2} \tag{6.5}$$

correspond to the trapped modes; and short waves with

$$K > \frac{1}{B}\left(\frac{Fr}{Ek}\right)^{1/2} \tag{6.6}$$

are rapidly damped out by dissipation. Relation (6.5) indicates that Rossby waves can propagate provided,

$$Ek < \min\{ \frac{Fr}{16\pi^2}\left(\frac{L}{B}\right)^2, 1 \}. \tag{6.7}$$

This condition is satisfied for the entire experimental parameter range. However the waves will only play a significant role in the dynamics of the flow if the change in depth of the isopotentials is greater than the depth over which the waves are trapped. This condition is satisfied when,

$$\frac{\partial \eta}{\partial x} > \frac{d}{L/2}. \tag{6.8}$$

This is equivalent to requiring that the horizontal scale of the flow L/2 is greater than the Rhines radius f/β where $\beta = (f/d)\partial\eta/\partial x$. From equation (6.1) $\partial\eta/\partial x \sim f^2L/8g$ and using equation (6.3), relation (6.8) becomes

$$K > 16 \frac{gH}{f^2L^2} \frac{Fr^{1/2}}{B}. \qquad (6.9)$$

Combining this with result (6.5) indicates that Rossby waves will only be important if,

$$Ek < \left(\frac{\nu^2 L^2}{16 g H^5} \right)^{2/5}. \qquad (6.10)$$

For our cavity this condition is equivalent to $Ek < 1.6 \times 10^{-4}$ ($f > 0.27$).

The arguments presented above suggest that baroclinic Rossby waves may influence the flow in the cavity during experiments with sufficiently small Ekman numbers. The waves propagate towards most of the boundary currents (1, 3, 4 and 5 in Figure 6.3) and would tend to transfer energy into these flows and intensify them. In contrast, the warm return flow (current 2) would tend to be dissipated by energy loss to the waves. However, observations of dye streaks along with potential vorticity data to be presented in Section 6.2, indicate that both of the inertial currents (2 and 3) were subsurface flows and thus may not have been affected by waves trapped near the horizontal boundaries.

6.2 The Temperature and Potential Vorticity Fields

With an understanding of the basic dynamics of the cavity flow, we can now continue with a detailed description of properties such as the temperature and potential vorticity fields. Temperature sections were recorded at approximately 20 minute intervals after the flow had been allowed to develop to a steady mean state. These data were averaged over time in order to remove the fluctuating signal due to individual eddies and thus obtain a mean temperature field. Alternatively the variability associated with eddies was determined by calculating the standard deviation of temperature from the mean, at each point in the cross-section. The temperature data were also used to determine the potential vorticity distribution, which is both a dynamically important property and a conserved tracer in the absence of dissipation at boundaries (see review by Rhines 1986). The role of potential vorticity in revealing the structure of ocean circulation is well established (Talley 1988). In this chapter it will be shown that, under certain circumstances it can be equally useful in the laboratory.

The potential vorticity q is defined as

$$q = \frac{(\underline{f}+\underline{\zeta}).\nabla\rho}{\rho}, \tag{6.11}$$

where $\underline{\zeta} = \nabla \times \underline{u}$ is the relative vorticity and ρ is a conservative fluid property, usually the fluid density. Assuming that the vertical velocities are negligible, (6.11) can be expanded to give,

$$q = \frac{\left(\frac{\partial u}{\partial z}\frac{\partial \rho}{\partial y} - \frac{\partial v}{\partial z}\frac{\partial \rho}{\partial x} + (f+\zeta)\frac{\partial \rho}{\partial z}\right)}{\rho}, \tag{6.12}$$

where $\zeta = \frac{\partial v}{\partial x} - \frac{\partial u}{\partial y}$ is the vertical component of the relative vorticity. For the experimental parameter range, the vertical stratification was sufficiently large and the vertical gradients of horizontal velocities (determined from velocity profiles such as those in Figure 6.2) sufficiently weak, that $\frac{\partial u}{\partial y}\frac{\partial \rho}{\partial z} \sim \frac{\partial v}{\partial x}\frac{\partial \rho}{\partial z} > \frac{\partial u}{\partial z}\frac{\partial \rho}{\partial y} > \frac{\partial v}{\partial z}\frac{\partial \rho}{\partial x}$. Furthermore, $\zeta/f < 10^{-1}$ even in the regions of maximum horizontal shear. Equation (6.12) can therefore be approximated by

$$q = \frac{f}{\rho}\frac{\partial \rho}{\partial z}. \tag{6.13}$$

This approximation is also used in the open ocean. Since the density stratification in the convection experiment was produced solely by temperature variations, (6.13) can be written in the form

$$q = f\alpha\frac{\partial T}{\partial z}, \tag{6.14}$$

where the coefficient of thermal expansion α is a function of temperature. Hence, calculation of the potential vorticity field required only measurements of the temperature and vertical temperature gradient. In regions where diffusion, viscous dissipation and forcing are all negligible, fluid elements conserve their potential vorticity and we can write $D/Dt(\alpha\partial T/\partial z) = 0$.

Figure 6.5 illustrates the flow characteristics described above at four different cross-sections in the cavity under a single set of conditions. The first column of contour plots are examples of the instantaneous temperature fields at the various cross-sections.

While the temperature gradients were non-linear, the density gradients ($\rho_0 \alpha \partial T/\partial z$) were nearly linear over most of the cross-section. Some heat loss through the cavity lid is evident; however the profiles do not extend close enough to the bottom to detect any exchange through this surface. The signature of individual eddies can sometimes be distinguished in these profiles by comparing them with the time averaged temperature profiles in the second column (Figure 6.5b). The latter were produced by averaging the temperature at each point over ten profiles, taken over a period of approximately four hours (equivalent to from 100 to 2000 rotation periods for the range of rotation speeds investigated). The results are consistent with the dye streaks in Figure 6.1 and the sketch in Figure 6.3, with the crossing of the warm flow from the right to the left hand side boundary particularly well defined by the cross-cavity slopes of the isotherms. Efficient lateral mixing by eddy motions ensured that the slope of isotherms was generally small in regions away from the strong boundary currents.

Column (c) in Figure 6.5 shows the potential vorticity fields calculated by applying equation (6.14), with local values of α, to the temporally averaged temperature values. This is undoubtedly the most revealing form in which to present the temperature data. It defines the strong currents (regions of high potential vorticity) flowing away from the heated and cooled end walls much more clearly than does the raw temperature field. Furthermore, the conservation of potential vorticity (except for dissipation at boundaries and creation at the end walls) allows mean fluid paths to be followed from one profile to the next. In Figure 6.5 some of the regions of equal potential vorticity are

---

Figure 6.5 Profiles of various flow characteristics at x/L = 0.28, 0.43, 0.65 and 0.80 respectively (moving from the top to the bottom of the page) when $Ra = 2.2 \times 10^9$, $Ek = 2.4 \times 10^{-5}$ and $Fr = 71$. These conditions are the same as those in Figure 6.1. The profiles cover the cross-sections to within 0.5cm of the side and bottom boundaries and completely to the top of the cavity. Column (a) are examples of the instantaneous temperature profiles. T_0 is the average of the end wall temperatures and the isotherms are at 1.0°C intervals. Column (b) represents the temporally averaged temperature profiles, while column (c) are potential vorticity profiles. Isolines of potential vorticity are at intervals of $0.005 m^{-1}s^{-1}$ and the shading corresponds to $0.045\text{-}0.050 m^{-1}s^{-1}$ for the lighter regions and $0.060\text{-}0.065 m^{-1}s^{-1}$ for the dark regions. Column (d) illustrates contours of constant standard deviation in temperature at 0.1°C intervals.

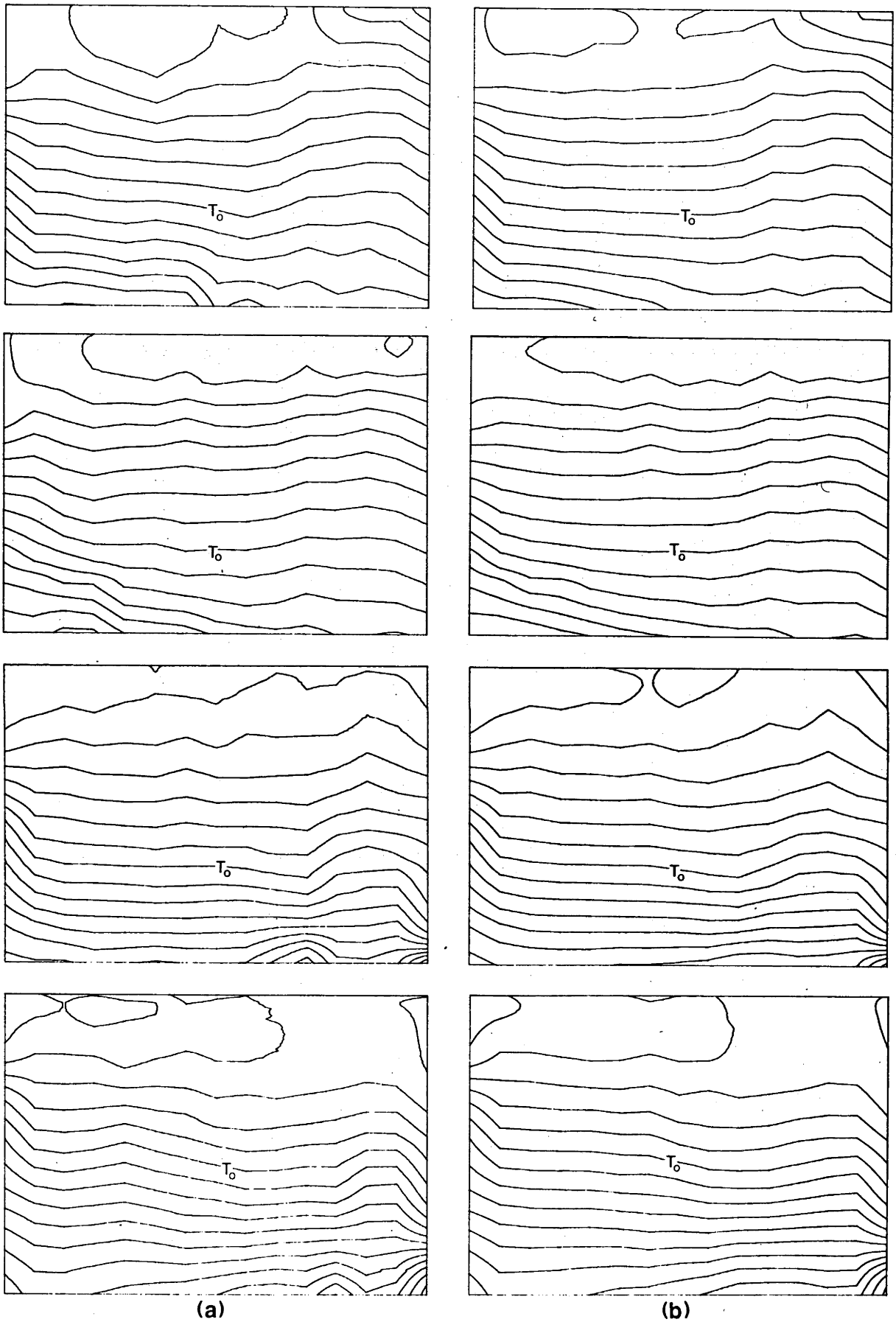
T_o
T_o
T_o
T_o
T_o
T_o
T_o
T_o
(a)
(b)

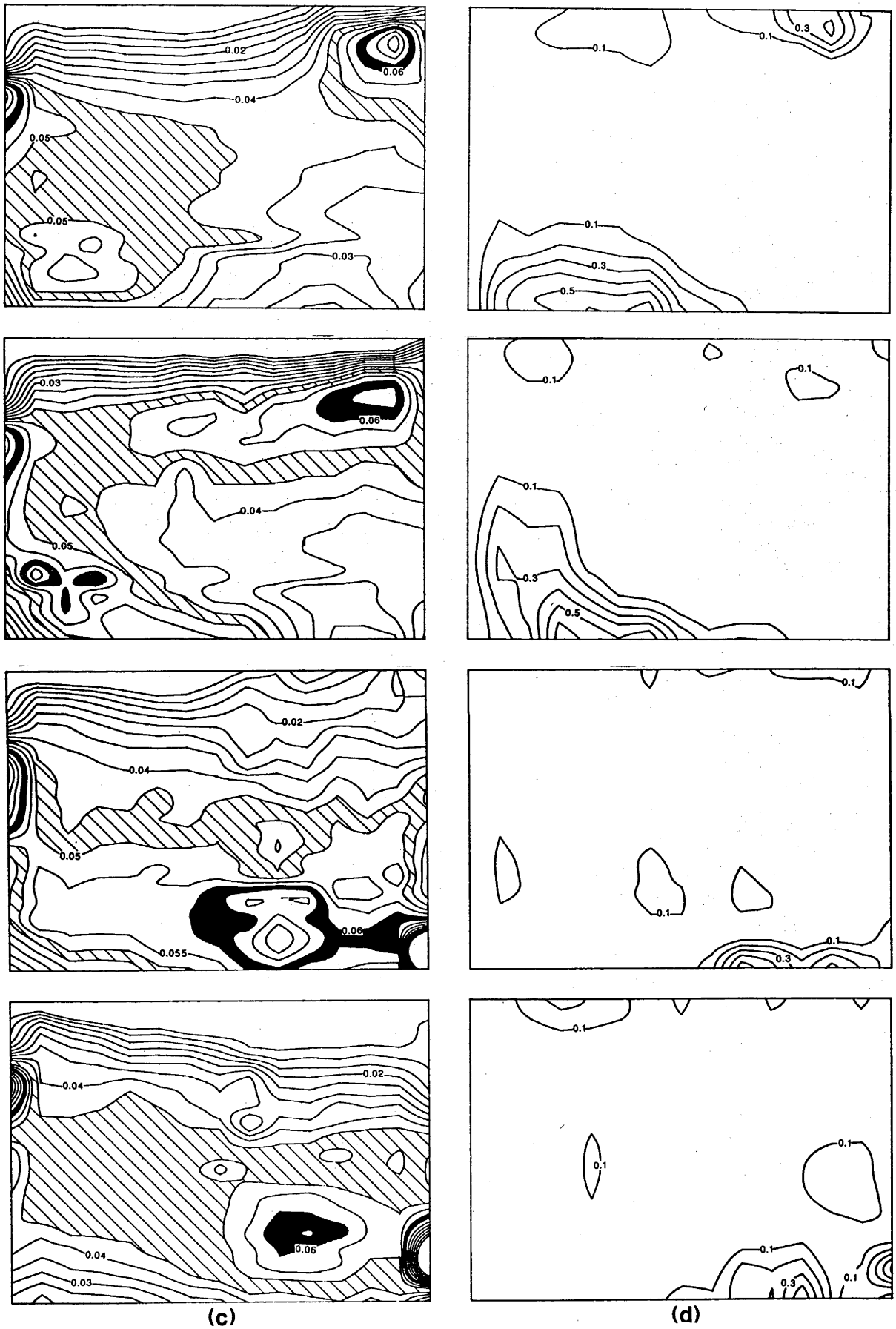
0.02
0.06
0.04
0.05
0.05
0.03
0.1
0.1
0.3
0.1
0.3
0.5
0.03
0.06
0.04
0.05
0.1
0.1
0.1
0.3
0.5
0.02
0.04
0.05
0.06
0.055
0.1
0.1
0.1
0.3
0.04
0.02
0.06
0.04
0.03
0.1
0.1
0.1
0.1
0.3
0.1

(c) (d)

shaded to allow paths to be easily traced. Broadening of the warm current (top right hand corner of the profiles, and current 1 in Figure 6.3) with distance from the hot wall is clearly marked. This region of the flow also demonstrates the horizontal diffusion of q by eddy motions, and its dissipation within the Ekman layers. In particular, the magnitude of the potential vorticity decayed with distance from the source, while the depth at which the maximum value occurred increased. Some of these aspects are even more distinct in the cold region of the flows. Working from the bottom to the top of column 6.5c, the cold current (current 4 in Figure 6.3) widened then crossed to the opposite side boundary where it progressed towards the heated end wall (as current 5). There was significant dissipation over this path, while the basic shape of the current was preserved.

Another prominent feature of all the potential vorticity profiles is a concentration of q approximately two thirds of the way up the left hand boundary (some evidence of this can also be seen in the raw temperature profiles). This feature corresponds to the two jets (2 and 3 in Figure 6.3) which carried warm fluid away from the central region of the tank, toward the two end walls as described in Section 6.1. The depth of the currents, and their strong confinement to the side boundary, suggest that they are inertial rather than driven by buoyancy. The portion of this flow which returned to the heated end wall as part of the cyclonic gyre did not appear to have a distinct counterpart in the cold flow. As discussed in Section 6.1, this asymmetry may have resulted from non-linearity in the equation of state for water and the consequent difference in buoyancy fluxes out of the two end wall regions.

The cold current near the cooled end wall (bottom right hand corner of the last two profiles in column (c)) had a particularly complex potential vorticity structure. This may have been related to the opposing influences of the linear Coriolis term in the momentum equation (pushing the current away from the side boundary) and the nonlinear potential vorticity constraints (holding the current against the boundary). The resulting current appeared to consist of two interacting components. One component was centred against the side wall and had similar characteristics to the inertial currents discussed above. The other component was centred some distance from the side wall and resembled the warm

current at the other end of the cavity. Since the potential vorticity of the latter component increased with distance from the source, there must have been significant input of fluid from the inertial component which had greater potential vorticity.

In regions away from the boundaries and strong currents, the potential vorticity gradients were generally small. This is particularly true of the first and last profiles in Figure 6.5 which correspond to the central regions of the large scale gyres. It is suggested that these cross-sections may reveal islands of nearly constant q covering the central area of the gyres. Within such islands, dissipation is small and time-mean streamlines form closed loops. Potential vorticity gradients are expelled from these regions and eddy stirring maintains a homogeneous distribution of q. The degree of homogenization depends on the relative magnitudes of the diffusive timescale and the timescale over which the stream function varies (Rhines and Young 1983). Observations in the cavity indicate that the stream function is relatively constant, suggesting that conditions may be suitable for significant homogenization.

Since both density and potential vorticity are conserved along streamlines in the absence of diffusion and dissipation, it is useful to replot the potential vorticity distribution along isotherms. Figure 6.6 shows the results for two isotherms using the same data as that used to produce Figure 6.5. The isotherms have been chosen to include most of the strong currents, while generally excluding the Ekman layers where dissipation dominates. As in the contour plots of Figure 6.5, regions of relatively strong flow and regions dominated by eddy stirring are clearly distinguishable. One clear advantage of plotting the data along density surfaces is that, if we follow the distribution of q from one section to the next, we find that conservation of potential vorticity demands that the flow field be like that depicted in Figure 6.3. In particular, with the exception of the signal associated with the inertial return flow, we find that the potential vorticity maxima swaps to the opposite side of the cavity for both isotherms near $x/L = 0.5$.

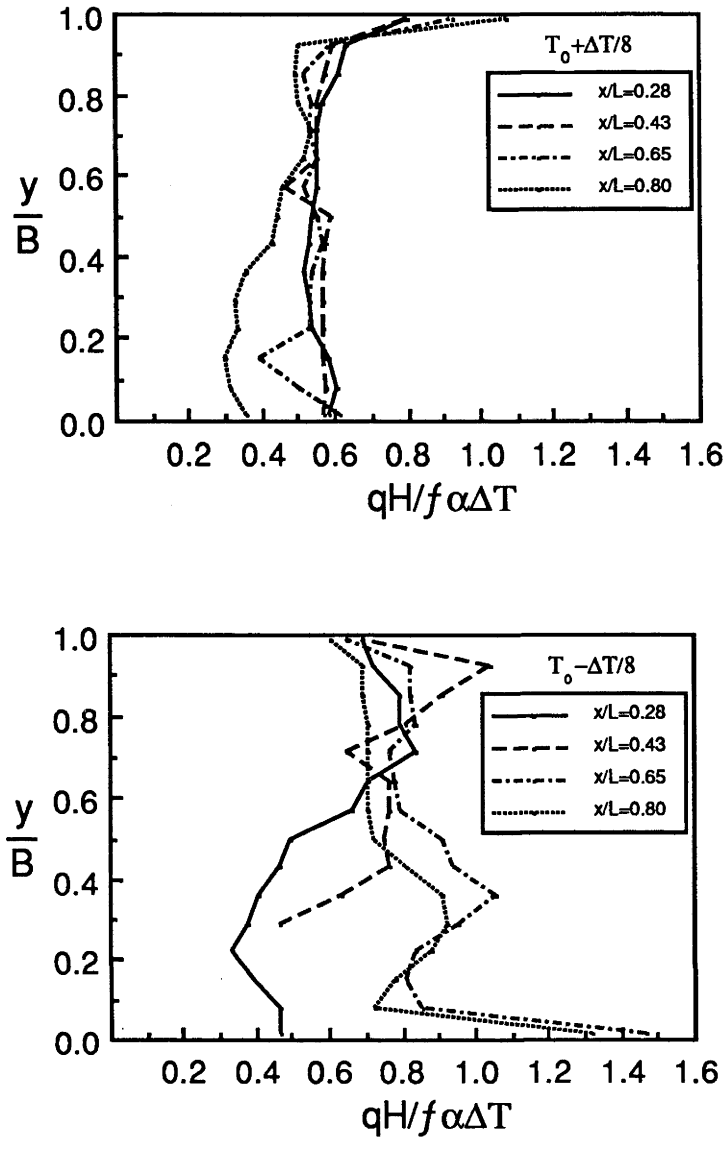

Figure 6.6 The non-dimensional potential vorticity distribution measured along the isotherms $T_0+\Delta T/8$ (top) and $T_0-\Delta T/8$ (bottom) at the the four cross-sections given in Figure 6.5. The applied conditions are also the same as those in Figure 6.5.

Column (d) in Figure 6.5 illustrates the distribution of variability (based on a 20 minute sampling period) associated with the turbulent eddy field in the cavity. Shown are contours of constant standard deviation in temperature calculated from the ten profiles. As might be expected, regions of high variability are correlated with the position of strong currents where large vertical and horizontal shears lead to instability. The maximum variability occurred near the horizontal boundaries, but probably outside the Ekman layers. The two inertial jets on the left hand wall which carried warm fluid from the centre of the cavity to the two end walls showed less variability. This result is consistent

with the dye observations which indicated that these currents were more stable. The variability associated with the cold current in the two sections closest to the cooled end, supports the earlier assertion that this part of the flow consisted of two components. The low levels of variability away from strong currents indicated that as eddies moved away from the regions of baroclinic instability, their vorticity was dissipated by Ekman layer pumping.

6.3 Ek, Fr and Ra Dependence

The general circulation of the ocean is determined by the size of the ocean basin, dissipation at boundaries, internal mixing of buoyancy and momentum, and forcing by wind and buoyancy. Analogous features (excluding surface wind stress) exist in the convection experiment and each can be represented by one of the parameters defined in Section 3.2. For example, the size of the basin is described by the Froude number, which is the ratio of the width of the cavity to the Rossby deformation radius, while the role of dissipation is determined by the Ekman number. Both of these parameters were varied by changing the rotation rate. The Rayleigh number, on the other hand, describes the strength of the forcing and is controlled experimentally by the applied temperature difference.

A single cross-section (x/L = 0.28) has been used to illustrate the dependence of the temperature, potential vorticity and variability, on the Froude and Ekman numbers (Figure 6.7). The average temperature profiles (column (a)) indicate that the vertical temperature gradients were almost independent of rotation over most of the cross-section. The cross stream temperature gradients were smaller at low Froude numbers, as would be expected for a geostrophic flow. However, even at large Froude numbers, lateral transport by eddy motions significantly reduced the slope of isotherms outside the strong current regions. Careful examination of the temperature profiles also indicated that with

---

Figure 6.7 (a) Averaged temperature (b) potential vorticity and (c) standard deviation in temperature at a single cross-section (x/L = 0.28) for a range of rotation rates. The top row corresponds to $Ek = 3.6 \times 10^{-4}$, $Fr = 0.33$, the second row to $Ek = 7.1 \times 10^{-5}$, $Fr = 8.3$, the third row to $Ek = 3.6 \times 10^{-5}$, $Fr = 33$ and the last row to $Ek = 2.4 \times 10^{-5}$ and $Fr = 71$. In all cases $Ra = 2.1 \times 10^{9}$.

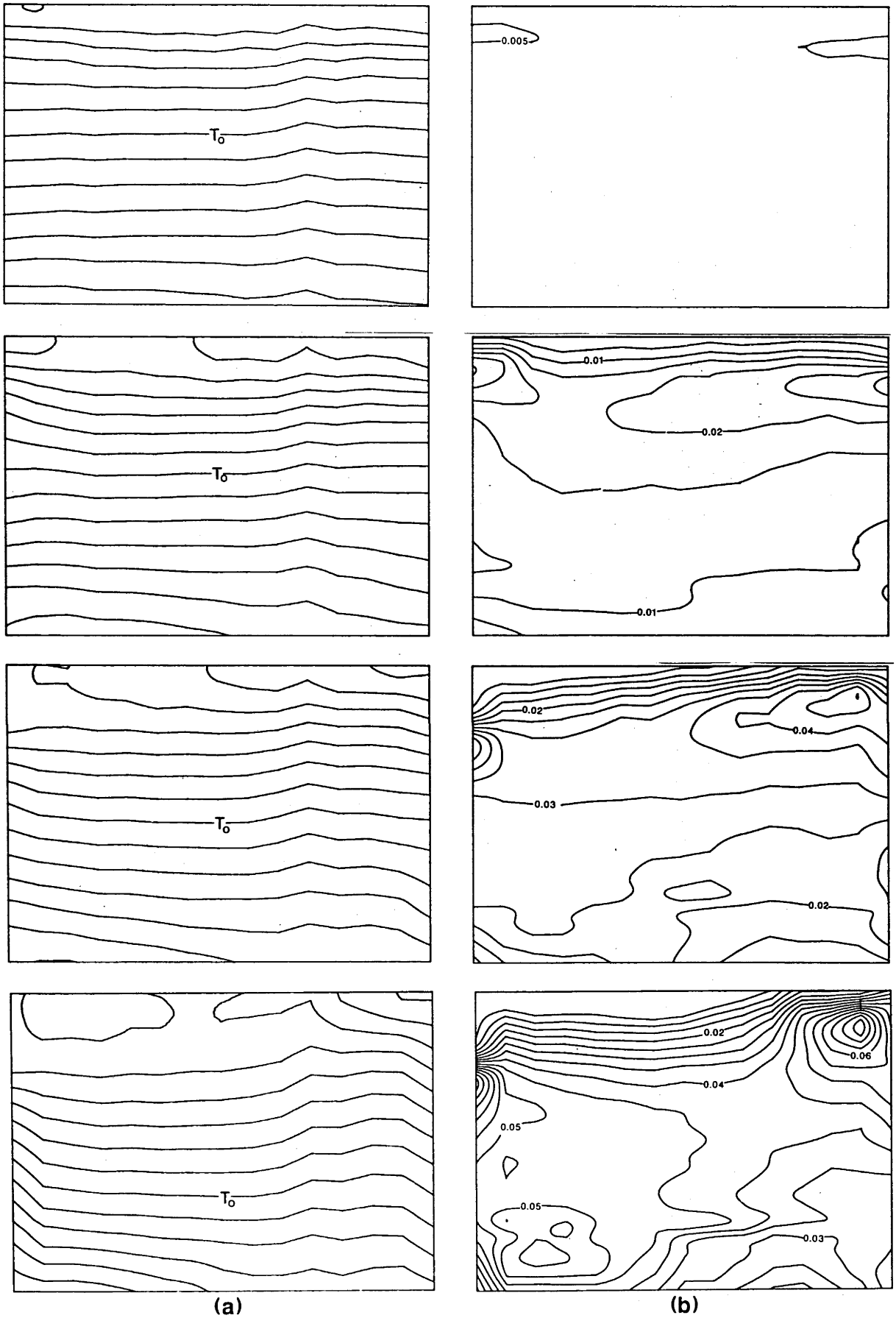
T_o
0.005
T_o
0.01
0.02
0.01
T_o
0.02
0.04
0.03
0.02
T_o
0.02
0.06
0.04
0.05
0.05
0.03

(a) (b)

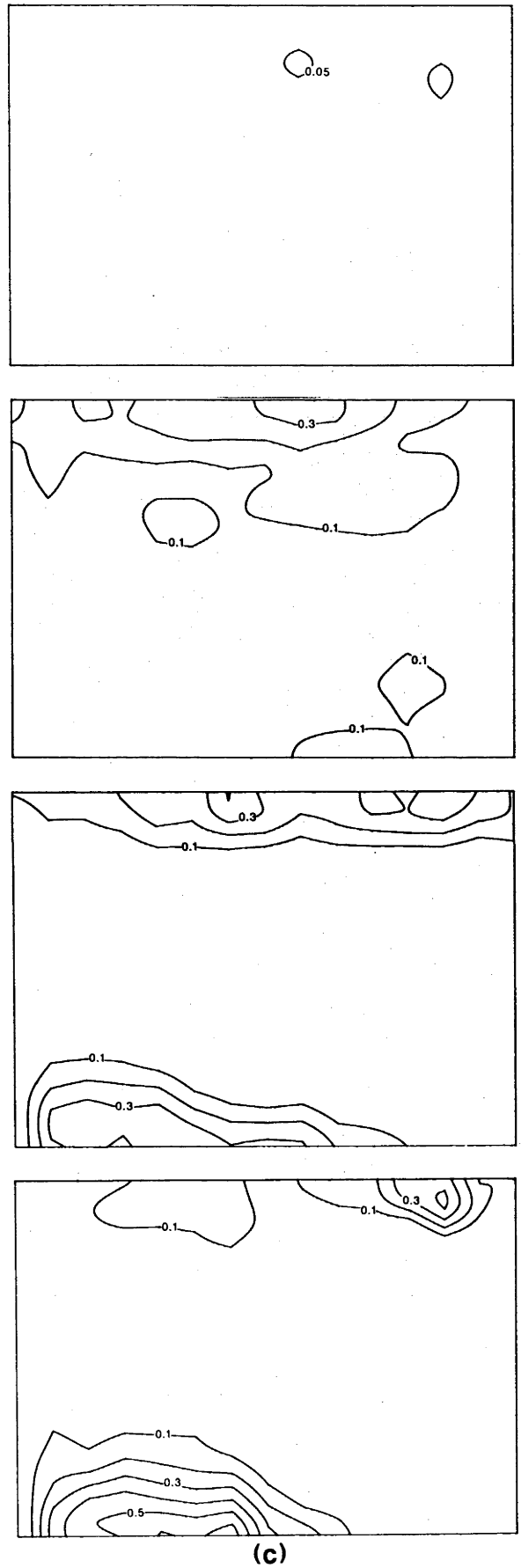

(c)

an increase in Froude number, the width of the strong boundary currents was reduced while the depth was increased.

The dimensions of the strong currents were more clearly defined by the potential vorticity fields (Figure 6.7b). These profiles also indicate that, while the total potential vorticity of the flow increased with Froude number, the basic character of the flow is preserved over the parameter range. In fact, the maximum q of the strong currents is directly proportional to the rotation rate. This result is consistent with equation (6.14), since the vertical temperature gradient was almost independent of f. Comparisons with profiles at other cross-sections (not shown) point to increased rate (per unit time) of dissipation of potential vorticity as the Ekman number is reduced. This is the result of a faster 'spin-down' through dissipation within the Ekman layers.

The standard deviation contours in Figure 6.7(c) are again correlated with regions of strong flow. Although the spatial distribution of temperature variability is Froude number dependent, the magnitude of variability generally is not. Notable exceptions to this are when $Ek > 10^{-4}$ or $Fr \lesssim 1$. In Section 4.2, it was pointed out that the condition $Ek > 10^{-4}$ is satisfied when the time scale for the growth of waves (~ 10 rotation periods) exceeds the spin-down time for fluid columns ($\tau \sim H(\frac{1}{2}\nu f)^{-1/2}$). Waves therefore failed to break and variability was small. When $Fr << 1$, shallow currents covered the entire width of the cavity and were stable. At slightly higher Froude numbers ($Fr \sim 1$) eddies formed; however the dimensions, location and interactions of eddies were strongly influenced by the side boundaries. Hence the variability associated with processes such as advection and interaction of eddies was almost absent.

The other parameter varied during the experiments was the Rayleigh number, although technical limitations restricted variation in Ra to a factor of 3.6. This was the dominant parameter in determining the stratification in the cavity. Away from the end wall boundary layers and the boundary currents, the vertical temperature gradient was relatively constant over the cavity. Measurements along the centre of the tank (y=30cm)

over the full parameter range investigated gave $\partial T/\partial z = (0.55\pm0.04)\Delta T/H$. Figure 6.8 demonstrates the Rayleigh number dependence for the same cross-section (x/L = 0.28) as that used in the previous comparisons. The potential vorticity contours indicate that the width of the strong current regions may increase slightly with Ra, consistent with the dependence of the deformation radius on $\Delta T^{1/2}$. More importantly, as the Rayleigh number is increased, larger potential vorticity gradients reflect an increase in the strength of the flow. The last column (c) shows the dependence of the standard deviation of temperature on Rayleigh number. The increase in temperature variability with Ra results from the larger horizontal temperature gradients within the flow, and to a lesser extent, the more unstable nature of the flow.

The above series of experiments demonstrated the role played by varying each of the parameters (apart from the aspect ratio and Prandtl number). The Froude number determined the length scales of the flow, with both the density and velocity fields giving length scales which varied significantly over the parameter range investigated. The Ekman number described the dissipation in the flow and therefore determined whether waves broke to form eddies. The magnitude of density gradients and flow velocities were functions of the end wall forcing and were therefore determined by the Rayleigh number.

6.4 Heat Transfer

The total heat transport by the fluid is a fundamental quantity in all studies of free convection. It is particularly important in the ocean in relation to climate studies, since the ocean is thought to be responsible for approximately half the net heat transfer between equatorial and polar regions. The experiment was accordingly designed to allow for measurement of the longitudinal heat transfer (Section 3.1).

The heat flux through the hot end wall was generally found to be a few percent higher than that through the cold end due to a small net heat loss. The heat transfer

---

Figure 6.8 (a) Averaged temperature (b) potential vorticity and (c) standard deviation in temperature at a single cross-section (x/L = 0.28) for a range of applied temperature differences. The three rows correspond to Ra = $5.8\text{x}10^8$, $8.7\text{x}10^8$ and $2.1\text{x}10^9$ respectively. In each case Ek = $4\text{x}10^{-5}$.

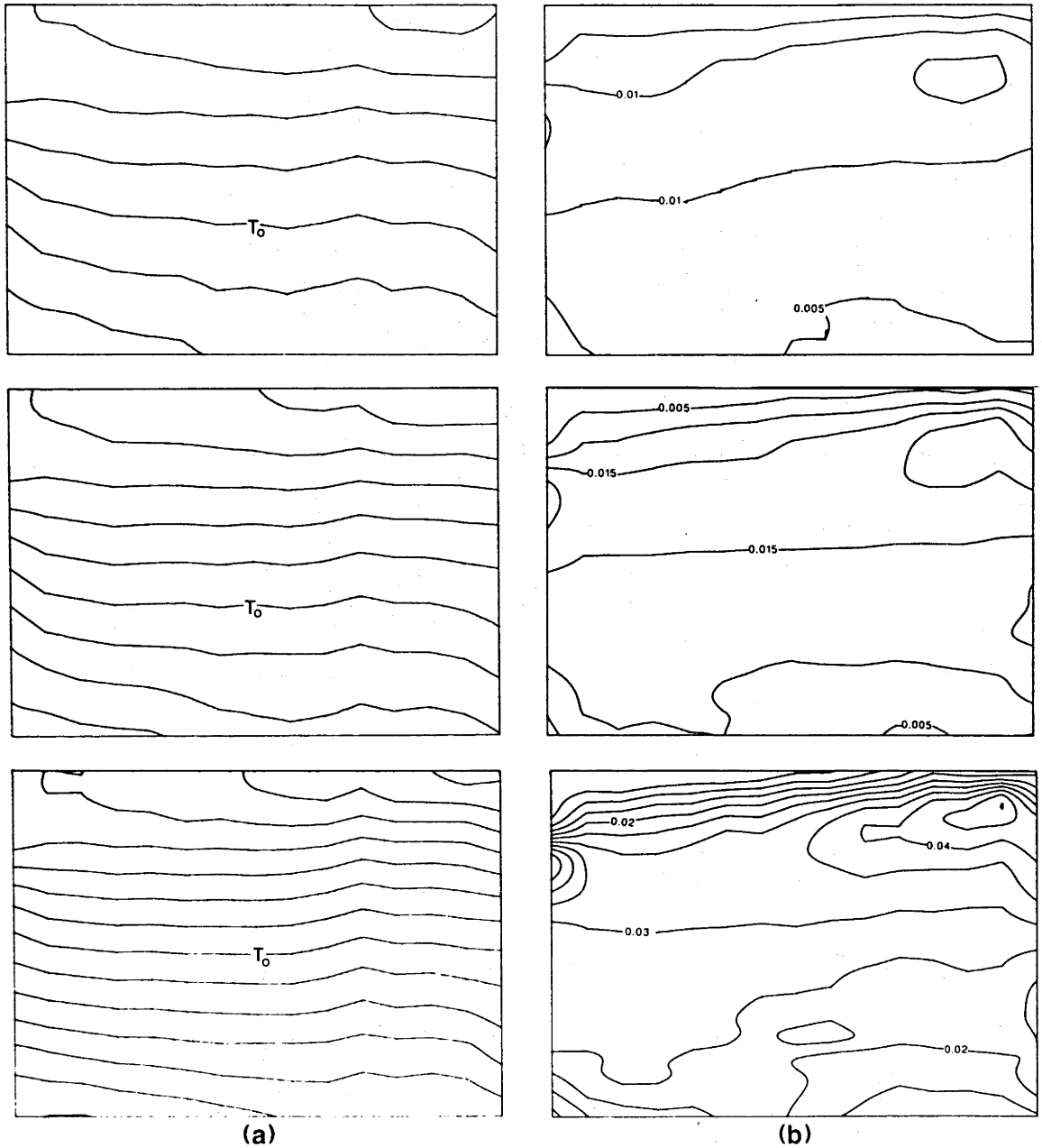
T_o
T_o
T_o
0.01
0.01
0.005
0.005
0.015
0.015
0.005
0.02
0.04
0.03
0.02
(a)
(b)

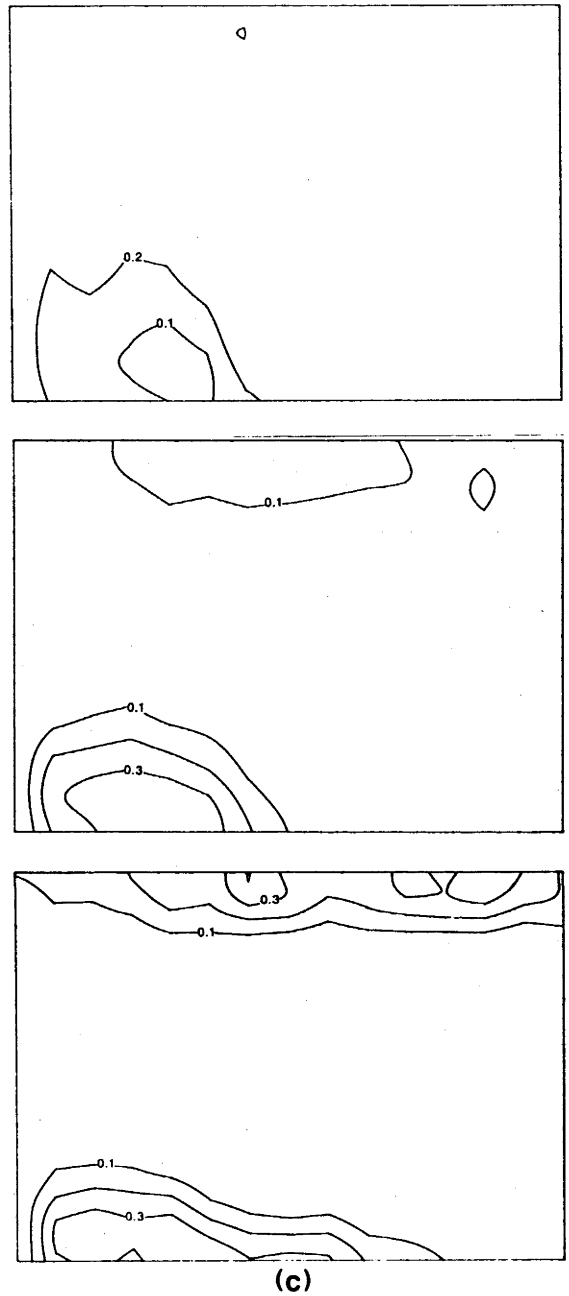

(c)

through the hot end over a range of Ekman and Rayleigh numbers is presented in Figure 6.9. It is expressed in the form of a Nusselt number (ratio of the total heat transfer to the conductive component of the heat transfer) as a function of the inverse of the Ekman number. The heat flux is found to be weakly dependent on rotation with a slight increase in Nusselt number with Ekman number (decreasing rotation rate). This may be due to the more rapid dissipation of momentum within the Ekman layers or more unstable nature of the mean flow at small Ekman numbers. Another factor which may have influenced the heat flux was the parabolic distortion of potential surfaces associated with rotation. Fluid emerging from the base of the cold end wall would need to cross isopotentials in order to reach the centre of the cavity and this would tend to impede the flow of heat and mass between the end walls. However, the important result from these measurements is that the effects of rotation on the heat transfer were secondary when compared to the Rayleigh number dependence.

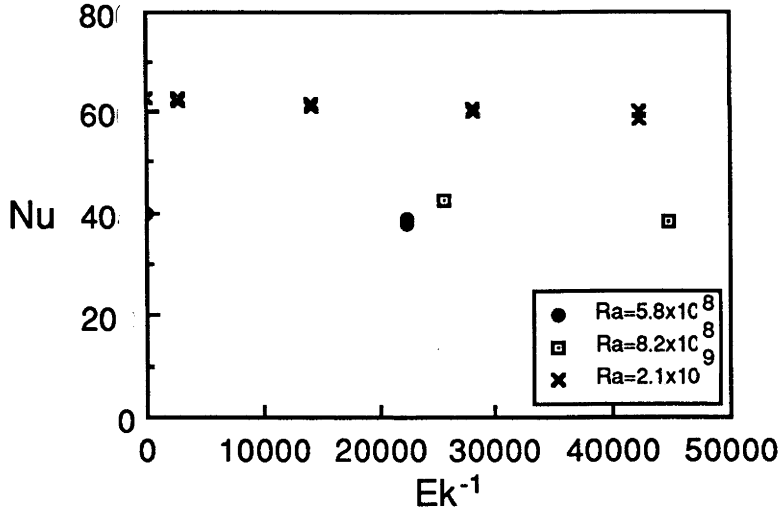

Figure 6.9 The Nusselt number as a function of inverse Ekman number for a range of Rayleigh numbers.

6.5 Conclusions

The mean flow observed in the cavity differs substantially from that expected on the basis of Kelvin wave dynamics. This has been explained largely in terms of the potential vorticity dynamics and the parabolic shape of isopotential surfaces. It has also

been suggested that Rossby waves may play a role. Possible exceptions to this are the warm inertial currents on the left hand wall (currents 2 and 3 in Figure 6.3) which were some distance below the lid and therefore may not have been significantly influenced by either Rossby wave propagation or the relative slope of the lid and potential surfaces.

The steady state experiments examined the effects of forcing, dissipation and basin size on flow characteristics such as the velocity field, stratification, variability and potential vorticity distribution. The potential vorticity is the dynamically important quantity which governs the motions and, as in the oceans (Talley 1988), has been particularly useful in revealing the structure of the mean flow in the laboratory cavity. Furthermore, the strong correlation in every detail between the flow field traced by the dye streaks and that indicated by the potential vorticity field clearly demonstrates the validity of the potential vorticity as a tracer for the flow. It is evident that the potential vorticity distribution yields much more information than the raw density data and it may play an important role in future laboratory studies on rotating stratified fluids.

CHAPTER 7

APPLICATION TO OCEANIC FLOWS

Quantitative comparisons can now be made with oceanic field data. Direct comparisons will be made between the initial intrusions in the cavity and buoyancy driven coastal currents, with special attention to the Leeuwin Current. Other aspects of the experiments have interesting implications for large scale ocean flows and these will be discussed in Section 7.2.

7.1 Coastal Currents

Density driven boundary currents in the ocean can be driven by either salinity or temperature gradients. For example, the source of the East Greenland Current is melting sea ice, while the Norwegian Coastal Current, the Alaska Coastal Current and the Nova Scotia Current are driven by river or fiord inflows. An important example of a thermally driven boundary current is the Leeuwin Current off the western and southern coasts of Australia. This flow consists of a seasonal intrusion of tropical water that moves southward along the Western Australian coast and turns at Cape Leeuwin to flow along the South coast. Thompson (1984) and Godfrey and Ridgeway (1985) showed that the current is driven into the prevailing winds, at least partially by an along-shore temperature gradient. A more recent study by Weaver and Middleton (1988) indicates that inertia may also play an important role along the west coast.

Quantitative comparisons can be made between field data from the Leeuwin Current and data from the laboratory experiments. The seasonality of the Leeuwin Current, along with its density structure (Thompson 1984) suggest an analogy with the initial intrusions observed in the cavity. Consider, for example, the hydrographic section of the Leeuwin Current at $25^0$24'S reported by Thompson (1984) and reproduced here in Figure 7.1. Like the experiments, the vertical temperature gradient showed little variation off the shelf, but was considerably more complex above the shelf. The cross-stream slope of the isopycnals over this section can be expressed as $\partial h/\partial y = 0.25f/N$ where N is

the buoyancy frequency at the shelf edge. This result is in close agreement with the experimental results in Section 4.3 which gave the constant as 0.28±0.08.

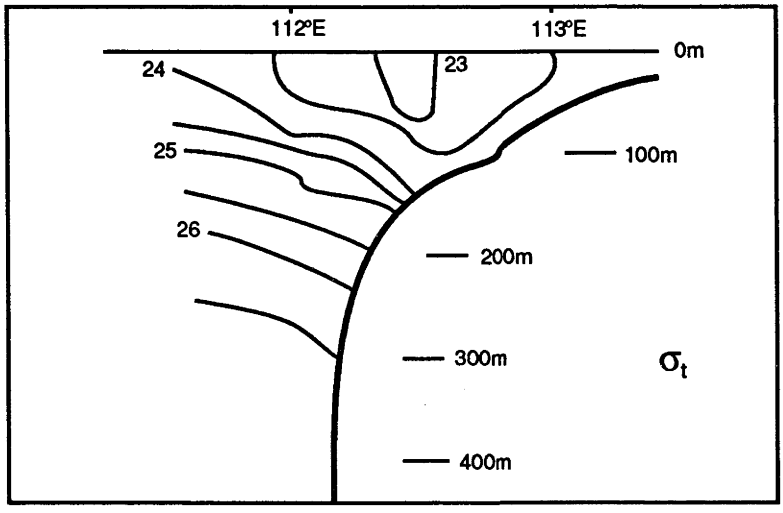

Figure 7.1 A hydrographic section along 25°24'S over the continental slope and shelf of Western Australia (reproduced from Thompson 1984). Isopycnals (σ_t) are at 1 kg m^{-3} intervals.

Griffiths and Pearce (1985b) measured the surface width of the Leeuwin Current (from the coast to the centre of the main front) from satellite imagery off Australia's South coast. The values obtained for the non-dimensional width over a three month period were b/R = 4.1±1.3, 3.8±1.0 and 4.8±1.8 for Cape Leeuwin (115°E), Albany (118°E) and Hood Point (119.5°E) respectively, where the deformation radius was based on the local surface density difference across the front and a maximum current depth of 200m. In the laboratory experiments, temperature profiles indicated that the edge of the dye cloud may be reasonably representative of the main front. When no large scale wave structures were present the dye gave a non-dimensional current width of 3.22±0.30. The tendency of the ocean current widths to be slightly higher than the laboratory values may result from the difference in the definition of the deformation radius. Alternatively it may reflect the presence of the shelf. In particular, Ou (1983) found that a shelf in a simple two layered geostrophic adjustment model marginally widened the frontal zone. A third possibility is that instabilities had already influenced the width of the Leeuwin Current. This is quite likely since the satellite images were taken more than a month after the nose of the warm seasonal intrusion had passed the observation point.

Characteristics of instabilities on buoyancy driven boundary currents have also been studied with the aid of satellite images. Non-dimensional wavelengths of $\lambda/2\pi R = 0.9$ measured on the Norwegian Coastal Current (Mork 1980) and 0.94 to 1.12 on the Nova Scotia Current (Petrie 1987) are in reasonable agreement with the experimental value of 1.19 ± 0.16. Griffiths and Pearce (1985) made measurements of the diameters of the major eddy structures and their separation (or wavelength) on the Leeuwin Current. The values of these two quantities was essentially equal during the early stages of the experiments since eddies grew until they were in contact with neighbouring eddies. They then interacted, with the dominant eddy tearing its neighbour apart (Figure 4.1). The diameter of structures off the Southern coast of Australia was reported to be $d/2\pi R = 1.19\pm0.14$ which is almost identical to the experimental value. The separation of the Leeuwin Current eddies was, however, substantially greater at $\lambda/2\pi R = 2.18\pm0.53$.

The large separation of eddies on the Leeuwin Current may result from the fact that the field data related to large amplitude eddies. Griffiths and Pearce (1985a) suggested that the wide separation was due to large meanders engulfing smaller amplitude structures and other non-linear interactions between different wavelengths. These mechanisms were first suggested by Ikeda et al. (1984), to explain an observed wavelength of $\lambda/2\pi R = 3.16$ for the California Current off Vancouver Island. Similar behaviour was observed during the experiments after ~50 rotation periods (Figure 4.1). The separation of the dominant coherent structures was then quite variable, but always larger than at earlier times.

The phase speeds of all waves observed by Griffiths and Pearce (1985a) satisfied $c/Nh < 10^{-2}$ relative to the coast with effectively zero phase speed for large scale eddies. The Leeuwin Current's depth ratio along the south coast is $H/h \approx 10$, which is considerably larger than the experimental range. However, if the trend in the theoretical curve in Figure 4.12 is relevant to the experiments, non-dimensional phase speeds of order 10^{-2} or less would indeed be expected at such large depth ratios. Despite the smaller depth ratios in the experiment, large scale eddies generally had zero phase

velocities as observed on the Leeuwin Current. More comparable depth ratios are found off Norway and Nova Scotia where non-dimensional phase speeds of 0.09 ($H/h \approx 6$) and 0.07 ($H/h \approx 3.7$) have been measured by Mork (1981) and Petrie (1987) respectively.

The time lapse between the appearance of a small amplitude wave and its breaking to form a dipolar structure, was 10 to 15 rotation periods for both the Leeuwin Current (Griffiths and Pearce 1985a) and the laboratory experiment. Growth rates are particularly difficult to measure and the only value reported by Griffiths and Pearce was for their 'structure A' which had $\varepsilon/Rf < 0.036$. The experimental value of $\varepsilon/Rf = 0.016 \pm 0.005$ is consistent with this observation. However, in a free surface laboratory experiment we might expect a higher growth rate which would be closer to the field value.

Comparisons with the Leeuwin Current indicate that the initial flow in the cavity may be relevant to flow in coastal currents. Quantitative comparisons are remarkably good when one considers that complications such as the continental shelf, external currents and wind stress are absent from the experiment (see Weaver and Middleton (1988) for a more detailed discussion of these effects).

7.2 Other Applications

The longer term development of the flow (Chapter 5) incorporated the processes associated with the production of stratification. The timescales for establishment of stratification may be relevant to a range of geophysical phenomena. Common examples are the adjustment of systems such as large lakes, seas, gulfs and oceans to seasonal variations in atmospheric temperature, evaporation rates, precipitation and fresh water run-off. While the response of the oceans to long term climatic change is a very complex problem (see for example Broeker 1987), some of the experimental results may be relevant to this problem. The fundamental result that the timescales associated with both the 'filling box' and 'fine tuning' adjustment modes are independent of rotation may be particularly useful.

We can apply the results of Chapter 5 to gain an estimate for the timescale to establish the basic stratification in the world's oceans. Consider an ocean with with a depth scale of 4km, horizontal length scale of 5000km and $\Delta\rho/\rho_0 \approx 10^{-2}$. This gives a Rayleigh number of $5\text{x}10^{22}$ and a heat-up timescale of $\tau \sim 10^4$ years (equation 5.1). The timescale to create the basic stratification is then $0.8\tau \approx 8000$ years. This rather crude estimate is in surprisingly good agreement with the value of ~ 5000 years, obtained by Colin de Verdiere (1988) using a numerical model with a more realistic heat input distribution. The simple scaling is reasonably successful because the adjustment time-scale is many orders of magnitude greater than the rotation period of the earth. Hence, local effects of rotation near the sources and sinks of buoyancy would not effect the long term development of stratification. The laboratory results also suggest that small adjustments to this basic stratification due to changes in forcing would take a period of time considerably longer than those mentioned above.

The steady state flow was explained largely in terms of the potential vorticity dynamics and the parabolic shape of isopotential surfaces. These experiments are therefore of some relevance to oceanic flows over topography on scales of a few hundred kilometres, since the effects of bottom slope are then much larger than the β-effect (Rhines 1969). Documented examples include the overflow from the Denmark Straits, the large scale mean bottom circulation of the western North Atlantic (Tucholke et al. 1973), flow over the mid-Atlantic ridge (Fu et al. 1982) and the deep flow in Drake Passage (Rattray 1985).

The dynamics of the steady flow also suggest an analogy with ocean circulation on a β-plane. While the exact dynamical equivalence between a sloping bottom with constant Coriolis parameter f and a variation in f with latitude (the β-effect) does not strictly hold for stratified flows, a useful similarity between the two systems exists for some aspects of the flow. The propagation of baroclinic Rossby waves towards most of the major currents points to an analogy with baroclinic western boundary currents in the oceans. However, it is generally accepted that western currents are inertial flows responding to the wind driven circulation, while the laboratory currents are buoyancy flows which may be

modified by Rossby waves. Therefore, the steady state currents probably have more in common with surface gravity currents, particularly those that show little seasonal variation.

It was noted in Section 6.2 that only the warm current returning towards the heated end wall of the cavity might lose energy to Rossby waves in the manner of an eastern ocean boundary current on a β-plane. However, both of the warm inertial currents on the left hand wall (currents 2 and 3 in Figure 6.3) were some distance below the lid and therefore may not have been significantly influenced by either Rossby wave propagation or the relative slope of the lid and potential surfaces. There are, however, oceanic flows which similarly impinge on a coastline and break into oppositely directed boundary jets. One example of this is the formation of boundary jets in the Alboran Sea from flow impinging on the African coast (Whitehead and Miller 1979).

The steady state experiments also encompassed a number of more general aspects of thermohaline circulation in the ocean and other large scale water bodies. For example, the effects of forcing, dissipation and basin size on flow characteristics such as the velocity field, stratification, variability and potential vorticity distribution have been examined. Such results may provide useful insights to aid the interpretation of both oceanic observations and numerical models.

CHAPTER 8

CONCLUDING REMARKS

Rotating convection currents play a major role in the circulation of the oceans and other large water bodies. A controlled and flexible experimental method for studying this class of flows has been developed. This involved supplying buoyancy to a rotating fluid by differentially heating and cooling the vertical end walls of a rectangular cavity.

When heating and cooling were initiated at the two end walls, warm and cold boundary currents formed on either side of the cavity. The currents initially propagated under an along-shore inertial-buoyancy balance and a geostrophic cross-stream balance. After 10 to 15 rotation periods rotational instabilities formed on the edge of the currents. The growth of these structures resulted in a spreading of the flow away from the boundary. For small Ekman numbers and large Froude numbers the waves produced dipolar eddy structures which coupled with the lower layer. Results indicate that this process slowed the advance of the intrusion. This flow eventually established the basic stratification in the cavity via a 'filling box' process over an exponential timescale of 0.8τ, which is independent of rotation. As the stratification developed, the relative slope of the isopotentials and the horizontal surfaces became important. The resulting steady mean circulation differed substantially from that expected on the basis of Kelvin wave dynamics. Locations of the strong currents in the cavity (as determined from dye streaks and the potential vorticity distribution) were controlled by the potential vorticity dynamics. In particular, the mean circulation consisted of two basin-scale counter-rotating gyres.

The rotating convection experiment facilitates the study of forcing, dissipation and basin size on flow characteristics such as velocities, stratification, variability and potential vorticity over a wide parameter range. This, combined with the relevance of the system to ocean circulation, suggests that the configuration (and variations upon it) will yield further useful results in the future.

REFERENCES

Ahlnas, K., Royer, T.C. and George, T.H., 1987. Multiple dipole eddies in the Alaska Coastal Current detected with Landsat thermatic mapper data. *J. Geophys. Res.*, 92: 13041-13047.

Batchelor, G.K. (1954), 'Heat transfer by free convection across a closed cavity between vertical boundaries of different temperatures', *Quart. J. Appl. Maths.*, 12, 209.

Batchelor, G.K. (1969), 'Computation of the energy spectrum in homogeneous two-dimensional turbulence', *Phys. of Fluids Supplement II* , II233-II23

Bejan, A. (1984), *'Convective Heat Transfer'*, John Wiley and Sons, New York.

Bejan, A., Al-Homoud, A.A. and J. Imberger (1981), 'Experimental study of high-Rayleigh-number convection in a horizontal cavity with different end temperatures', *J. Fluid Mech.*, 109, 283-299.

Bretherton, F.P. and J.S. Turner (1968), 'On the mixing of angular momentum in a stirred rotating fluid', *J. Fluid Mech.*, 32, 449-464.

Broeker, W.S. (1987), 'Unpleasant surprises in the greenhouse', *Nature*, 328, 123-126.

Buzyna, G., Pfeffer, R.L. and R. Kung (1984), 'Transition to geostrophic turbulence in a rotating differentially heated annulus of fluid', *J. Fluid Mech.*, 145, 377-403.

Charney, J.G. (1947), 'The dynamics of long waves in a baroclinic westerly current', *J. Meteorol.*. 4, 135-163.

Chia, F., Griffiths, R.W. and P.F. Linden (1982), 'Laboratory experiments on fronts. Part II: The formation of cyclonic eddies at upwelling fronts', *Geophys. Astrophys. Fluid Dynamics*, 19, 1-18.

Colin de Verdiere, A. (1980), 'Quasi-geostrophic turbulence in a rotating homogeneous fluid', *Geophys. Astrophys. Fluid Dynamics*, 15, 213-251.

Colin de Verdiere, A. (1988), 'Buoyancy driven planetary flows', *J. Mar. Res.*, 46, 215-265.

Condie, S.A. (1988), 'A laboratory model of a convectively driven ocean', *Dyn. Atmos. Oceans*. (in press).

Condie, S.A. and R.W. Griffiths (1988), 'Convection in a rotating cavity: Modelling ocean circulation', *J. Fluid Mech.* (submitted).

Condie, S.A. and G.N. Ivey (1986), 'Laboratory experiments on convection in a rotating rectangular cavity'. *Proceedings of the 9th Australasian Fluid Mechanics Conference*, University of Auckland, December 8th-12th 1986.

Condie, S.A. and G.N. Ivey (1988), 'Convectively driven coastal currents in a rotating basin', *J. Marine Res.*, 46, 473-494.

Cormack, D.E., Leal, L.G. and J. Imberger (1974), 'Natural convection in a shallow cavity with differentially heated end walls. Part 1: Asymptotic theory', *J. Fluid Mech.*, 65, 209-229.

Cormack, D.E., Leal, L.G. and J.H. Seinfield (1974), 'Natural convection in a shallow cavity with differentially heated end walls. Part 2: Numerical solutions', *J. Fluid Mech.*, 65:2, 231-246.

Creswell, G.R., and T.J. Golding (1980) 'Observations of a south-flowing current in the southeastern Indian Ocean' *Deep-Sea Res.*, 27, 449-466.

Dickson, S.C. and R.R. Long (1983), 'Oscillating-grid turbulence including effects of rotation', *J. Fluid Mech.*, 126, 315-333.

Eady, E.T. (1949), 'Long waves and cyclone waves' *Tellus*, 1, 33-52.

Elder, J.W. (1965), 'Laminar free convection in a vertical slot', *J. Fluid Mech.*, 23, 77-98.

Fedorov, K.N. and A.I. Ginsburg (1986), '‹‹ Mushroom-like ›› currents (vortex dipoles) in the ocean and in a laboratory tank', *Annales Geophysicae*, 4, B, 5, 507-516.

Flierl, G.R. (1987), 'Isolated eddy models in geophysics', *Ann. Rev. Fluid Mech.*, 19, 493-530.

Flierl, G.R., Stern, M.E. and J.A. Whitehead (1983), 'The physical significance of modons: Laboratory experiments and general integral constraints', *Dyn. Atmos. Oceans.*, 7, 233-263.

Fu, L.-L., Keffer, P.P. and C. Wunsch (1982), 'Observations of mesoscale variability in western North Atlantic: a comparative study', *J. Mar. Res.*, 40, 809-848.

Gill, A.E. (1966), 'The boundary-layer regime for convection in a rectangular cavity', *J. Fluid Mech.*, 26, 515-536.

Gill, A.E. (1976), 'Adjustment under gravity in a rotating channel', *J. Fluid Mech.*, 77, 603-621.

Gill, A.E. (1982), '*Atmosphere-Ocean Dynamics*', Academic Press.

Gill, A.E., Davey, M.K., Johnson, E.R. and P.F. Linden (1986), 'Rossby adjustment over a step', *J. Mar. Res.*, 44, 713-738.

Godfrey, J.S. and K.R. Ridgeway (1985), 'The large-scale environment of the poleward-flowing Leeuwin Current, Western Australia: Longshore steric height gradients, wind stresses and geostrophic flow', *J.Phys.Oceanogr.*, 15, 481-495.

Griffiths, R.W. (1986), 'Gravity currents in rotating systems', *Ann. Rev. Fluid Mech.*, 18, 59-89.

Griffiths, R.W. and E.J. Hopfinger (1983), 'Gravity currents moving along a lateral boundary in a rotating fluid', *J. Fluid Mech.*, 134, 357-399.

Griffiths, R.W. and E.J. Hopfinger (1984), 'The structure of mesoscale turbulence and horizontal spreading at ocean fronts', *Deep-Sea Res.*, 31:3, 245-269.

Griffiths, R.W., Killworth, P.D. and M.E. Stern (1982), 'Ageostrophic instability of ocean currents', *J. Fluid Mech.*, 117, 343-337.

Griffiths, R.W. and P.F. Linden (1981a), 'The stability of buoyancy-driven coastal currents', *Dynamics Atmos. Oceans*, 5, 281-306.

Griffiths, R.W. and P.F. Linden (1981b), 'The stability of vorticies in a rotating, stratified fluid', *J. Fluid Mech.*, 105, 283-316.

Griffiths, R.W. and P.F. Linden (1982), 'Laboratory experiments on fronts. Part I: Density-driven boundary Currents', *Geophys. Astrophys. Fluid Dynamics*, 19, 159-187.

Griffiths, R.W. and P.F. Linden (1985), 'Intermittent baroclinic instability and fluctuations in geophysical circulations', *Nature*, 316, 801-803.

Griffiths, R.W. and A.F. Pearce (1985a), 'Satellite images of an unstable warm eddy derived from the Leeuwin Current', *Deep-Sea Res.*, 32, 1371-1380.

Griffiths, R.W. and A.F. Pearce (1985b), 'Instability and eddy pairs on the Leeuwin Current south of Australia', *Deep-Sea Res.*, 32, 1511-1534.

Haidvogel, D.B. and T. Keffer (1984), Tracer dispersal by mid-ocean mesoscale eddies. Part 1. Ensemble Statistics', *Dyn. Atmos. Oceans*, 8, 1-40.

Hart, J.H. (1973), 'On the behaviour of large-amplitude baroclinic waves', *J. Atmos. Sc.*, 30, 1017-1034.

Hart, J.H. (1979), 'Finite amplitude baroclinic instability', *Ann. Rev. Fluid Mech.*, 11, 147-172.

Hart, J.H. (1980), 'An experimental study of nonlinear baroclinic instability and mode selection in a large basin', *Dyn. Atmos. Oceans*, 4, 115-135.

Hart, J.H. (1981), 'Wavenumber selection in nonlinear baroclinic instability', *J. Atmos. Sc.*, 38, 400-408.

Hathaway, D.H. and W.W. Fowlis (1986), 'Flow regimes in a shallow rotating cylindrical annulus with temperature gradients imposed on the horizontal boundaries', *J. Fluid Mech.*, 172, 401-418.

Hide, R. (1958), 'An experimental study of thermal convection in a rotating liquid', *Phil. Tran. R. Soc.*, A250, 441-478.

Hide, R. and P.J. Mason (1975), 'Sloping convection in a rotating fluid', *Adv. Phys.*, 24, 57-100.

Hignett, P. (1985), 'Characteristics of Amplitude Vacillation in a Differentially Heated Rotating Fluid Annulus', *Geophys. Astrophys. Fluid Dynamics*, 31, 247-281.

Hignett, P., Ibbetson, A. and P.D. Killworth (1981), 'On rotating thermal convection driven by non-uniform heating from below', *J. Fluid Mech.*, 109, 161-187.

Holland, W.R. and P.B. Rhines (1980), 'An example of eddy-induced ocean circulation', *J. Phys. Oceanogr.*, 10, 1010-1031.

Holloway, G. (1986), 'Eddies, waves, circulation, and mixing: Statistical geofluid mechanics' *Ann. Rev. Fluid Mech.*, 18, 91-147.

Hopfinger, E.J., Browand, F.K. and Y. Gagne (1982), 'Turbulence and waves in a rotating tank', *J. Fluid Mech.* , 125, 505-534.

Hopfinger, E.J., Griffiths, R.W. and M.Mory (1983), 'The structure of turbulence in homogeneous and stratified fluids' *J. de Mec. Theor. Appliq.* , 44, 21-41.

Hsieh, W.W. and A.E. Gill (1984), 'The Rossby adjustment problem in a rotating, stratified channel, with and without topography', *J.Phys.Oceanogr.*, 14, 424-

Hyun, J.M. (1984), 'Source-sink flows of a stratified fluid in a rotating annulus', *J. Fluid Mech..*, 145, 111-125.

Ikeda, M. (1984), 'Coastal flows driven by a local density flux', *J. Geophys. Res.*, 89, 8008-8016.

Ikeda, M., Mysak, L.A., and W.J.Emery (1984), 'Observations and modeling of satellite sensed meanders and eddies off Vancouver Island', *J.Phys.Oceanogr.*, 14, 3-21.

Imberger, J. (1974), 'Natural convection in a shallow cavity with differentially heated end walls. Part 3: Experimental results', *J. Fluid Mech.*, 65, 247-260.

Ivchenko, V.O. and A.V. Klepikov (1985), 'Eddy fluxes of heat, vorticity and momentum in the ocean and atmosphere and their parameterization (a review)', *Oceanol.*, 25, 1-10.

Ivey, G.N. (1984), 'Experiments on transient natural convection in a cavity', *J. Fluid Mech.*, 144, 389-401.

Ivey, G.N. (1987), 'Boundary mixing in a rotating, stratified fluid', *J. Fluid Mech..*, 183, 25-44.

Ivey, G.N. and P.F. Hamblin (1988), 'Convection near the temperature of maximum density for high Rayleigh number, low aspect ratio rectangular cavities', *J. Heat Transfer*, (in press).

Killworth, P.D. (1980), 'Barotropic and baroclinic instability in rotating stratified fluids', *Dynamics Atmos. Oceans* , 4, 143-184.

Killworth, P.D. (1983), 'Long-wave instability of an isolated front', *Geophys. Astrophys. Fluid Dynamics* , 25, 235-258.

Killworth, P.D., Paldor, N. and M.E. Stern (1984), 'Wave propagation and growth on a surface front in a two-layer geostrophic current', *J. Marine Res.*, 42, 761-785.

Killworth, P.D. and M.E. Stern (1982), 'Instabilities on density- driven boundary currents', *Geophys. Astrophys. Fluid Dynamics*, 22, 1-28.

Kubokawa, A. (1985), 'Instability of a geostrophic front and its energetics', *Geophys. Astrophys. Fluid Dynamics*, 33, 223-257.

Li, G-.Q., Kung, R. and R.L. Pfeffer (1986), 'An experimental study of baroclinic flows with and without two-wave bottom topography', *J. Phys. Oceanogr.*, 16, 2585-.

Luyten, J. and H. Stommel (1986), 'Gyres driven by combined wind and buoyancy flux', *J. Phys. Oceanogr.*, 16, 1551-1560.

McCreary, J.P., Shetye, S.R. and P.K. Kundu (1986), 'Thermohaline forcing of eastern boundary currents: With application to the circulation off the west coast of Australia', *J. Mar. Res.*, 44, 71-92.

McEwan, A.D. (1976), 'Angular momentum diffusion and the initiation of cyclones', *Nature*, 260, 126-128.

Mertz, G., El-Sabh, M.I., Proulx, D. and A.R. Condal (1988), 'Instability of a buoyancy-driven coastal jet: The Gaspe Current and its St. Lawrence precursor', *J. Geophys. Res.*, 93, 6885-6893.

Mork, M. (1981), 'Circulation phenomena and frontal dynamics of the Norwegion Coastal Current', *Phil. Trans. R. Soc. Lond.*, 302, 635-647.

Mysak, L.A. and F.Schott (1977), 'Evidence for baroclinic instability off the Norwegian Current', *J.Geophys.Res.*, 82, 2087-2095.

Narimousa, S. and T. Maxworthy (1987), 'Coastal upwelling on a sloping bottom: the formation of plumes, jets and pinched-off cyclones', *J. Fluid Mech.*, 176, 169-190.

Nof, D. (1987), 'Penetrating outflows and the dam-breaking problem', *J. Mar. Res.*, 45, 557-577.

Nunes, R.A. and G.W. Lennon (1987) 'Episodic stratification and gravity currents in a marine environment of modulated turbulence', *J. Geophys. Res.*, 92, 5465-5480.

Ou, H.W. (1983), 'Some Two-Layer Models of the Shelf-Slope Front: Geostrophic Adjustment and its Maintenance' *J. Phys. Oceanogr.*, 13, 1798-1808.

Patterson, J.C. (1984), 'Unsteady natural convection in cavity with internal heating and cooling', *J. Fluid Mech.* , 140, 135-151.

Patterson, J.C. and Imberger, J. (1980), 'Unsteady natural convection in a rectangular cavity', *J. Fluid Mech.* , 100:1, 65-86.

Pedlosky, J. (1979), *'Geophysical Fluid Dynamics'* , Springer-Verlag, New York.

Petrie, B., (1987), 'Undulations of the Nova Scotia Current' *Atmos-Ocean*, 25, 1-9.

Rattray, M. (1985), 'The effect of bathymetry on the deep flow in Drake Passage', *Deep-Sea Res.*, 32, 127-147.

Rhines, P.B. (1969), 'Slow oscillations in an ocean of varying depth. Part 1. Abrupt Topography', *J. Fluid Mech.* , 37, 161-189.

Rhines, P.B. (1970), 'Edge-, bottom- and Rossby waves in a rotating stratified fluid', *Geophys. Fluid Dyn.*, 1, 273-302.

Rhines, P.B. (1979), 'Geostrophic turbulence', *Ann. Rev. Fluid Mech.* , 11, 401-441.

Rhines, P.B. (1986), 'Vorticity dynamics of the ocean general circulation', *Ann. Rev. Fluid Mech.* , 18, 433- 497.

Rhines, P.B. and W.R. Young (1983), 'How rapidly is a passive scalar mixed within closed streamlines', *J. Fluid Mech.*, 133, 133-145.

Robinson, A.R.(ed.) (1983), *'Eddies in Marine Science'*, Springer-Verlag.

Rossby, H.T. (1969), 'A study of Benard convection with and without rotation', *J. Fluid Mech.* , 36, 309-335.

Royer, T.C. (1981), 'Baroclinic transport in the Gulf of Alaska Part II. A fresh water driven coastal current', *J.Mar.Res.*, 39, 251-266.

Salmon, R. (1982), 'Geostrophic turbulence', *Proc. Int. School Phys.*, 7th-19th July, Varenna.

Simpkins, P.G. and T.D. Dudderar (1981), 'Convection in rectangular cavities with differentially heated end walls', *J. Fluid Mech.* , 110, 433-456.

Simpson, J.E. (1982) ' Gravity currents in the laboratory, atmosphere, and ocean', *Ann. Rev. Fluid Mech.* , 14, 213-234.

Simpson, J.E. and R.E. Britter (1979), 'The dynamics of the head of a gravity current advancing over a horizontal surface', *J. Fluid Mech.* , 94, 477-495.

Smith, P.C. (1975), 'A streamtube model for bottom boundary currents in the ocean', *Deep-Sea Res.*, 22, 853-873.

Speer, K.G. and J.A. Whitehead (1988), 'A gyre in a non-uniformly heated rotating fluid', *Deep-Sea Res.* in press.

Stern, M.E. (1980), 'Geostrophic fronts, bores, breaking and blocking waves', *J. Fluid Mech.* , 99, 687-703.

Stern, M.E., Whitehead, J.A. and B. Hua (1982), 'The intrusion of a density current along the coast of a rotating fluid', *J. Fluid Mech.* , 123, 237-265.

Stommel, H., A.B. Arons and A.J. Faller (1958), 'Some examples of stationary flow patterns in bounded basins', *Tellus*, 10, 179-187.

Sugimoto, T. and J.A. Whitehead (1983), 'Laboratory models of bay-type continental shelves in the winter', *J. Phys. Oceanography* , 13, 1819-1828.

Talley, L.D. (1988), 'Potential vorticity distribution in the North Pacific', *J. Phys. Oceanogr.*, 18, 89-106.

Tennekes, H. (1985), 'A comparative pathology of atmospheric turbulence in two and three dimensions', *Proc. Int. School Phys.*, Varenna.

Thompson, R.O.R.Y. (1984), 'Observations of the Leeuwin Current off Western Australia', *J.Phys.Oceanogr.*, 14, 623-628.

Tritton, D.J. (1985), 'Experiments on turbulence in geophysical fluid dynamics. Part 1: Turbulence in rotating fluids', *Proc. Int. School Phys.*, Varenna.

Tucholke, B.E., Wright, W.R. and C.D. Hollister (1973), 'Abyssal circulation over the Greater Antilles Ridge', *Deep-Sea Res.*, 20, 973-995.

Turner, J.S. (1973), '*Buoyancy Effects in Fluids*', Cambridge University Press, Great Britain.

Wadhams, P., Gill, A.E. and P.F. Linden (1979), 'Transects by submarine of the East Greenland Polar Front', *Deep-Sea Res.* , 26A, 1311-1327.

Warren, B.A. (1981), 'Deep circulation of the world ocean', In: Warren, B.A. and C. Wunsch (Eds.), *Evolution of Physical Oceanography* , MIT Press, USA.

Weaver, A.J. and J.H. Middleton (1988), 'On the dynamics of the Leeuwin Current', *J. Phys. Oceanogr.*, (submitted).

Whitehead, J.A. (1985), 'The deflection of a baroclinic jet by a wall in a rotating fluid', *J. Fluid Mech.*, 157, 79-93.

Whitehead, J.A. and D.C. Chapman (1986), 'Laboratory observations of a gravity current on a sloping bottom: the generation of shelf waves', *J. Fluid Mech.*, 172, 373-399.

Whitehead, J.A. and A.R. Miller (1979), 'Laboratory simulation of the gyre in the Alboran Sea', *J. Geophys. Res.*, 84, 3733-3742.

Worster, M.G. and A.M. Leitch (1985), 'Laminar free convection in confined regions', *J. Fluid Mech.*, 156, 301-319.

Yewell, P., D. Poulikakos and A. Bejan (1982), 'Transient natural convection experiments in shallow enclosures', *Trans. ASME: J. Heat Transfer*, 104, 533-538.